LBNL-38901
UC-401

ERNEST ORLANDO LAWRENCE
BERKELEY NATIONAL LABORATORY

High-Resolution Spectroscopy Using Synchrotron Radiation for Surface Structure Determination and the Study of Correlated Electron Systems

E.J. Moler, Jr.
Accelerator and Fusion
Research Division

May 1996
Ph.D. Thesis

DISCLAIMER

This document was prepared as an account of work sponsored by the United States Government. While this document is believed to contain correct information, neither the United States Government nor any agency thereof, nor The Regents of the University of California, nor any of their employees, makes any warranty, express or implied, or assumes any legal responsibility for the accuracy, completeness, or usefulness of any information, apparatus, product, or process disclosed, or represents that its use would not infringe privately owned rights. Reference herein to any specific commercial product, process, or service by its trade name, trademark, manufacturer, or otherwise, does not necessarily constitute or imply its endorsement, recommendation, or favoring by the United States Government or any agency thereof, or The Regents of the University of California. The views and opinions of authors expressed herein do not necessarily state or reflect those of the United States Government or any agency thereof, or The Regents of the University of California.

This report has been reproduced directly from the best available copy.

Ernest Orlando Lawrence Berkeley National Laboratory
is an equal opportunity employer.

LBNL-38901
LSBL-330
UC-401

HIGH-RESOLUTION SPECTROSCOPY USING SYNCHROTRON RADIATION FOR SURFACE STRUCTURE DETERMINATION AND THE STUDY OF CORRELATED ELECTRON SYSTEMS*

Edward John Moler, Jr.
Ph.D. Thesis

DEPARTMENT OF CHEMISTRY
University of California, Berkeley

and

Accelerator and Fusion Research Division
Ernest Orlando Lawrence Berkeley National Laboratory
University of California
Berkeley, CA 94720

MAY 1996

---

*This work was supported by the Director, Office of Energy Research, Office of Basic Energy Sciences, Chemical Sciences Division, of the U.S. Department of Energy, under Contract No. DE-AC03-76SF00098.

Light Source Note:
Author(s) Initials EJM. 5-17-96
Date
Group Leader's initials 5-17-96
Date

High Resolution Spectroscopy Using Synchrotron Radiation for Surface Structure Determination
and
the Study of Correlated Electron Systems

by

Edward John Moler, Jr.

B. S. (Texas A&M University) 1989

A dissertation submitted in partial satisfaction of the
requirements for the degree of
Doctor of Philosophy
in
Chemistry
in the
GRADUATE DIVISION
of the
UNIVERSITY of CALIFORNIA, BERKELEY

Committee in Charge:

Professor David A. Shirley, Chair
Professor Gabor A. Somorjai, Co-Chair
Professor A. Paul Alivisatos
Professor Zahid Hussain
Professor David T. Attwood

1996

High Resolution Spectroscopy Using Synchrotron Radiation for Surface Structure Determination and the Study of Correlated Electron Systems

by

Edward John Moler, Jr.

ABSTRACT

High Resolution Spectroscopy Using Synchrotron Radiation
for Surface Structure Determination
and
the Study of Correlated Electron Systems

by

Edward John Moler, Jr.
Doctor of Philosophy
in
Chemistry
University of California, Berkeley
Professor David A. Shirley, chair

The surface structure of three molecular adsorbate systems on transition metal surfaces, $(\sqrt{3} \times \sqrt{3})R30°$ and $(1.5 \times 1.5)R18°$ CO adsorbed on Cu(111), and c(2x2) N_2/Ni(100), have been determined using Angle-Resolved Photoemission Extended Fine Structure (ARPEFS). The adsorption site and bond lengths are reported for the adsorbate-metal bond and the first two substrate layers. The ARPEFS diffraction pattern of the shake-up peak for c(2x2) N_2/Ni(100) is also discussed.

A unique method of experimentally determining the angular momentum and intrinsic/extrinsic origin of core-level satellites is presented. We show for the first time that satellite peaks not associated with chemically differentiated atomic species display an ARPEFS intensity oscillation. Specifically, we present data for the C 1s from $(\sqrt{3}x\sqrt{3})R30$

CO/Cu(111) and p2mg(2x1)CO/Ni(110), N 1s from c(2x2) N_2/Ni(100), and Ni 3p from clean nickel(111). The satellite peaks in all cases exhibit ARPEFS curves which indicate an angular momentum identical to the main peak and are of an intrinsic nature.

A Fourier Transform Soft X-ray spectrometer (FT-SX) has been designed and is under construction for the Advanced Light Source (ALS) at Lawrence Berkeley National Laboratory. The spectrometer is designed for ultra-high resolution (theoretical resolving power $E/\Delta E{\sim}10^6$) in the photon energy region of 60-120 eV. This instrument is expected to provide experimental results which sensitively test models of correlated electron processes in atomic and molecular physics. The design criteria and consequent technical challenges posed by the short wavelengths of x-rays and desired resolving power are discussed. The fundamental and practical aspects of soft x-ray interferometry are also explored.

Table of Contents

Dedication and Acknowledgments

I dedicate this work to my loving wife, whose support and encouragement was invaluable and who brings meaning to all of my activities. I also dedicate this thesis to my parents for their faith in my abilities and their support of my indulgence to follow my dreams.

Several people have contributed greatly to my experience and work throughout graduate school. First and foremost is Dr. Zahid Hussain, without whom I could never have continued in this field of study. Second is Dr. Tony Huff and Scot Kellar: their contributions have enabled the execution and completion of this work. I also thank Dr. David Shirley, my research advisor, for his guidance and confidence. Malcolm Howells has played a very great role in the design of the FT-SX spectrometer and I have learned a great deal from him in our many discussions on optics and the theory of the instrument.

Finally, I thank the staff and management of the Advanced Light Source at Lawrence Berkeley National Laboratory, the Stanford Synchrotron Radiation Facility at Stanford University, and the National Synchrotron Light Source at Brookhaven National Laboratory, whose support is greatly appreciated.

This work was supported by DOE grand DE-AC03-76SF00098. The support of the Department of Energy Office of Basic Energy Sciences is gratefully acknowledged.

Introduction

Since the establishment of quantum mechanics and the photoelectric effect in the early 1900's, a good understanding has been developed of the interaction between a single photon and an ensemble of independent electrons. Some of the earliest, and most important, experimental techniques developed upon this basic understanding include x-ray diffraction for the study of inorganic and biological crystals and electron spectroscopy and x-ray fluorescence for elemental analysis.

With these reductionist successes firmly in hand, the latter half of the 20th century has seen science begin to address problems of greater complexity. The correlated motions of photons with independent electrons were explored and culminated in the development of lasers in the 1960's. The correlated motions of high-energy electrons in dense beams, and the consequent emission of x-ray photons, were explored in the development of electron-synchrotron storage rings. These tools enable even further investigations into complex problems which cut across all scientific disciplines. The future will probably bring even brighter and shorter x-ray pulses from free-electron lasers, which are based upon both correlated electron and correlated photon motions.

The recent development of high brightness synchrotron x-ray sources, the so-called "third generation synchrotrons", has opened up new avenues of investigation which were previously inaccessible or extremely difficult to achieve. The advent of more intense probes (beams) leads to two general investigative paths: studies of more dilute or short-lived systems, and studies of more subtle and complex phenomena.

In this thesis, I have utilized this new tool to pursue both paths. The study of molecular adsorbates on metal surfaces is a dilute system important to both fundamental and applied chemical physics. Using the photoelectric effect treated with an independent, quantum-mechanical electron approximation, the surface spatial structure can be elucidated. More complex phenomena arise in situations where the independent electron approximation break down. In photoemission, multi-electron excitations are often the dominant process, giving rise to satellite peaks which contain information on the ground- and excited-states of the molecule or surface. Double excitation of the helium atom is the most fundamental 3-body problem and x-ray absorption provides a very sensitive test of the electron-electron correlation model. Correlated electron motions are at the heart of any chemical reaction and constitute one of the most important fundamental questions of chemistry for the coming decades.

Spatial Structure Determination of (√3 x √3)R30° and (1.5 x 1.5)R18° CO on Cu(111) using Angle-Resolved Photoemission Extended Fine Structure

Abstract

We report a study of the spatial structure of (√3 x √3)R30° and (1.5 x 1.5)R18° CO adsorbed on Cu(111), using the Angle-Resolved Photoemission Extended Fine Structure (ARPEFS) technique. The ARPEFS data were taken along the surface normal-emission direction with a sample temperature of 80 K. The CO molecule adsorbs on an atop site for both adsorption phases. Full multiple-scattering spherical-wave (MSSW) calculations were used to extract the C-Cu bond length and the first Cu-Cu layer spacing for each adsorption phase. The C-Cu bond length is 1.91 (1) Å in the (√3 x √3)R30° phase and 1.91(2) Å in the (1.5 x 1.5)R18° phase. The first layer Cu-Cu spacing is 2.07(3) Å in the (√3 x √3)R30° phase. The first layer Cu-Cu spacing in the (1.5 x 1.5)R18° phase is 2.01(4) Å, a contraction of 3 % from the clean metal value of 2.07 Å. We calculate the bending mode force constant in the (1.5 x 1.5)R18° phase to be k_δ=2.2 (1) x 10^{-12} dyne·cm/rad from the above bond lengths combined with previously published infra-red absorption frequencies.

Introduction

The adsorption of carbon monoxide on transition-metal surfaces has been extensively studied, both experimentally[1-12] and theoretically[13-19], with the goal of gaining a basic understanding of the surface chemical bond. Experimentally determined spatial structures of CO adsorbates provide important tests of theoretical models for these systems. We have determined the carbon-copper bond length and the first copper-copper layer spacing for two different, well-ordered coverage phases of CO on Cu(111) using Angle-Resolved Photoemission Extended Fine Structure (ARPEFS)[20].

The adsorption of CO on Cu(111) has been previously investigated with Fourier-transform Reflection Adsorption Infra-Red Spectroscopy (FT-RAIRS), Electron Energy Loss Spectroscopy (EELS) and Low Energy Electron Diffraction (LEED) by Raval, et. al.[8]. They found that CO adsorbs on an atop site with the carbon end down for the first two coverage phases, which exhibit a ($\sqrt{3} \times \sqrt{3}$)R30° LEED pattern at ~0.33 monolayer coverage and a (1.5 x 1.5)R18° pattern for a coverage of ~0.44 monolayer. Based on their observations, they proposed an overlayer structure for the (1.5 x 1.5)R18° phase in which there are six CO molecules which each have two adjacent CO adsorbates and one CO which has no adjacently adsorbed molecules. We reproduce this proposed structure in Fig. 1. Additional evidence for the atop adsorption of CO/Cu(111) in the two lower-coverage phases was reported by Hirschmugl, et. al., using far-IR reflection-absorption spectroscopy with synchrotron radiation[5]. They also reported finding a low-frequency vibrational mode which is assigned to a frustrated rotation or bending mode of the Cu-C-O bond in the (1.5 x 1.5)R18° phase. The Gibbs free activation energy of desorption was found to exhibit a dramatic rise in the transition from the higher coverage (1.5 x 1.5)R18° phase to the lower coverage ($\sqrt{3} \times \sqrt{3}$)R30° phase by thermal desorption spectroscopy (TDS)[11]. The isosteric heat of adsorption also shows an abrupt change, from ~ 38 kJ/mole to 50 kJ/mole, at the transition from the (1.5 x 1.5)R18° phase to the ($\sqrt{3}$ x $\sqrt{3}$)R30° phase as determined by surface potential measurements[6].

The bonding of CO to copper surfaces has been treated theoretically by several workers[14-19]. These investigations infer that the bonding between the CO molecule and the surface are primarily dominated by the donation of the Cu 3d and valence electrons into the antibonding $2\pi^*$ molecular orbital (MO), which resides primarily on the carbon atom. Hence, the molecule usually adsorbs with the carbon end down. The transfer of electronic charge to the molecule leads to a positive charge on the metal which stabilizes the repulsive interaction between the occupied 5σ MO and the metal valence electrons.

The ARPEFS structure determination technique is based on the oscillatory variation in the angle-resolved photoemission intensity from the core levels of near-surface atoms with the electron kinetic energy. It has been successfully used in the past few years to study the local structure of adsorbed atoms and molecules and to determine the substrate layer relaxation[7,20-24]. The surface structure can be determined quantitatively by fitting the experimental data with multiple-scattering spherical-wave (MSSW) calculations[7,20,24,25].

Experimental

The experiments were carried out in an ultrahigh-vacuum chamber with a base pressure $<2 \times 10^{-10}$ torr. The chamber was equipped with an ion-gun, a four-grid LEED system, a liquid helium cooled sample manipulator, and a 50 mm angle-resolving, hemispherical electrostatic electron energy analyzer for X-ray photoemission experiments. The hemispherical analyzer had an acceptance half-angle of approximately 2 degrees.

The copper (111) substrate was cleaned and prepared using the standard UHV surface science techniques of argon-ion sputtering and annealing by e-beam heating. The surface order and cleanliness were checked with LEED and synchrotron-radiation excited XPS. There was no detectable carbon or oxygen contamination on the surface and the LEED showed a sharp 1x1 pattern. The sample was aligned by laser autocollimation and LEED. The sample temperature was measured by a chromel-alumel thermocouple, spot-welded near the sample. A liquid nitrogen reference junction was used with the thermocouple.

The CO overlayers were prepared by first cooling the copper substrate to ~ 80 K then backfilling the chamber with 1x10^{-8} Torr of CO for ~30 seconds through a variable leak-valve . The sample was then gently warmed to 130 K at a rate of 0.5 K/sec and subsequently cooled to 80 K, resulting in a sharp (1.5 x 1.5) R18° LEED pattern. A sharp ($\sqrt{3}$ x $\sqrt{3}$) R30° pattern resulted from warming the sample to 150 K at the same rate. During the ARPEFS experiments, the sample was maintained at 80 K. We were careful not to damage the overlayers used for the ARPEFS experiment, by checking the LEED pattern only briefly near and the edge of the sample.

The experiments were performed using the spherical-grating x-ray monochromator on beam-line 9.3.2 at the Advanced Light Source, Lawrence Berkeley National Laboratory. A 55-meter radius, 600 line/mm grating was used to provide photons in the energy range 385-700 eV. The x-ray angle of incidence on the sample was 20° and the photoelectron emission direction was normal to the surface for all experiments. The x-ray monochromator was set to a 0.1% bandpass. The hemispherical electron energy analyzer was set to a resolution of 0.3 eV, yielding an overall resolution of 0.5-0.7 eV.

A series of carbon 1s photoemission spectra were taken for each overlayer over a kinetic energy range of 100-400 eV in electron wave-vector increments of 0.1 $Å^{-1}$. Figure 2 shows a typical XPS spectrum for this work. The intensities of the main and satellite peaks were determined by least-squares fitting each peak to a Voigt function, a step-like Voigt-function integral to account for the inelastically scattered electrons associated with the peak, and an experimental background which arises mainly from the inelastically scattered electrons from the substrate. Also shown in figure 2 is the deconvoluted components of the spectrum from the best-fit. Each peak intensity is normalized to an emperical inelastic background.

The total photoemission intensity I(k), as a function of electron wave-number in $Å^{-1}$, is composed of a slowly varying, atomic-like portion $I_0(k)$ and a rapidly oscillating portion due to the interference of the electron wave resulting from scattering from nearby atoms. The ARPEFS curve $\chi(k)$ is obtained by removing the slowly varying portion

$$\chi(k)=[I(k)-I_0(k)]/I_0(k).$$

$I_0(k)$ is determined by least-square fitting of a low-order polynomial through the experimental curve I(k). Only the main peak intensity was used for the structure analysis. We note here that the satellite peaks show the same ARPEFS oscillations as the main peak, after adjustment to each peak's k-value, which is shifted relative to the main peak by the binding energy difference. Further analysis of the satellite-peak ARPEFS for this and other systems will be reported separately.

Surface Structure Determination

The ARPEFS curves for both the (√3 x √3) R30° and (1.5 x 1.5) R18° overlayers are shown in Fig. 3. Their similarity suggests that the adsorption site is the same for both structures with only small differences in the interlayer spacings in agreement with previous FT-IR and EELS results which indicate only one kind of adsorption site for these structures[8]. The Fourier transforms of the experimental data are also shown if Fig. 3. The dominant peak at ~4 Å arises from back scattering of the photoelectron from the nearest neighboring copper atom in the first copper layer. The second peak, at ~8 Å path-length difference, is due to scattering from the nearest second-layer copper atoms.

We have performed full Multiple Scattering Spherical Wave (MSSW) calculations to quantitatively extract the inter-layer spacing between the overlayer and substrate and between the near-surface substrate layers. The calculation program is based on the formalism of Rehr and Albers[25]. The program, developed entirely within our group, is highly optimized for obtaining a best fit to experimental data. It uses second-order matrices (6x6) and up to 8th order scattering, which produce a convergent calculation at these energies and inter-atomic distances. The best fit was defined by the conventional R-factor analysis[21]. Previous studies of these overlayers with FT-IR and EELS determined that the CO molecules adsorbed on atop sites with the carbon end down[8]. We assumed in the calculations that the molecules in the (1.5 x 1.5) R18° structure adsorb on nearest atop sites in accordance with the structure proposed by Raval, et. al.[8] The layer spacing between carbon-oxygen, carbon-copper, and between the first three copper layers were allowed to vary. Two non-structural parameters were also allowed to vary: the surface Debye temperature and the inner potential.

The results of the MSSW calculations with lowest R-factor for each structure are shown in Fig. 4. The R-factor is 0.12 for both structures. The carbon-copper layer spacing for both structures were found to be the same, 1.91 Å. The first copper-copper layer spacing was found to be 2.07 Å and 2.01 Å for the ($\sqrt{3}$ x $\sqrt{3}$) R30° and (1.5 x 1.5) R18° overlayer structures, respectively. These derived parameters proved to be insensitive to the C-O bond-length and tilt. This is expected, because the oxygen atom is in a forward-scattering geometry for the normal-emission experiment. We also found the results to be insensitive to neighboring C-O molecules because the amplitude for 90° scattering is very low. The surface Debye temperature was determined to be 200 K. The R-factors are relatively insensitive to the inner potential and to the spacing between the second, third, and fourth copper layers.

Error Analysis

The statistical uncertainty of each structural parameter is estimated from the curvature of the R-factor plotted versus the parameter value, as previously described method[24]. The uncertainty determined by this method is reported as one standard deviation, i.e. with a 0.67 confidence level[26]. The uncertainty in the last digit appears in parenthesis after the number. The R-factor plots for the C-Cu layer spacing and the first Cu-Cu layer spacing are shown for each of the two overlayer structures in Fig. 5. Statistical uncertainties in the C-Cu bond length are 0.01 Å and 0.02 Å for the ($\sqrt{3}$ x $\sqrt{3}$) R30° and (1.5 x 1.5) R18° overlayer structures, respectively. The first Cu-Cu layer spacings have uncertainty estimates of 0.03 Å and 0.04 Å for the (√3 x √3) R30° and (1.5 x 1.5) R18° overlayer structures, respectively. Possible systematic errors for this technique have been previously discussed in detail[20].

Further Considerations Concerning the Structure of the (1.5 x 1.5) R18° Overlayer

The relative positions of adsorbed CO molecules in the (1.5 x 1.5) R18° overlayer may lead to inequivalent adsorption sites. The question arises as to whether these inequivalent sites may have different layer spacings. As stated above, the normal-emission geometry of this experiment renders the results insensitive to the position of the neighboring CO molecules. We may, however, determine the sensitivity to a variation in layer spacing using R-factor analysis. We have assumed the adsorption structure for the (1.5 x 1.5) R18° overlayer as proposed by Raval, et. al.[8], as reproduced in Fig. 1. The A-type adsorption site is one CO molecule with no adjacent adsorbates. The B-type molecules each have two neighboring adsorbates. Note that there are six B-type molecules to one A-type. The R-factor vs. A-B layer spacing is shown in Fig. 6, in which the B-Cu layer spacing was fixed at 1.91 Å. The R-factor analysis leads to no detectable difference between A-Cu and B-Cu layer spacings, with an uncertainty of ±0.03 Å.

Results and Discussion

The results of this work are summarized in Table I. The chi curve based on the atop adsorption site of the CO molecule with the carbon end down shows excellent agreement (R=0.12) between the MSSW calculations and the experimental data, confirming the previous findings for the two lowest-coverage phases[5,6,8,11,12]. The C-Cu bond length is the same for both coverages, 1.91 Å with uncertainties of ±0.01 Å and ±0.02 Å for the (√3 x √3) R30° and (1.5 x 1.5) R18° overlayer structures, respectively. The C-Cu bond length is similar to the value of 1.8(1) Å for c(2x2) CO/Cu(100) determined by LEED[1] with the possible expansion being consistent with the observation that CO is least strongly bound on the (111) face[27]. The first copper-copper layer spacing does not show any change from the clean copper surface spacing of 2.07(2) Å[28] for the lower coverage (√3 x √3) R30° phase, within experimental uncertainty. There is a distinct contraction of the surface layer for the higher coverage (1.5 x 1.5) R18° phase to 2.01(4) Å. These experiments were not sensitive to the C-O tilt or bond length.

The fact that the Cu-C bond length remains constant for both adsorption coverages while the 1st Cu-Cu layer spacing changes has interesting implications regarding the energetics and dynamics of the two overlayers. The difference in Gibbs free energy between the adsorbed state and the same state activated for desorption has been shown to have a dramatic increase with decreasing coverage between the (1.5 x 1.5) R18° and the (√3 x √3) R30° phases[11], while the change is less steeply sloped at lower and higher coverages. The coverage-dependent isosteric heat of adsorption also has a significant inflection in the region between the (1.5 x 1.5) R18° and the (√3 x √3) R30° phases, with a nearly constant values of 50 kJ/mole at lower coverages and 38 kJ/mole at higher coverages[6]. The authors of Reference 6 noted that this inflection could indicate the onset of a different adsorption site, but pointed out that this hypothesis did not explain why the heat of adsorption then remained constant throughout the high coverage region. Subsequent work showed that only atop species exist for these phases[8]. It has also been suggested that competition for back-donated metal d-electrons may weaken the Cu-CO bond with increasing coverage[6]. Our results indicate that the Cu-CO bond does not weaken with greater coverage but that the changes in energy of adsorption are related to an adsorbate-induced contraction of the first substrate layer. There is little if any contraction of the first Cu-Cu layer up to a coverage of 0.33 monolayer. The onset of the inflections in the thermodynamic properties occur at approximately this coverage. The end of the inflections at the 0.44 monolayer coverage would suggest that there is no further contraction of the first Cu-Cu layer beyond that determined for the (1.5 x 1.5) R18° structure.

Theoretical studies of CO on transition metal surfaces published to date have to our knowledge not specifically investigated the relaxation of the substrate with increasing adsorbate coverage. One notable study has touched upon relevant effects for CO adsorbed on copper (100)[16]. Bauschlicher found that two layers are required to describe the binding energy of low coverage CO/Cu(100) convergently and three layers are required at higher coverages[16]. This requirement is ascribed to the repulsion of metal valence electrons by the CO molecules into the second and third copper layers. Bauschlicher also reported that changing the layer spacing of the first two copper layers does not significantly affect the binding energy or geometry of the CO molecule. Our finding of constant Cu-CO bond length, despite the first copper layer contraction, suggests that the binding energy is indeed unchanged. Further theoretical investigation is required to gain an understanding of why a change in surface coverage of 0.33 monolayer to 0.44 monolayer results in a contraction of the first copper layer.

Infrared and electron energy loss spectroscopy (EELS) studies of the CO/Cu(111) have been previously employed to elicit the dynamics of the adsorbate-substrate interactions[5,6,8,29]. Hirschmugl, et. al.[5] used synchrotron radiation to study the IR absorption region of the Cu-C stretch at 347 cm^{-1}. Their data show no observable shift in the Cu-C stretch mode with increasing coverage, providing further evidence that the Cu-C bond energy is not coverage-dependent. However, Hollins and Pritchard found a softening of the C-O bond mode with increasing coverage, using an isotopic-substitution IR technique[6]. In light of our results, it is now clear that, beginning with a coverage of 0.33 monolayer, the first layer Cu-Cu spacing contracts while the C-O bond weakens with increasing coverage, thereby leaving the Cu-C bond largely unchanged.

Hirschmugl, et. al. observed an IR adsorption band at ~285 cm^{-1} which was assigned to a bending (frustrated rotation) mode of the Cu-C-O complex in the (1.5 x 1.5) R18° structure. Calculation of the force constant of the bending-mode vibration, υ_2, of a linear molecule requires knowledge of the bond lengths between the atoms.Using our results and the frequency measurements of Hurschmugl, we can determine the bending mode force constant from[5,30]

$$(2\pi \upsilon_2)^2 = \frac{k_\delta}{l_1^2 l_2^2}\left[\frac{l_1^2}{m_O} + \frac{l_2^2}{m_{Cu}} + \frac{(l_1 + l_2)^2}{m_C}\right] \qquad (1)$$

where k_δ is the force constant, l_1 is the Cu-C bond length, l_2 is the C-O bond length, and m is the mass of each atomic species. We assume the C-O bond length to be that of the gas phase, 1.13(2) Å. This assumption seems justified, as numerous structural studies of CO adsorbed on transition metal surfaces do not find more than 0.02 Å change in bond length, e.g. see refs[31,32]. Additionally, the CO interaction with Cu(111) is among the weakest studied and we feel that the above uncertainty is a rather conservative estimate. The values of the IR absorption frequencies for three isotopes as measured by Hirschmugl, et. al. are 285(8) cm^{-1}, 273(8) cm^{-1}, and 285(6) cm^{-1} for $^{12}C^{16}O$, $^{13}C^{18}O$, and $^{12}C^{18}O$, respectively. Using equation (1) above we find the force constant to be k_δ=2.2(1) x 10^{-12} dyne·cm/rad. The uncertainty was estimated by propagation of the experimental uncertainties[33].

Conclusion

We have determined the spatial structure of CO/Cu(111) for two coverages, characterized by (1.5 x 1.5) R18° and (√3 x √3) R30° LEED patterns, using ARPEFS. The CO molecule adsorbs on an atop site at both coverages with a C-Cu bond length of 1.91 Å, with an uncertainty of ±0.01 Å and ±0.02 Å for the two respective structures. The first Cu-Cu layer spacings were found to be 2.07 (3) Å and 2.01(4) Å for the (1.5 x 1.5) R18° and (√3 x √3) R30° structures, respectively. The bending mode force constants for the Cu-C-O complex in the (1.5 x 1.5) R18° structure is calculated from the bond-lengths and published IR absorption frequencies to be k_δ=2.2(1) x 10^{-12} dyne·cm/rad.

Bibliography

[1] S. Andersson and J. B. Pendry, "The structure of c(2x2) CO adsorbed on copper and nickel (001) surfaces," Journal of Physics C **13**, 3547-3561 (1980).

[2] H. Antonsson, A. Nilsson, and N. Martensson, "Vibrational Motion and Geometrical Structure in Adsorbed CO Studied by Core Level Photoelectron Spectroscopy," Journal of Electron Spectroscopy and Related Phenomena **54/55**, 601-613 (1990).

[3] A. M. Baro and H. Ibach, "New Study of CO adsorption at low temperature (90 K) on Pt(111) by EELS," Journal of Chemical Physics **71** (12), 4812-4817 (1979).

[4] J. E. Demuth and D. E. Eastman, "Photoemission Observation of Two Molecular Phases of CO Absorbed on Cu(100)," Solid State Communications **18**, 1497-1500 (1976).

[5] C. J. Hirschmugl, G. P. Williams, F. M. Hoffmann, and Y. J. Chabal, "Adsorbate-Substrate Resonant Interactions Observed for CO on Cu(100) and (111) in the Far-IR using Synchrotron Radiation," Journal of Electron Spectroscopy and Related Phenomena **54/55**, 109-114 (1990).

[6] P. Hollins and J. Pritchard, "Interactions of CO Molecules Adsorbed on Cu(111)," Surface Science **89**, 486-495 (1979).

[7] Z. Huang, "Structural Studies of Molecular Metallic Overlayers Using Angle-Resolved Photoemission Extended Fine Structure," Ph. D. Thesis, LBNL report LBL-33040, University of California, Berkeley, 1992.

[8] R. Raval, S. F. Parker, M. E. Pemble, P. Hollins, J. Pritchard, and M. A. Chesters, "FT-RAIRS, EELS and LEED Studies of the Adsorption of Carbon Monoxide on Cu(111)," Surface Science **203**, 353-377 (1988).

[9] A. Sandell, P. Bennich, A. Nilsson, B. Hernnas, O. Bjorneholm, and N. Martensson, "Chemisorption of CO on Cu(100), Ag(110), and Au(110)," Surface Science **310**, 16-26 (1994).

[10] A. G. Yodh and H. W. Tom, "Picosecond linear vibrational spectroscopy of CO adsorbed on Cu(111) by phase-sensitive polarization modulation," Physical Review B **45** (24), 302-307 (1992).

[11] W. Kirstein, B. Kruger, and F. Theime, "CO Adsorption Studies on Pure and Ni-covered Cu(111) Surfaces," Surface Science **176**, 505-529 (1986).

[12] B. J. Hinch and L. H. Dubois, "Time-Resolved EELS Studies of Molecular Surface Residence Times: the CO/Cu(111) Desorption System," Journal of Electron Spectroscopy and Related Phenomena **54/55**, 1990 (1990).

[13] C. Rong and C. Satoko, "Adsorption of N2, CO, and No on Fe(111) Surface: Model Calculation by DV-X-Alpha Method," Surface Science **223**, 101-118 (1989).

[14] J. Paul and A. Rosen, "Electronic Structure of CO adsorbed on a Cu(111) surface analyzed with molecular cluster models.," Physical Review B **26** (8), 4073-4077 (1982).

[15] A. C. Pavao, M. Braga, C. A. Taft, B. L. Hammond, and W. A. Lester, "Theoretical Study of the CO interaction with 3d-metal surfaces," Physical Review B **43** (9), 6962-6966 (1991).

[16] C. W. Bauschlicher, "A theoretical study of CO/Cu(100)," Journal of Chemical Physics **101** (4), 3250-3254 (1994).

[17] E. Miyoshi, Y. Sakai, and S. Katsuki, "A molecular orbital study for CO coadsorbed with K on Cu(001) and Ag(001)," Surface Science **242**, 1991531-537 (1991).

[18] M. A. Nygren and P. E. M. Siegbahn, "Theoretical Study of Chemisorption of CO on Copper Clusters," Journal of Chemical Physics **96**, 7579-7584 (1992).

[19] R. A. Van Santen, "Coordination of Carbon Monoxide to Transition-metal Surfaces," Journal of the Chemical Society, Faraday Transactions **81**, 1915-1934 (1987).

[20] J. J. Barton, C. C. Bahr, C. C. Robey, Z. Hussain, E. Umbach, and D. A. Shirley, "Adsorbate-geometry determination by measurement and analysis of angle-

resolved-photoemission extended-fine-structure data: application to c(2*2)S/Ni(001)," Physical Review B **34** (6), 3807-3819 (1986).

[21] J. J. Barton, S. W. Robey, C. C. Bahr, and D. A. Shirley, "Surface Structure Determination with ARPEFS," in *The Structure of Surfaces(Springer Series in Surface Sciences)*, edited by M. A. Van Hove and S. Y. Tong (Springer Verlag, New York, 1985), Vol. 2, pp. 191-198.

[22] S. W. Robey, J. J. Barton, C. C. Bahr, G. Liu, and D. A. Shirley, "Angle-resolved-photoemission extended-fine-structure spectroscopy investigation of c(2x2) S/Ni(011)," Physical Review B **35** (3), 1108 (1987).

[23] K. T. Leung, L. J. Terminello, Z. Hussain, X. S. Zhang, T. Hayashi, and D. A. Shirley, "Surface-bonding geometry of (2x1)S/Ge(001) fby the normal-emission angle-resolved photoemission extended-fine-structure technique," Physical Review B **38** (12), 8241 (1988).

[24] L. Q. Wang, A. E. Schach von Wittenau, Z. G. Ji, Z. Q. Huang, and D. A. Shirley, "c(2x2) Cl/Cu(001) adsorbate geometry and substrate-surface relaxation using low-temperature angle-resolved photoemission extended fine structure," Physical Review B **44**, 8241 (1991).

[25] J. Rehr and Albers, "Scattering-matrix formulation of curved-wave multiple-scattering theory: Application to x-ray-absorption fine structure," Physical Review B **41** (12), 8139 (1990).

[26] W. H. Press, S. A. Teukolsky, W. T. Vertterling, and B. P. Flannery, *Numerical Recipes in C*, 2nd ed. (Cambridge University Press, New York, 1992).

[27] J. Kessler and F. Thieme, Surface Science **67**, 405 (1977).

[28] J. M. MacLaren, J. B. Pendry, P. J. Rous, D. K. Saldin, G. A. Somorjai, M. A. Van Hove, and D. D. Vvedensky, *Surface Crystallographic Information Service: A Handbook of Surface Structures* (D. Reidel Publishing Company, Boston, 1987).

[29] S. Bao, R. Xu, C. Y. Xu, H. Y. Li, L. Zhu, and Y. B. Xu, "HREELS and ARUPS investigation of the coadsorption of CO and K on Cu(111)," Surface Science **271**, 513-518 (1992).

[30] G. Herzberg, *Molecular Spectra and Molecular Structure II. Infrared and Raman Spectra of Polyatomic Molecules* (Van Nostrand Reinhold Company, New York, 1945).

[31] S. D. Kevan, R. F. Davis, D. H. Rosenblatt, J. G. Tobin, M. G. Mason, D. A. Shirley, C. H. Li, and S. Y. Tong, "Structural Determination of Molecular Overlayer Systems with Normal Photoelectron Diffraction: c(2x2) CO-Ni(001) and ($\sqrt{3}$x$\sqrt{3}$)R30 CO-Ni(111)," Physical Review Letters **46** (25), 1629-1632 (1981).

[32] Z. Q. Huang, Z. Hussain, W. R. A. Huff, E. J. Moler, and D. A. Shirley, "Structural determination of p2mg(2x1)CO/Ni(110) with the use of angle-resolved photoemission extended fine structure," Physical Review B **48** (3), 1696-1710 (1993).

[33] P. R. Bevington, *Data Reduction and Error Analysis for the Physical Sciences* (McGraw-Hill, San Francisco, 1969).

LEED Structure	C-Cu Bond Length	First Cu-Cu Layer Spacing
clean Cu(111) metal	------------	2.07(2) Å[28]
($\sqrt{3}$ x $\sqrt{3}$) R30°	1.91(1) Å	2.07(3) Å
(1.5 x 1.5) R18°	1.91(2) Å	2.01(4) Å

Table I.
Summary of bond lengths and layer spacings for two different coverage phases of CO/Cu(111) determined in this work from best fit to MSSW calculations. The statistical errors for the last reported digit are given in parentheses.

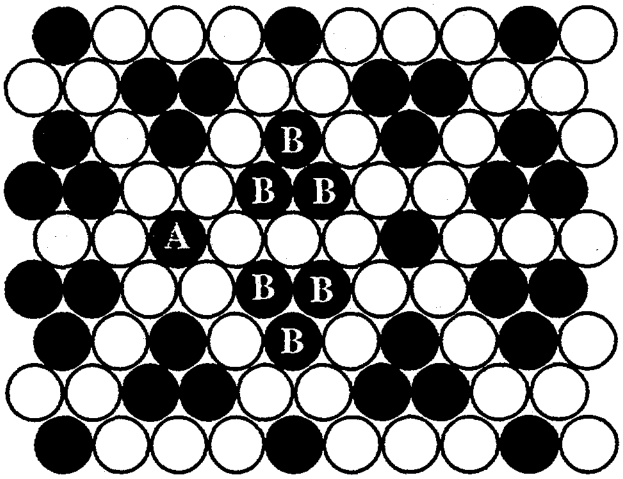

Figure 1.

Adsorption site structure of the (1.5 x 1.5)R18° LEED phase proposed by Raval, et. al.[8]. The open circles are copper atoms with no CO molecule adsorbed. There are two inequivalent atop adsorption site types labeled A and B and are shown in gray and black, respectively.

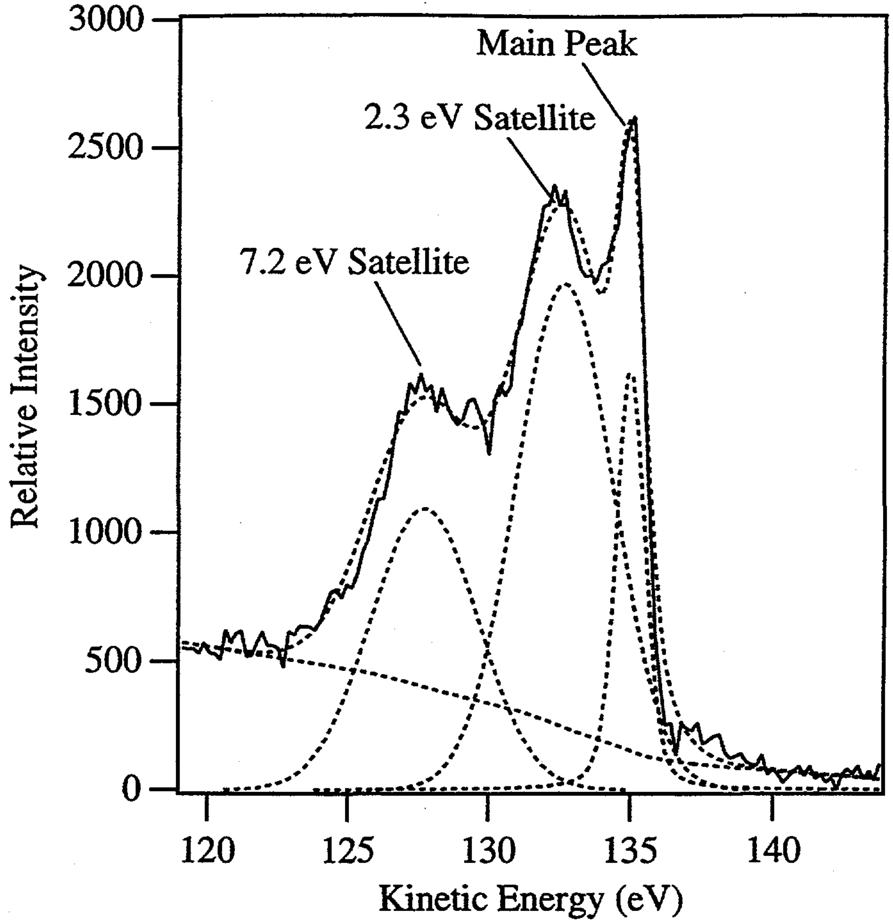

Figure 2.
Typical carbon 1s XPS spectrum for this work. The solid line is the experimental data. The dashed lines are the best fit and the deconvolved components.

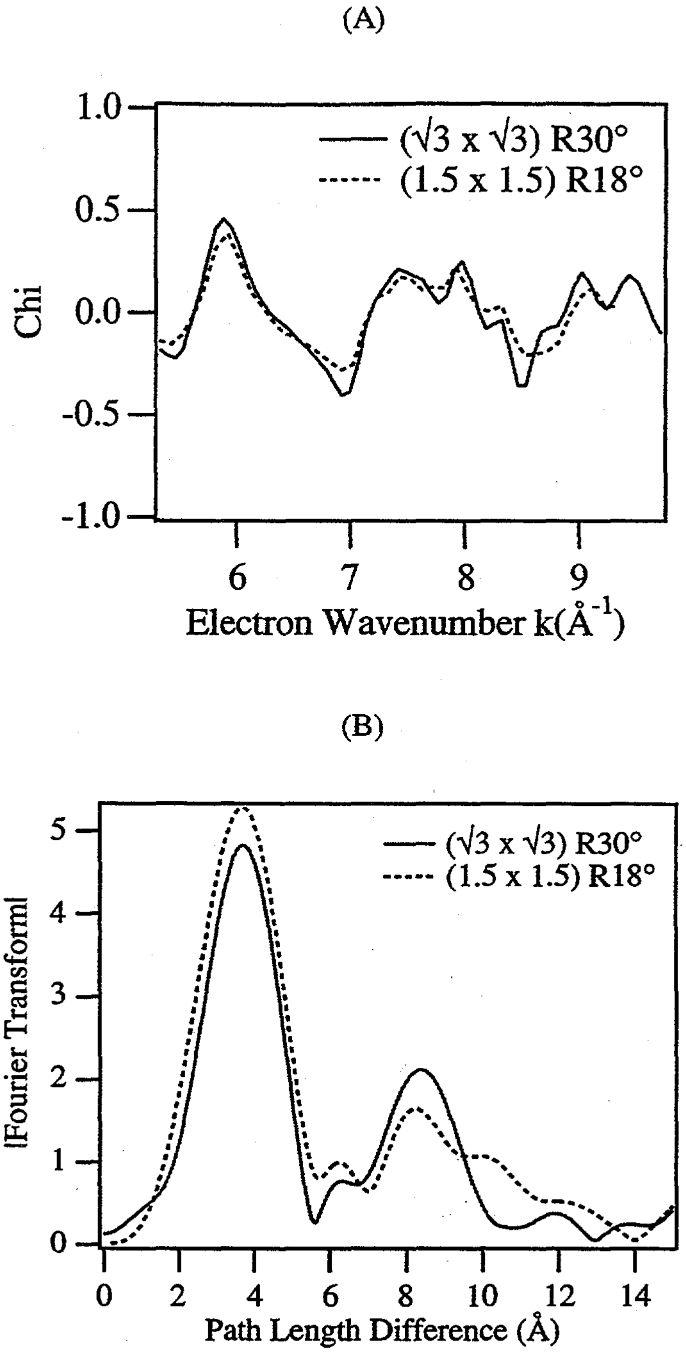

Figure 3.
Experimental carbon 1s ARPEFS curves (A) and their Fourier transforms (B) for the two lowest coverage phases of CO/Cu(111). The dominant peaks in (B) at ~3.8 Å and ~8.5 Å are assigned to single-scattering events from the nearest first- and second-layer copper atoms, respectively.

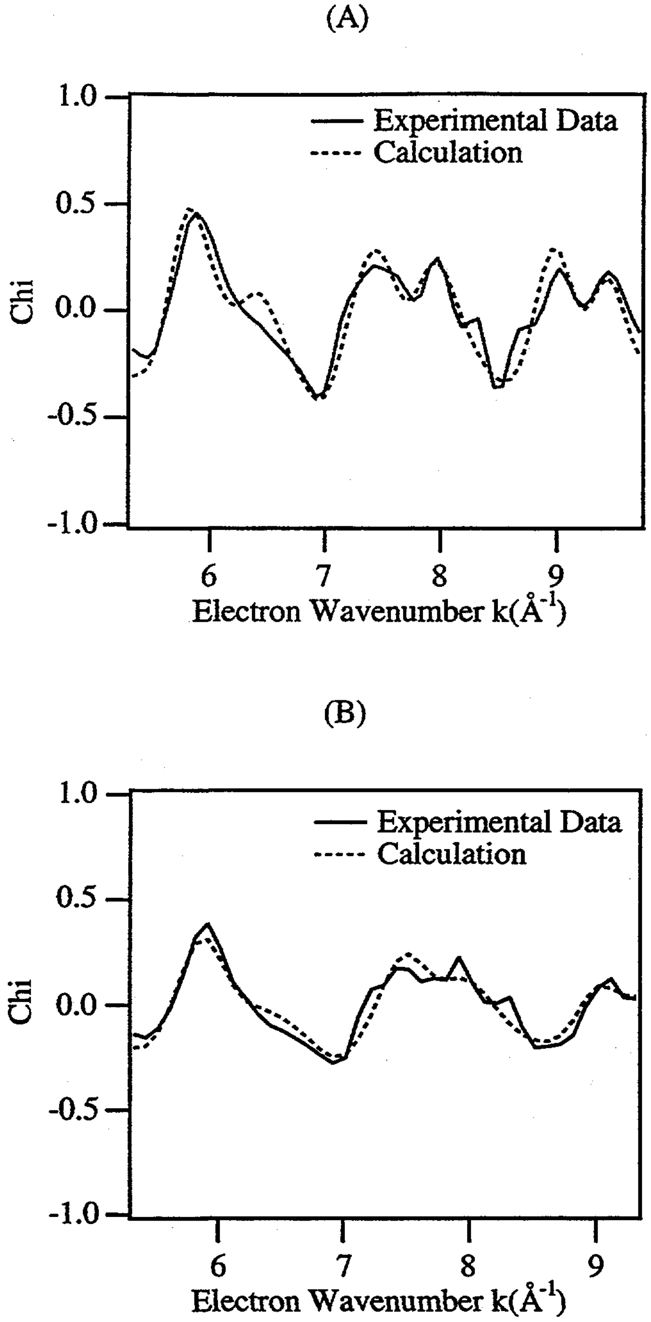

figure 4.

Comparison of experimental carbon 1s ARPEFS curves and MSSW calculations for (A) the $(\sqrt{3} \times \sqrt{3})$ R30° and (B) the (1.5 x 1.5) R18° CO/ overlayers on Cu(111). The R-factor between each experimental and calculated curve is 0.12. See text for structural parameters.

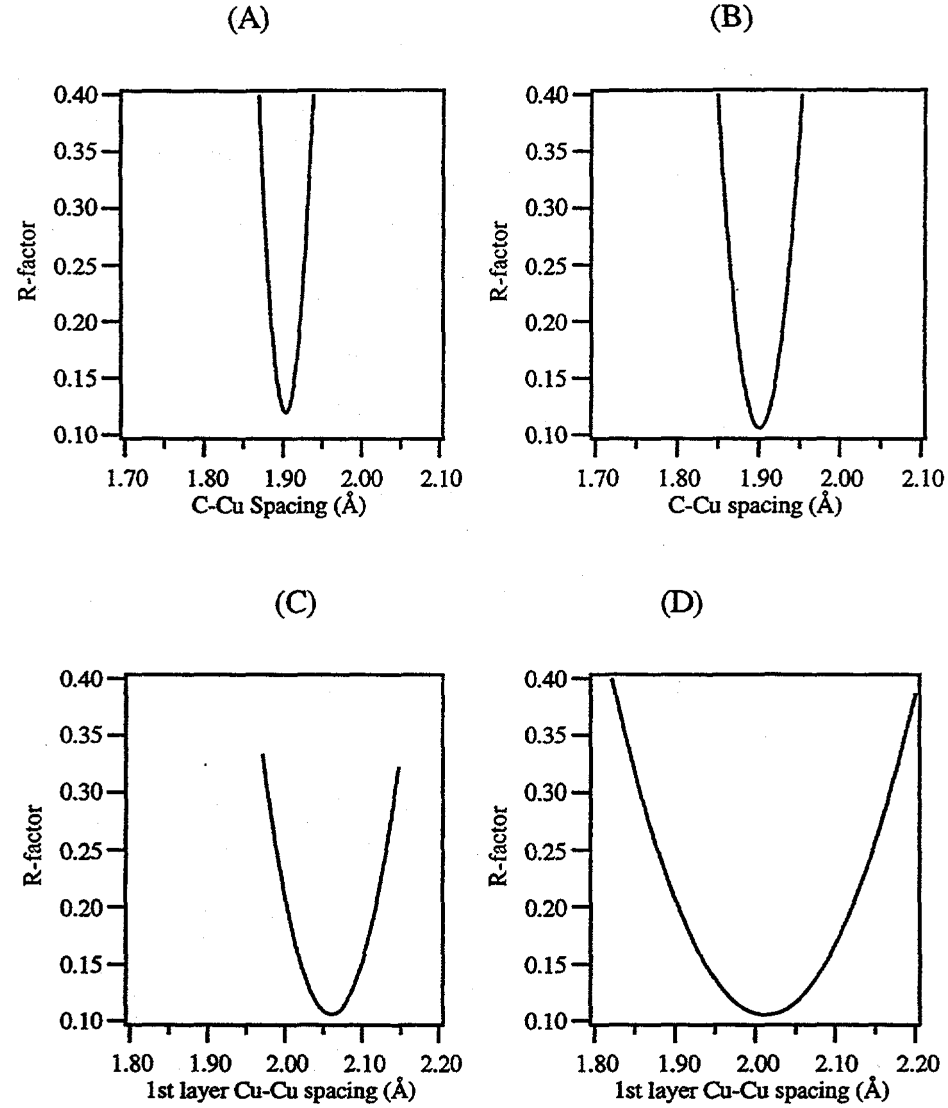

Figure 5.
R-factor curves vs. interlayer spacing. (A) C-Cu spacing for (√3 x √3) R30° , (B) C-Cu spacing for (1.5 x 1.5) R18°, (C) first Cu-Cu layer spacing for (√3 x √3) R30° , (D) first Cu-Cu layer spacing for (1.5 x 1.5) R18°. The statistical uncertainty of each interlayer spacing is determined from the curvature of the R-factor plot to be ± 0.01, 0.02, 0.03, and 0.04 Å for (A), (B), (C), and (D), respectively (see text).

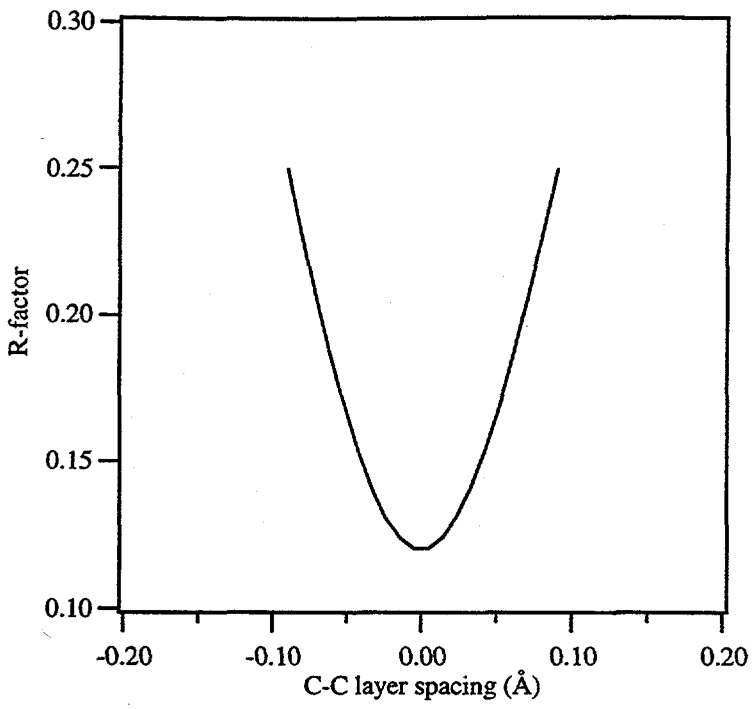

Figure 6.
R-factor vs. carbon-carbon (A-B) layer spacing. The B-type layer is fixed at 1.91 Å from the 1st copper layer. The A-layer distance from the B-layer along the surface normal is the abscissa.

Adsorption Site and Structure Determination of c(2x2) N_2/Ni(100) using Angle-Resolved Photoemission Extended Fine Structure

Abstract

We have determined the atomic spatial structure of c(2x2) N2/Ni(100) with Angle-Resolved Photoemission Extended Fine Structure (ARPEFS) using the nitrogen 1s core level. The chemically shifted N 1s peak intensities were summed together to obtain ARPEFS curves for both nitrogen atoms in the molecule. We used a new, highly-optimized program based on the Rehr-Albers scattering matrix formalism to find the adsorption site and to quantitatively determine the bond-lengths. The nitrogen molecule stands upright at an atop site, with a N-Ni bond length of 2.25(1) Å, a N-N bond length of 1.10(7) Å, and a first layer Ni-Ni spacing of 1.76(4) Å. The shake-up peak shows an identical ARPEFS diffraction pattern, confirming its intrinsic nature and supporting a previous use of this feature to decompose the peak into contributions from the chemically inequivalent nitrogen atoms. Comparison to a previously published theoretical treatment of N-N-Ni and experimental structures of analogous adsorbate systems demonstrates the importance of adsorbate-adsorbate interactions in weakly chemisorbed systems.

Introduction

Angle-Resolved Photoemission Extended Fine Structure (ARPEFS) is a well established technique for determining the spatial structure of atomic and molecular adsorbates on metal surfaces[1-3]. One of the advantages of the technique is its elemental selectivity due to the unique binding energies of core electrons. We have used ARPEFS to determine the adsorption site and bond lengths of C(2x2) molecular nitrogen on Ni(100).

This system has been the subject of several investigations, as it represents an analogue to the prototypical CO adsorbate on transition-metal surfaces. Stöhr and Jaeger determined that N_2 stands up normal to the surface on Ni(100)[4]. Grunze and Dowben established that molecular nitrogen forms a C(2x2) LEED pattern on Ni(100)[5]. Subsequent TPD studies indicated that only one adsorption site was occupied by N_2 at saturated coverages ($\approx$0.5 monolayer) for well ordered overlayers, even those with somewhat diffuse LEED patterns[6]. Nilsson and Mårtensson found two sharp peaks in the photoemission spectrum of the N 1s core-level corresponding to the two chemically inequivalent nitrogen atoms in the molecular adsorbate[7]. They also investigated the broad satellite peak 6 eV below the main peaks and concluded that it was a shake-up peak associated with final-state molecular excitations. Their analysis of the shake-up satellite was based on the implicit assumption that the satellite peak showed identical scattering characteristics as the main peak. This assumption has not been previously established.

In this paper we report an experimental determination of the adsorption site, the the N-N and N-Ni bond lengths, and the first Ni-Ni layer spacing. We also show that the shake-up peak associated with the nitrogen 1s core level displays an identical diffraction pattern as the main peak. We found that it is not necessary to resolve the chemically shifted peaks to determine the adsorbate structure.

Experiment

The experiments were performed using the high resolution Spherical Grating Monochromator (SGM) on beam line 6-1 at the Stanford Synchrotron Radiation Laboratory (SSRL). Photon energies from 480-700 eV were utilized. The UHV vacuum chamber was equipped with a 5 cm hemispherical electron energy analyzer, a liquid helium cooled sample manipulator, a LEED/Auger system, and an ion-sputtering gun. The bulk nickel substrate was cleaned by sputtering, annealing, and roasting in oxygen. The final surface cleaning was done by dosing O_2 at 3×10^{-9} torr for 20 seconds with the sample at 450° C. Sample cleanliness was monitored by XPS and sample order was checked by LEED. The nickel crystal was oriented by laser autocollimation, angular scanned photoemission along [110], and LEED. The C(2x2) N_2 overlayer was prepared by back-filling the chamber to 1×10^{-8} torr while cooling the sample from 140 K to 75 K at a rate of ~.12 K/s. The order of the overlayer was checked with LEED on trial preparations. LEED was not done on the overlayers used to take the ARPEFS curves, to avoid damage from electron bombardment. NEXAFS was used to confirm that the molecules were indeed standing up on the surface. The sample was free of measurable contamination, but we observed an accumulation of oxygen on the surface at a rate of approximately 3% monolayer/hour. Thus, we cleaned the surface and prepared a new overlayer after 1.5 hours with a single overlayer. The synchrotron radiation was incident on the sample at 25° between the electric vector and the sample normal and the photo-emission direction was 5° off the normal to the nickel(100) surface towards the [110] direction. The UHV chamber pressure was $<3 \times 10^{-10}$ torr. The sample temperature was 75 K as measured by a thermocouple spot-welded near the sample.

Surface Structure Determination

Figure 1 shows a typical photoemission spectrum and its deconvolution into three peaks. Nilsson and Mårtensson showed that the two lower binding energy peaks are due to the two chemically inequivalent nitrogen atoms[7]. The lowest binding energy peak is due to the nitrogen atom furthest from the nickel substrate. We call this nitrogen the "outer nitrogen" and the corresponding peak ,"peak 1." The next lowest binding energy peak is due to the nitrogen atom closest to the nickel surface. We call this nitrogen the "inner nitrogen" and the corresponding peak, "peak 2." Nilsson and Mårtensson measured the splitting between these peaks to be 1.33 eV. They also determined that the broad satellite peak approximately 6 eV below the two has contributions from both higher kinetic energy peaks using normal and off-normal emission. The peak intensities were extracted by fitting all three peaks with Voigt functions and normalized to the background the in the standard method[1]. We obtained the total ARPEFS diffraction curve by summing the intensities of peaks 1 and 2.

We have performed full Multiple Scattering Spherical Wave (MSSW) calculations using the formalism of Rehr and Albers[8] to determine the best match of adsorption site and bond lengths to the experimental ARPEFS χ-curve. The program, developed entirely within our group, is highly optimized for obtaining a best fit to experimental data including multiple emitters[9]. It uses second order matrices (6x6) and up to 8th order scattering, which produce a convergent calculation at these energies and inter-atomic distances. The best fit was defined by the conventional R-factor analysis[1]. We show the experimental chi-curve and the best fit for each of the three adsorption sites in figure 2. To obtain these fits we allowed the N-N and N-Ni distances and the spacing between the first two nickel layers to vary. We also allowed the inner potential, the Debye temperatures of the near surface layers, and the tilt of the N-N molecule to vary. Clearly the atop site is the best fit, with an R-factor of 0.34. The N-Ni bond length is found to be 2.25 Å and the N-N bond length is found to be the gas-phase nitrogen value of 1.10 Å. Interestingly, the spacing between the first two nickel layers is found to be the bulk nickel value of 1.76 Å, in contrast to the contracted clean-metal layer spacing of 1.60 Å[10]. A surface debye temperature of 220 K and an inner potential of 15.1 eV were found to give the best fit.

To examine the sensitivity to the layer spacings and establish error bars we calculated the R-factor for various interlayer spacings and inner potentials. It has been shown that the inner potential may affect the derived layer spacings and must be included in the R-factor analysis[11]. The uncertainty is reported as one standard deviation, i.e. a confidence level of 0.68, and is written in parentheses following the last significant digit. Figures 3 and 4 show the R-factor contours for the N-Ni layer spacing and inner potential and the first layer Ni-Ni spacing, respectively. The R-factor result for the nitrogen-nitrogen bond length is shown in figure 5, with the inner potential was held constant at 15.1 eV. Extraction of the error bars from the R-factor analysis has been discussed previously[12]. We conclude from these analyses that the error in the N-Ni layer spacing is 0.01 Å , the Ni-Ni layer spacing is 0.04 Å, and the N-N bond length is 0.07 Å.

The Satellite Peak

An interesting feature of the photoemission spectra is the broad, intense peak at 6 eV below the main peaks. Nilsson and Mårtensson assigned this peak as an intrinsic satellite feature, and shows that it contains contributions from both of the main peaks by spectrum subtraction, making use of the variation in peak intensities with emission angle[7]. In figure 6 we compare the χ-curve of the sum of peaks 1 and 2 to the χ-curve of peak 3. These two curves are each plotted against the k-value of the corresponding (sum) peak. The peak 3 chi-curve follows the summed main peak chi-curves very closely, showing that it displays an identical ARPEFS diffraction pattern as the main peaks, including identical amplitudes. We infer that the 6 eV peak arises from intrinsic satellite structures, each having the same intensity ratio as its main peak.

Discussion

In this work we have shown that the nitrogen adsorbs on an atop site with a nitrogen-nickel bond length of 2.25 Å, with approximatedly the gas phase nitrogen-nitrogen bond length and bulk nickel-nickel layer spacing. We now examine the bonding characteristics in the context of theoretical predictions and in comparison to related adsorbate systems. The bonding is qualitatively described by the molecular nitrogen donating electrons to the nickel from its HOMO $3\sigma_g$ orbital and accepting electrons into the LUMO $1\pi_g^*$ orbital from the nickel 3d orbitals[13]. There is a repulsive interaction between the $3\sigma_g$ occupied level and the metal electrons. The electron accepted into the $1\pi_g^*$ is thought to stabilize the $3\sigma_g$ interaction by creating a partial positive charge on the metal atom. The induced dipole is then attractive to the $3\sigma_g$ electrons. The relative importance of molecular bonding and mutually induced dipole interactions remains to be clarified. This model also ignores adsorbate-adsorbate interactions, which may occur both directly and through the substrate.

There have been several ab-initio calculations published for the N-N-Ni system examining the bonding characteristics of the molecular nitrogen-metal system [14-16]. The investigations of Freund, et. al., found a minimum total energy at a N-Ni bond length of 1.64 Å for a $3d^{10}$ configuration nickel atom and 1.96 Å for a $3d^9 4s$ configuration. They found that the $3d^{10}$ configuration led to a better match to the calculated core-level splitting between the two inequivalent nitrogen atoms. These calculations clearly overestimate the molecule-metal interaction strengths for the saturated overlayer. The large discrepancy between our measured N-Ni bond lengths of 2.25 Å and the theoretical predictions of 1.96 Å underscores the importance of including the effects of other interactions with the surface layer metal atoms and other neighboring molecules. This is not surprising considering that Varma and Dowben have shown that there are strong lateral interactions between nitrogen molecules in the ordered c(2x2) overlayer[6].

It is useful to compare our results to the structure of the related systems, c(2x2) CO/Ni(100) and low-coverage NH_3/Ni(100). The CO molecule adsorbs on Ni(100) in an atop site with a C-Ni layer spacing of 1.80 Å[17]. The first-layer Ni-Ni spacing was assumed to be the bulk value in that analysis. The heat of adsorption of CO on Ni(100) is 122(2) kJ/mole at low coverage and drops to 100(2) kJ/mole at high coverage[17]. The heat of adsorption of N_2/Ni(100) is much lower, 45(4) kJ/mole to 25(2) kJ/mole[5], which is consistent with the longer N-Ni bond length. The bonding scheme for CO to Ni(100) is expected to be analogous to N_2. The relatively large N-Ni bond length is consistent with the molecular orbital interaction picture. The CO molecule has a stronger covalent interaction with the metal surface due to the concentration of the $2\pi^*$ antibonding orbital on the carbon and the greater oxygen character of the 5σ donor orbital. This enhances the orbital overlap relative to the N_2 MO's and results in a stronger bond with shorter bond length.

The NH_3/Ni(100) also adsorbs on an atop site with an N-Ni spacing of 2.01 Å and an Ni-Ni layer spacing of 1.81 Å[18]. The spacing for that system was determined at low coverage. The bonding scheme of the ammonia is understood to be a σ donation to the metal and a large electrostatic interaction between the ammonia dipole and the metal atoms[19]. Considering the electrostatic interactions, the larger N-Ni spacing for N_2 is expected, as there is no molecular dipole and the N_2 molecule has a low polarizability relative to the ammonia, 1.74×10^{-24} vs. 2.26×10^{-24} cm^3, respectively[20]. The expansion of the initially contracted clean metal surface has not been investigated theoretically for either the NH_3 or the N_2 adsorbate systems. We note that the more strongly interacting ammonia adsorbate leads to a greater expansion of the surface nickel layer than the molecular nitrogen from the clean metal 1st layer Ni-Ni spacing of 1.60 Å.

It is clear that the interaction of the molecular nitrogen overlayer with the surface is very weak. There is neither a strong covalent interaction nor an electrostatic one. The weak-chemisorption picture analogous to CO is supported by the analysis of the core-level photoemission satellites[7,15] and valence level UPS[21]. The weak interaction with the metal substrate emphasizes the importance of lateral interactions among adsorbates. A quantitative theoretical treatment will need to include adsorbate-adsorbate interactions and possibly sub-surface nickel layers.

Conclusion

We have measured the nitrogen 1s ARPEFS oscillations from c(2x2) N_2/Ni(100). We find that the nitrogen molecule adsorbs in an atop site with the N-N bond normal to the surface with a N-N length of 1.10(7) Å. The N-Ni bond length is 2.25(1) Å and the first Ni-Ni layer spacing is 1.76(4) Å . The satellite peak intensity shows the same chi curve as the sum of the two main peaks, confirming that the component satellite peaks are intrinsic, and with the same intensity ratio as the main peaks. Comparison with theoretical treatments of the N-N-Ni system and experimental structures of analogous adsorbate systems suggests that a quantitative theoretical treatment of weakly adsorbed systems must include lateral interactions between adsorbates.

Bibliography

[1] J. J. Barton, C. C. Bahr, C. C. Robey, Z. Hussain, E. Umbach, and D. A. Shirley, Physical Review B **15**, 3807 (1986).

[2] C. C. Bahr, J. J. Barton, Z. Hussain, S. W. Robey, J. G. Tobin, and D. A. Shirley, Physical Review B **35**, 3773 (1987).

[3] L. G. Terminello, X. S. Zhang, S. Kim, A. E. Schach von Wittenau, K. T. Leung, and D. A. Shirley, Physical Review B **38**, 3879 (1988).

[4] J. Stöhr and R. Jaeger, Physical Review B **26**, 4111 (1982).

[5] M. Grunze, P. A. Dowben, and R. G. Jones, "Thermodynamic Measurements for N2 Adsorption on Ni(100)," Surface Science **141**, 455-472 (1984).

[6] Shikha Varma and P. A. Dowben, "The effect of lateral interactions on the thermal desorption of N2 from Ni(100)," Journal of Vacuum Science and Technology A **8** (3), 2605 (1990).

[7] Anders Nilsson, Helena Tillborg, and Nils Martensson, "Electronic Structure of Adsorbates from Core-level Shake-up Spectra: N2 on Ni(100)," Physical Review Letters **67** (8), 1015 (1991).

[8] J. Rehr and Albers, Physical Review B **41**, 8139 (1990).

[9] to be published.

[10] J. W. M. Frenken and J. F. van der Veen, "Relation between Surface Relaxation and Surface Force Constants in Clean and Oxygen-Covered Ni(001)," Physical Review Letters **51** (20), 1876-1879 (1983).

[11] W. R. A. Huff, Y. Zheng, Z. Hussain, and D. A. Shirley, Journal of Physical Chemistry **98**, 9182-9186 (1994).

[12] Z. Huang, "Structural Studies of Molecular Metallic Overlayers Using Angle-Resolved Photoemission Extended Fine Structure," Ph. D. Thesis, University of California, Berkeley, 1992.

[13] C. N. R. Rao and G. R. Rao, "Nature of nitrogen adsorbed on transition metal surfaces as revealed by electron spectroscopy and cognate techniques," Surface Science Reports **13** (7) (1991).

[14] C. R. Brundle, P. S. Bagus, D. Menzel, and K. Hermann, "Adsorption of molecular nitrogen on nickel. II. Comparisons of photoemission for N2/Ni(100) to CO/Ni(100) and to theory," Physical Review B **24** (12), 7041-7056 (1981).

[15] H. J. Freund, R. P. Messmer, C. M. Kao, and E. W. Plummer, "Interpretation of the N 1s photoelectron spectra of chemisorbed N2 in terms of local molecule-metal interaction," Physical Review B **31** (8), 4848-4853 (1985).

[16] C. M. Kao and R. P. Messmer, "Ab intio cluster-model study of the electronic ground state and photoemission properties of NiN2 and NiCO: Models for chemisoption," Physical Review B **31** (8), 4835-4847 (1985).

[17] J. T. Stuckless, N. Al-Sarraf, C. Wartnaby, and D. A. King, "Calorimetric heats of adsroption for CO on nickel single crystal surfaces," Journal of Chemical Physics **99** (3), 2202-2212 (1993).

[18] Y. Zheng, E. J. Moler, E. A. Hudson, and D. A. Shirley, "Structural determination of NH3 adsorbed on Ni(100) using angle-resolved photoemission extended fine-structure spectroscopy," Physical Review B **48** (7), 4760-4766 (1993).

[19] C. W. Bauschlicher, "H20/Ni(100) and NH3/Ni(100): A computational approach," Journal of Chemical Physics **83** (6), 3129-3133 (1985).

[20] R. C. Weast, J. A. Melvin, and H. B. William, "CRC Handbook of Chemistry and Physics," (CRC Press, Inc., Boca Raton, Florida, 1988).

[21] P. A. Dowben, Y. Sakisaka, and T. N. Rhodin, "Angle-Resolved Photoemission from Molecular N2 Adsorbed on Ni(100)," Surface Science **147**, 89-102 (1984).

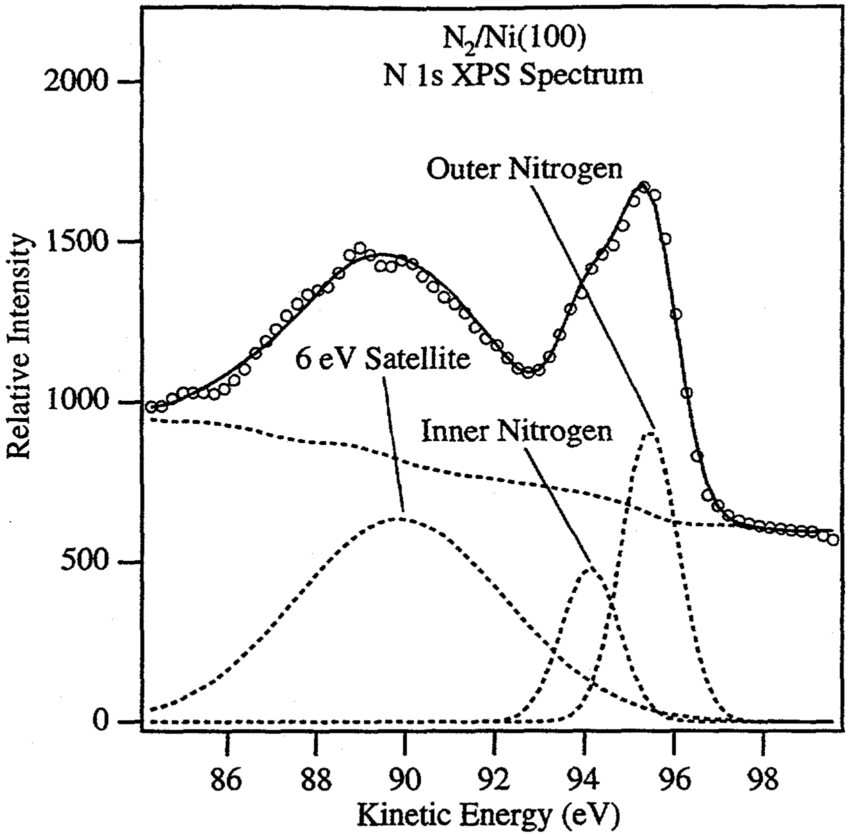

Figure 1.
Typical XPS spectrum of c(2x2) N_2/Ni(100) for this work. The circles are the data points, the dashed lines are the deconvolved fit to the data, and the solid line is the total fit. See the text for explanation of "outer" and "inner" nitrogen peaks.

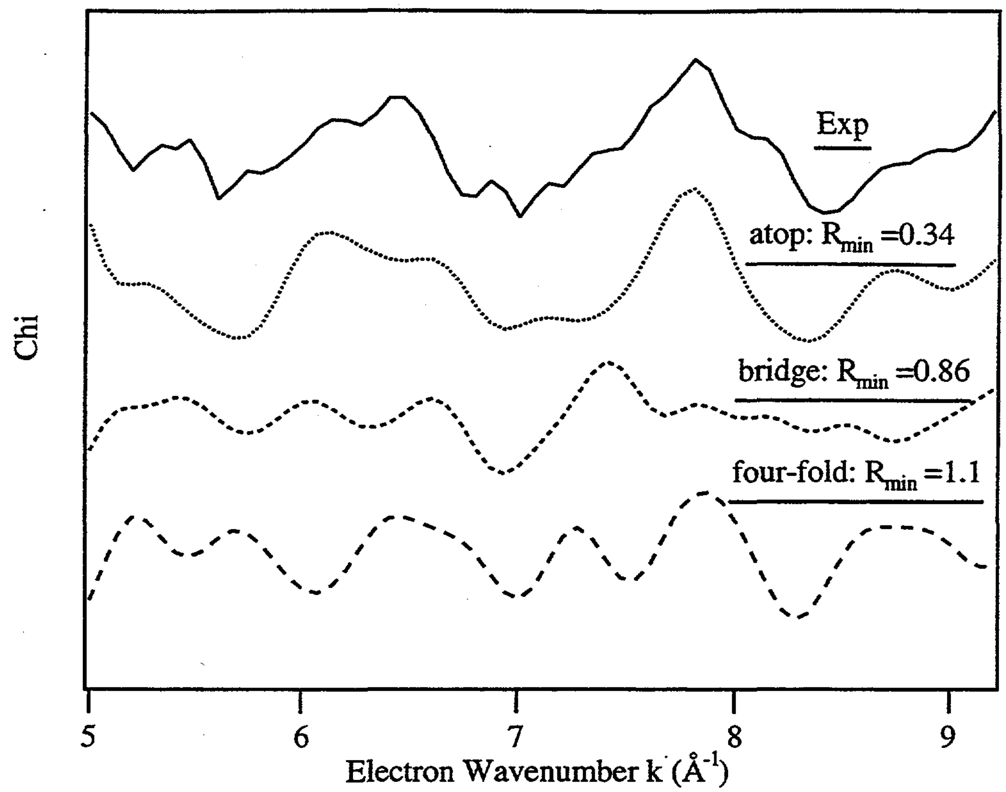

Figure 2.
Experimental ARPEFS curve and best fit calculation for each adsorption site. The experimental curve is derived from the sum of the intensities from the two main peaks in the XPS spectrum. Clearly the atop adsorption site gives the best fit with an R-factor of 0.34.

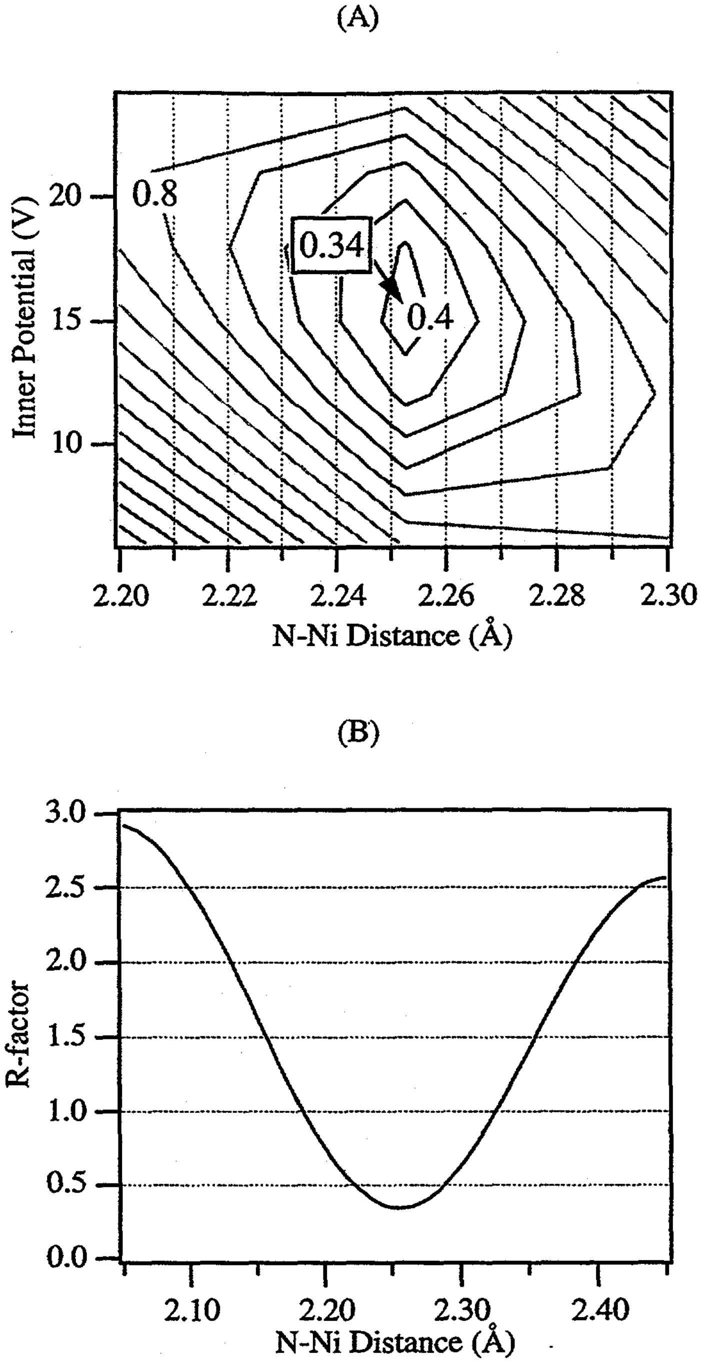

Figure 3.
(A) R-factor vs. inner potential and N-Ni layer spacing. The minimum is at a layer spacing of 2.255 Å. (B) R-factor vs. N-Ni layer spacing with inner potential fixed at 15.1 eV.

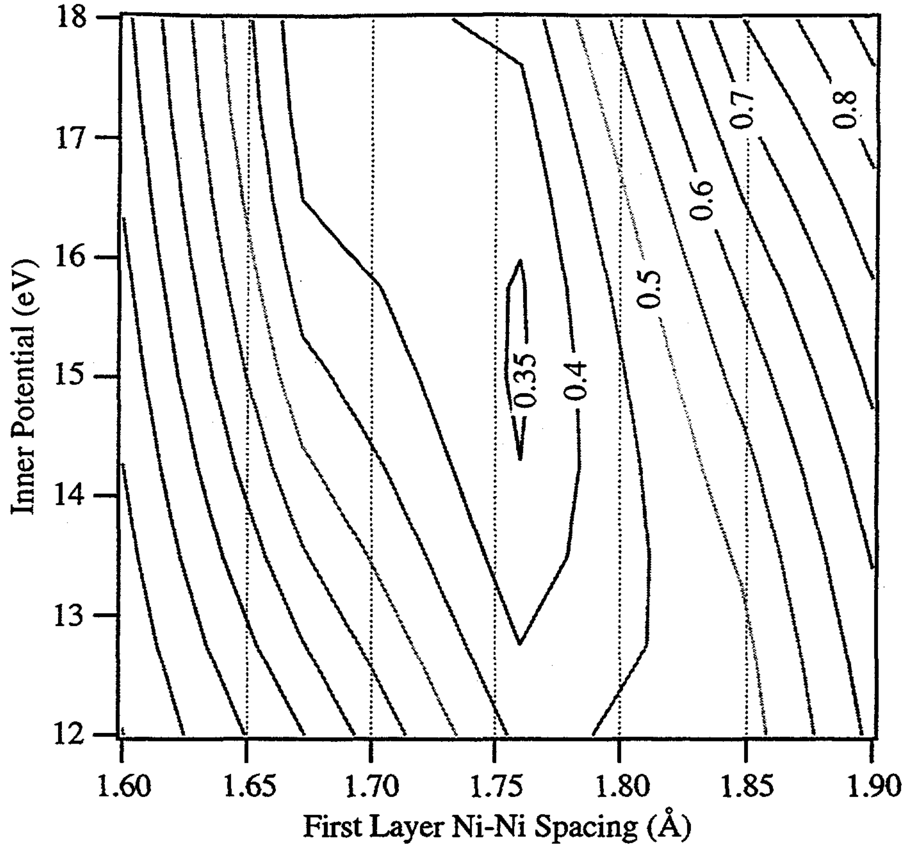

Figure 4.
R-factor vs. inner potential and spacing between the first and second nickel layers.

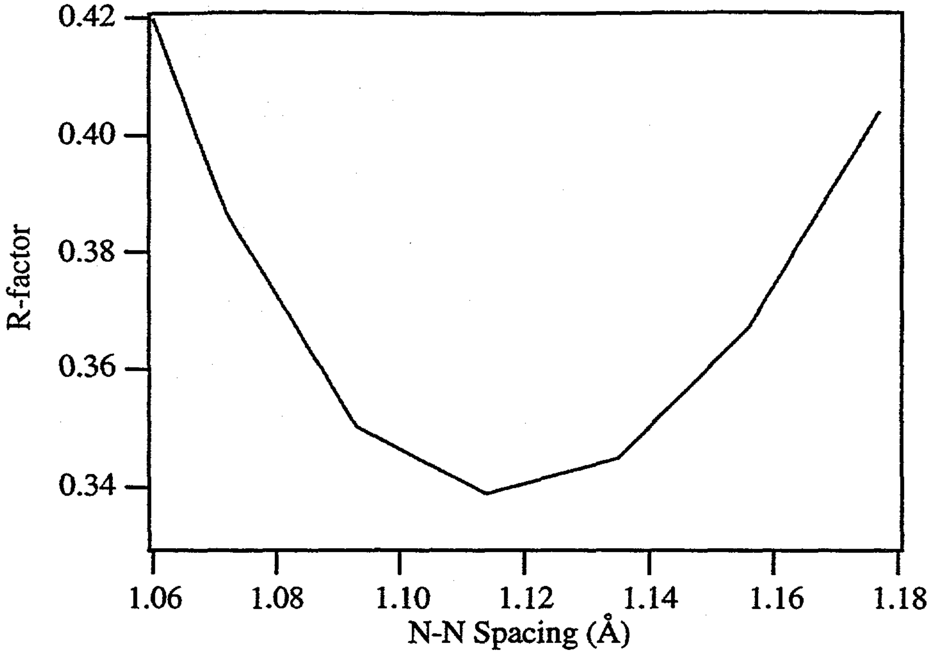

Figure 5.
R-factor vs. nitrogen-nitrogen bond length. The inner potential is fixed at 15.1 eV

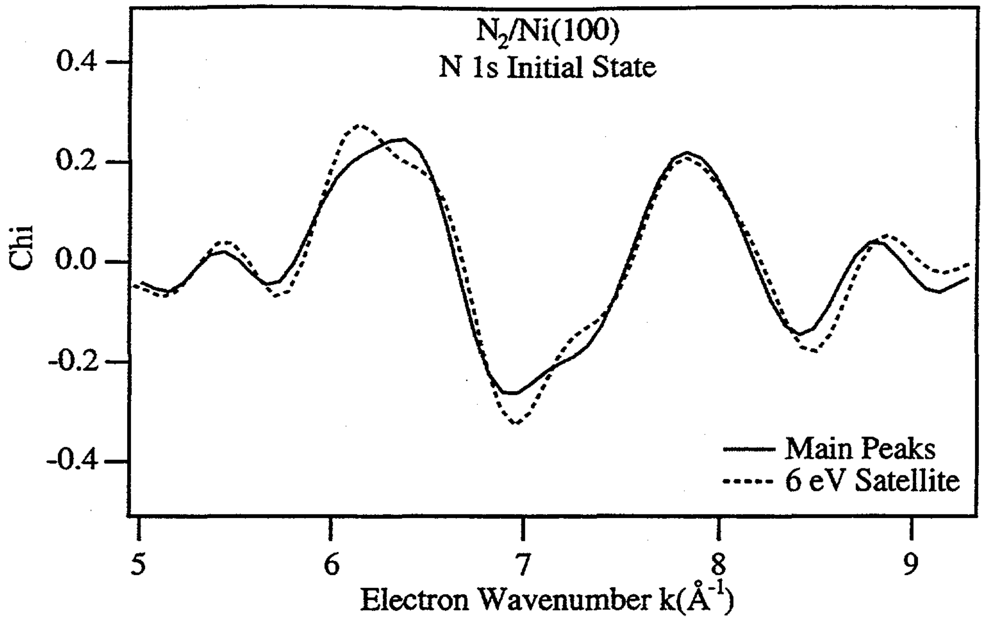

Figure 6.
Comparison of ARPEFS chi-curves for the main peaks and the satellite peak. The curves have been Fourier smoothed to a 13 Å cutoff to facilitate comparison.

Evidence of the Nature of Core Level Photoemission Satellites using Angle-Resolved Photoemission Extended Fine Structure

Abstract

The origin of photoemission satellites in core level spectra of clean and molecular adsorbate covered transition metals is still open to debate, despite intense experimental and theoretical activity, largely because of the difficulty in disentangling the processes which may possibly occur in photoemission . In this paper we present a unique method of experimentally determining the angular momentum and intrinsic/extrinsic origin of core-level satellites by examining the satellite diffraction pattern in the Angle Resolved Photoemission Extended Fine Structure (ARPEFS) mode. We show for the first time that satellite peaks not associated with chemically differentiated atomic species display an ARPEFS intensity oscillation. Specifically, we present data for the C 1s from $(\sqrt{3}x\sqrt{3})R30$ CO/Cu(111) and p2mg(2x1)CO/Ni(110), N 1s from c(2x2) N_2/Ni(100), and Ni 3p from clean nickel(111). The satellite peaks in all cases exhibit ARPEFS curves which indicate an angular momentum identical to the main peak and are of an intrinsic nature.

Paper

The nature of core level photoemission satellites from clean metals has been an active area of investigation for many years[1-10]. More recently, the interpretation of satellites from molecular adsorbates on metal surfaces have been employed as a probe into the nature of the surface chemical bond on a variety of systems[11-17]. Generally, these satellites are interpreted as correlated excitations of valence level electrons into either unoccupied bound states (shake-up or electron-hole pair excitations) or into the continuum (shake-off) which are associated in some way with the photoemission process. There are, however, open questions regarding the nature of these satellite structures.

Two questions often arise in the interpretation of core-level satellites in solid and adsorbate systems. One question is whether the peak is intrinsic, i.e. a shake-up or shake-off peak, or extrinsic, from an inelastic scattering process encountered before the electron leaves the solid,e.g. a plasmon loss. The second question concerns the character of the valence excitation, which can be to a HOMO-LUMO type transition, for example, or an excitation into a rydberg-like state. We show in this paper that both of these questions can be approached by examining the Angle Resolved Photoemission Extended Fine Structure (ARPEFS) curves associated with the main peak and its satellites. ARPEFS is a well known technique for finding the spatial atomic structure of surfaces to very high accuracy [18]. It is based on measuring the intensity of a core level photoelectron with an angle-resolved electron energy analyzer while varying the electron kinetic energy. We have found that the satellite structures not associated with a chemically differentiated atomic species can display an ARPEFS diffraction pattern and can thus be used to infer certain features of the origin of these peaks.

The XPS spectrum and ARPEFS curves for C 1s from ($\sqrt{3}$x$\sqrt{3}$)R30 CO/Cu(111), N 1s from c(2x2) N_2/Ni(100), and Ni 3p from clean nickel(111) are shown in Fig. 1 and 2. The CO/Cu(111) experiment was performed on beam line 9.3.2 at the Advanced Light Source at Lawrence Berkeley National Laboratory. The N_2/Ni(100) experiment was performed on beam line 6.1 at the Stanford Synchrotron Radiation Laboratory. The clean nickel and CO/Ni(110) experiments were performed using beam line U3-C at the National Synchrotron Light Source at Brookhaven National Laboratory. The samples were cleaned and prepared using standard UHV surface science techniques and were cooled to 80-100 K for the molecular adsorbates and ~120 K for the clean nickel. The x-ray angle of incidence on the sample ranged from 10-35° and the emission direction was normal for all experiments. We were careful to not damage the adsorbate systems by checking the LEED pattern only briefly near the edge of the sample. It is known that the nitrogen molecule stands up on end atop a nickel atom on the surface[19,20]. Similarly, the CO is known to occupy only atop sites in the ($\sqrt{3}$x$\sqrt{3}$)R30 structure on Cu(111) from FT-IR and EELS[21] and ARPEFS[20]. The CO molecule in p2mg(2x1)CO/Ni(110) occupies an atop site but is tilted by 17° away from the normal[22].

An example XPS spectra for each system is shown in Fig. 1 and 2. The experimental data points are shown as circles with the deconvolution and best fit lines drawn in. These fits are used to extract the peak intensities for the ARPEFS curves. The ARPEFS curve, representing the intensity oscillation for each peak in the XPS spectrum, is shown to the right. The abscissa is the electron wave-number, in $Å^{-1}$, for each peak. The N 1s main XPS peak is known to consist of two components, each associated with the nitrogen closest or furthest from the nickel surface[14]. We have summed them to get a net ARPEFS curve. The nickel 3p 1/2 and 3/2 peaks were similarly summed. The C 1s XPS peak in p2mg(2x1)CO/Ni(110) has been shown to have a Doniach-Sunjic lineshape[22,23]. We have extracted the intensity for these spectra by integrating the area above the background across two regions, one centered on the peak and the other at 8 eV lower kinetic energy than the peak. The integration regions are shown with vertical lines. It is clear from the figures that the satellite peaks exhibit the same ARPEFS diffraction pattern as the main peak with the exception of the nickel 13 eV satellite, which will be discussed further below. The ARPEFS curves for the p2mg(2x1)CO/Ni(110) system have been

Fourier smoothed to 10 Å to aid comparison. The small difference between ARPEFS curves at low k in the p2mg(2x1)CO/Ni(110) system can be attributed to the poor counting statistics in the low kinetic-energy tail.

Two important conclusions can be drawn from the similarities between the main and the satellite peak ARPEFS curves. The first is that these peaks must be intrinsic. This stems from the extreme sensitivity of ARPEFS to the position of the outgoing electron wave's origin, which is ~ 0.01 Å. An inelastic scattering event from valence electrons would most likely lead to an outgoing electron wave which is not centered at an equivalent ion core and thus would exhibit a very different diffraction pattern, if any at all. The fact that we find these peaks to be intrinsic is compatible with the interpretation of Tillborg, Nilsson, and Martensson,[12]that the molecular adsorbate satellites are due to shake-up transitions which originate from a single-step process. This interpretation considers the final state of the remaining electrons to be strongly influenced by the newly created core-hole. This state is not an eigenstate of the unperturbed system, leading to a final state which is a sum of the new eigenstates of the adsorbate-plus-core-hole system and thus has significant probability of valence excitations. The nickel 6 eV satellite is also intrinsic. This is consistent with the current understanding its origin as being due to a excitation of a single d-level electron correlated with the 3p core excitation into the continuum, leaving a $3d^9$ valence configuration in the final state[3].

The second conclusion which can be drawn from the similarities in the ARPEFS curves is that the satellite peaks have the same angular momentum as the main peak. The dipole selection rules of photoemission are known to be valid for the main peaks and have been used to successfully model the diffraction curves from many systems. We have modelled those presented in this paper[20]. It is also known that different angular momenta in the final state lead to different and characteristic diffraction curves[24]. The similarity of the ARPEFS curves indicates that the angular momentum of the satellites are the same as that of the main peak. This restricts the valence excitations to monopole transitions for single electrons and a net zero angular momentum change for two electron excitations in these systems. This agrees well with previous theoretical investigations into the 6 eV nickel satellite where a d-d transition is considered the most likely origin of that satellite structure[3]. It has been suggested that there may be excitations to s and d-like Rydberg states in the carbon 1s XPS of c(2x2) CO/Ni(100)[12], which is closely related to the CO/Cu(111) system. It is apparent from our data that there is essentially no angular momentum transfer and that the transitions to np states dominate.

Finally, we examine the apparent difference in the nickel 13 eV satellite from the main and 6 eV peaks. This peak has been attributed to the excitation of two d-band electrons at the 3p resonance energy leaving a $3d^8$ configuration in the final state[1]. In Fig. 3B we show the Fourier transform (FT) spectrum of the three nickel ARPEFS curves. They have been normalized to the same intensity in the first peak. Each FT exhibits peaks at the same nearest neighbor path length differences, but with very different intensities. It is not apparent from the FT whether or not the phase of the 13 eV curve matches that of the others, so we also show the ARPEFS curves which have been Fourier filtered to 3 Å, including only the dominant peak. It has been shown previously that odd-parity final states will give ARPEFS curves which are 180° out of phase with even parity final states[24]. From the filtered curves it is apparent that the final states are of the same parity. The angular momentum of the final state may be either d-like or s-like. The main peak is mostly d-like, in accordance with the atomic radial matrix elements (RME) for nickel[25]. We have performed ARPEFS calculations using both an s-wave final state and the published atomic RME[25]. The results of these calculations are shown in figure 3. While the d-like RME calculation matches the main peak ARPEFS curve very well, the s-wave curve does not. The 13 eV satellite curve also does not match the s-wave final state calculation. The FT of the calculated and the satellite ARPEFS curves are shown at the bottom of figure 4. The similarity of the satellite and d-like FT curves lead us to conclude that the satellite peak is predominately d-like in the final state.

We are left to speculate on the suppressed intensity of oscillations of the 13 eV satellite due to the more distant scatterers. One possible explanation is that the core hole in the presence of the $3d^8$ configuration has a significantly shorter lifetime than the core hole with a $3d^{10}$ or $3d^9$ final state. This would result in a shorter coherence length of the outgoing electron wave, damping the intensity oscillations for more distant scatterers. Further theoretical investigation of the Auger decay mechanisms of the excited state is necessary to evaluate this possibility. We also considered the possibility of the peak being in some way associated with the surface of the metal. However, ARPEFS curves calculated using only the surface layer of atoms as photoemitters does not differ significantly from those of the bulk with many layers of emitters.

In conclusion, we have shown for the first time that photoemission satellite peaks from multi-electron excitations exhibit an ARPEFS diffraction pattern. Examination of this pattern leads to unique information on the angular momentum and intrinsic/extrinsic nature of the satellite. We find that the core level satellite peaks of carbon 1s from $(\sqrt{3}x\sqrt{3})R30$ CO/Cu(111), nitrogen 1s from c(2x2) N_2/Ni(100), and nickel 3p from clean nickel(111) are all intrinsic peaks with final state angular momenta identical to that dictated by the photoemission selection rules. The 13 eV satellite of nickel shows an anomolous suppression of ARPEFS intensity for more distant scatterers.

Bibliography

[1] O. Bjorneholm, J. N. Andersen, C. Wigren, and A. Nilsson, "Resonant photoemission at core-level shake-up thresholds: Valenc-band satellites in nickel," Physical Review B **41** (15), 10408-10412 (1990).

[2] L. C. Davis and L. A. Feldkamp, "New Mechansim for Resonant Photoemission," Physical Review Letters **44** (10), 673-676 (1980).

[3] W. Eberhardt and E. W. Plummer, "Angle-resolved photoemission determination of the band structure and multielectron excitations in Ni," Physical Review B **21** (8), 3245-3255 (1980).

[4] M. Iwan, F. J. Himpsel, and D. E. Eastman, "Two-Electron Resonance at the 3p Threshold of Cu and Ni," Physical Review Letters **43** (24), 1829-1832 (1979).

[5] B. W. Jepsen, F. J. Himpsel, and D. E. Eastman, "Single-step-model analysis of angle-resolved photoemission from Ni(110) and Cu(100)," Physical Review B **26** (8), 4039-4051 (1982).

[6] Y. Liu, Z. Xu, and P. D. Johnson, "Spin-orbit coupling, exchange interaction, and hybridization in the photoexcitation of the Ni 3p core level," Physical Review B **52** (12), R8593-R8596 (1995).

[7] M. F. Lopez, A. Gutierrez, C. Laubschat, and G. Kaindl, "Resonant 3p and 3s Core-Level Photoemission at the 2p Thresholds of Ni and Co Metal," Solid State Communications **94** (8), 673-676 (1995).

[8] Nils Martensson and Borje Johansson, "Valence-Band and Core-Level Satellites in Nickel and Related Elements," Physical Review Letters **45** (6), 482-485 (1980).

[9] Nils Martensson, Ralf Nyholm, and Borje Johansson, "Four-hole satellites in the L3VV Auger and the valenc-band spectra from nickel," Physical Review B **30** (4), 2245-2248 (1984).

[10] G. van der Laan, M. Surman, M. A. Hoyland, C. F. J. Flipse, B. T. Thole, U. Seino, H. Ogasawara, and A. Kotani, "Resonant photoemission at the Ni 2p core level as

a probe of electron correlation effects in nickel," Physical Review B **46** (15), 9336-9340 (1992).

[11] H. Ueba, "Theory of core-hole-decay dynamics of adsorbates on metal surfaces: Role of the $2\pi^*$ level of a chemisorbed CO molecule," Physical Review B **45** (7), 3755-3768 (1992).

[12] Helena Tillborg, Anders Nilsson, and Nils Martensson, "Shake-up and shake-off structures in core level photoemission spectra from adsorbates," Journal of Electron Spectroscopy and Related Phenomena **62**, 73-93 (1993).

[13] D. Lovric and B. Gumhalter, "Extra-adsorbate screening in XPS of C 1s core levels of CO/Cu," Surface Science **278**, 108 (1992).

[14] Anders Nilsson, Helena Tillborg, and Nils Martensson, "Electronic Structure of Adsorbates from Core-Level Shake-up Spectra: N2/Ni(100)," Physical Review Letters **67** (8), 1015-1018 (1991).

[15] Anders Nilsson, "Core Level Electron Spectroscopy Studies of Surfaces and Adsorbates," Ph. D. Thesis, Uppsala University, 1989.

[16] J. Schirmer, G. Angonoa, S. Svensson, D. Nordfors, and U. Gelius, "High-energy Photoelectron C 1s and O 1s shake-up spectra of CO," Journal of Physics B: Atomic and Molecular Physics **20**, 6031-6040 (1987).

[17] J. C. Fuggle, E. Umbach, D. Menzel, K. Wnadelt, and C. R. Brundle, "Adsorbate Line Shpaes and Multiple Lines in XPS: Comparison of Theory and Experiment," Solid State Communications **27**, 63-69 (1978).

[18] J. J. Barton, S. W. Robey, C. C. Bahr, and D. A. Shirley, "The Structure of Surfaces," in *Springer Series in Surface Sciences*, edited by M. A. Van Hove and S. Y. Tong (Springer Verlag, New York, 1985), Vol. 2.

[19] J. Stohr and R. Jaeger, "Absorption-edge resonances, core-hole screening, and orientation of chemisorbed molecules: CO, NO, and N2 on Ni(100)," Physical Review B **26** (8), 4111-4129 (1982).

[20] to be published.

[21] R. Raval, S. F. Parker, M. E. Pemble, P. Hollins, J. Pritchard, and M. A. Chesters, "FT-RAIRS, EELS and LEED Studies of the Adsorption of Carbon Monoxide on Cu(111)," Surface Science **203**, 353-377 (1988).

[22] Z. Huang, "Structural Studies of Molecular Metallic Overlayers Using Angle-Resolved Photoemission Extended Fine Structure," Ph. D. Thesis, University of California, Berkeley, 1992.

[23] S. Doniach and M. Sunjic, "Many-electron singularity in X-ray photoemission and X-ray line spectra from metals," Journal of Physics C: Solid State Physics **3**, 285-291 (1970).

[24] W. R. A. Huff, Y. Zheng, Z. Hussain, and D. A. Shirley, "Final-State Effects in the Angle-Resolved Photoemission Extended Fine Structure of c(2x2)S/Ni(001)," Journal of Physical Chemistry **98**, 9182-9186 (1994).

[25] S. M. Goldberg, C. S. Fadley, and S. Kono, "Photoionization Cross-section for Atomic Orbitals with Random and Fixed Spatial Orientation," Journal of Electron Spectroscopy and Related Phenomena **21**, 1981 (1981).

(A) (√3 x √3)R30° CO/Cu(111)

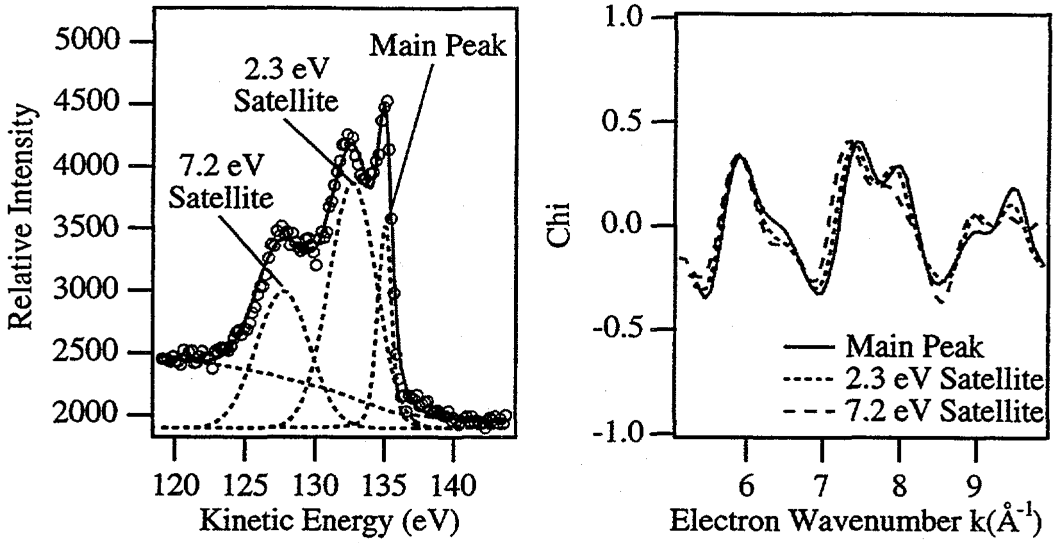

(B) p2mg(2x1) CO/Ni(110)

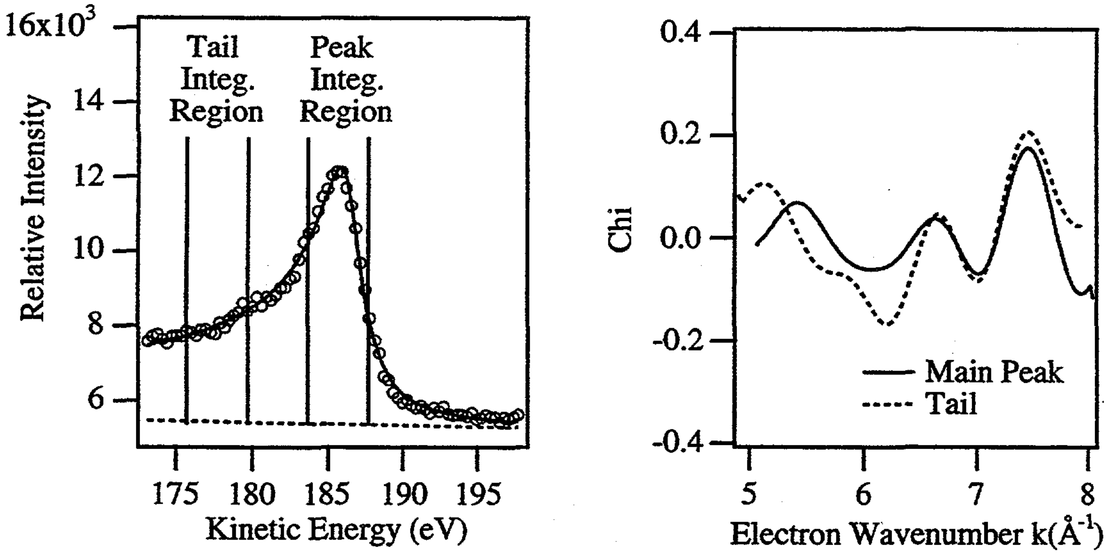

Figure 1.
XPS spectra and ARPEFS chi currves for A) (√3 x √3)R30° CO/Cu(111) and B) p2mg(2 x1) CO/Ni(110), of the C 1s core-level. The circles in the XPS spectra (left) represent experimental data and the solid line is the best fit using the components shown in dashes. The peaks in (A) are fit with Voigt functions to extract their intensity. The best fit Doniac-Sunjic curve is the solid line in (B). The intensity for two regions, indicated by vertical solid lines, was determined by numerical integration in (B). The ARPEFS curve for each peak/region is shown to the right. Each curve is scaled horizontally to the k-value of its corresponding peak in (A) and to the center of the corresponding region in (B).

(A) c(2x2) N_2/Ni(100)

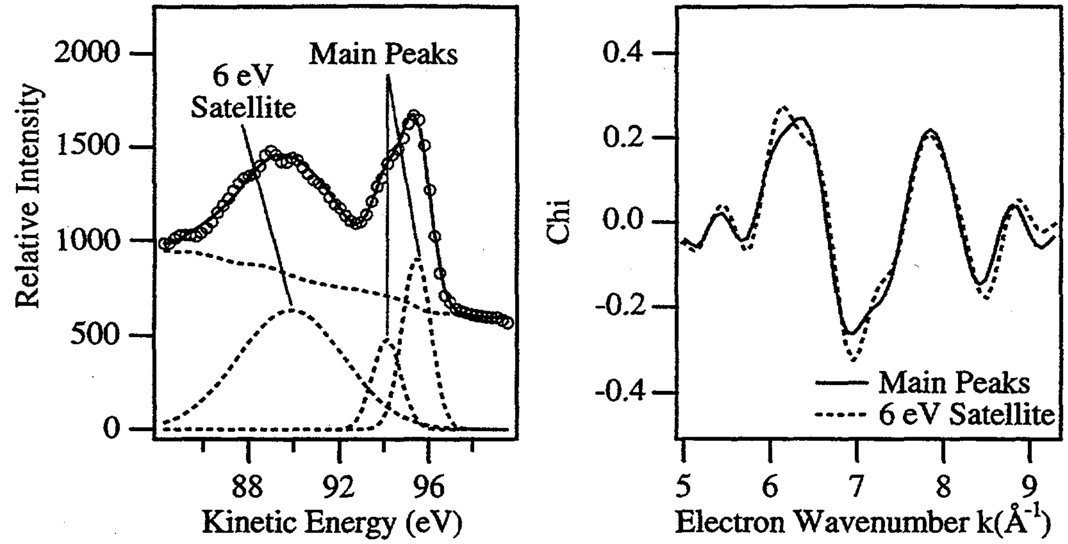

(B) clean Ni(111)

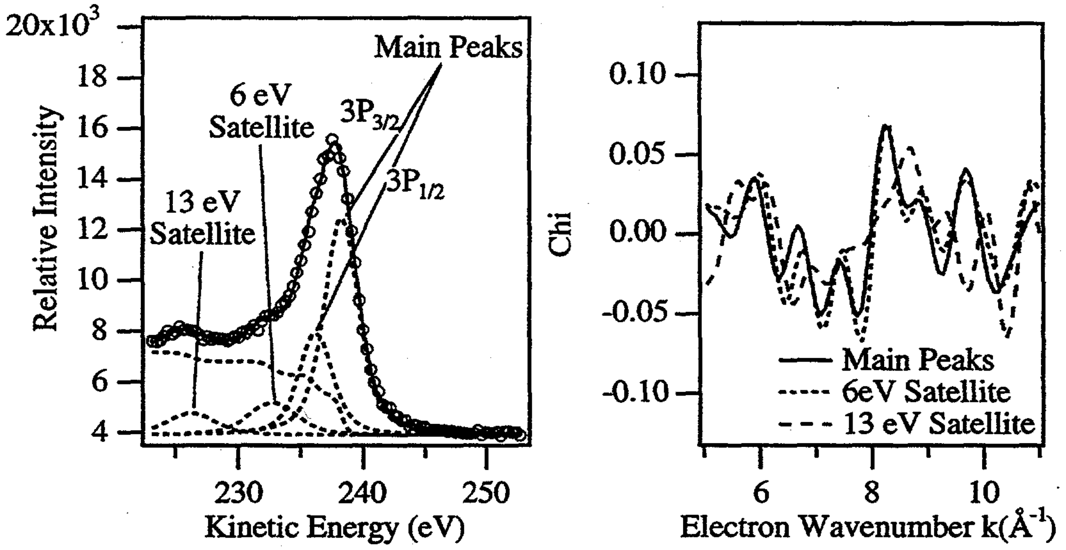

Figure 2.

XPS and ARPEFS curves of A) c(2 x 2)N_2/Ni(100) of the N 1s core-level, and B) clean Ni(111) of the Ni 3p core-level. The circles in the XPS spectra (left) represent data and the solid curve is the best fit using the components indicated in dashes. The ARPEFS curves (right) are extracted from the peak intensities and are scaled to the wave-number of the corresponding peak. The two main peaks in (A) area summed and the k-value used for scaling the ARPEFS curve is the average of the two. The Ni 3p-1/2 and 3p-3/2 peaks are similarly summed to find their total intensity.

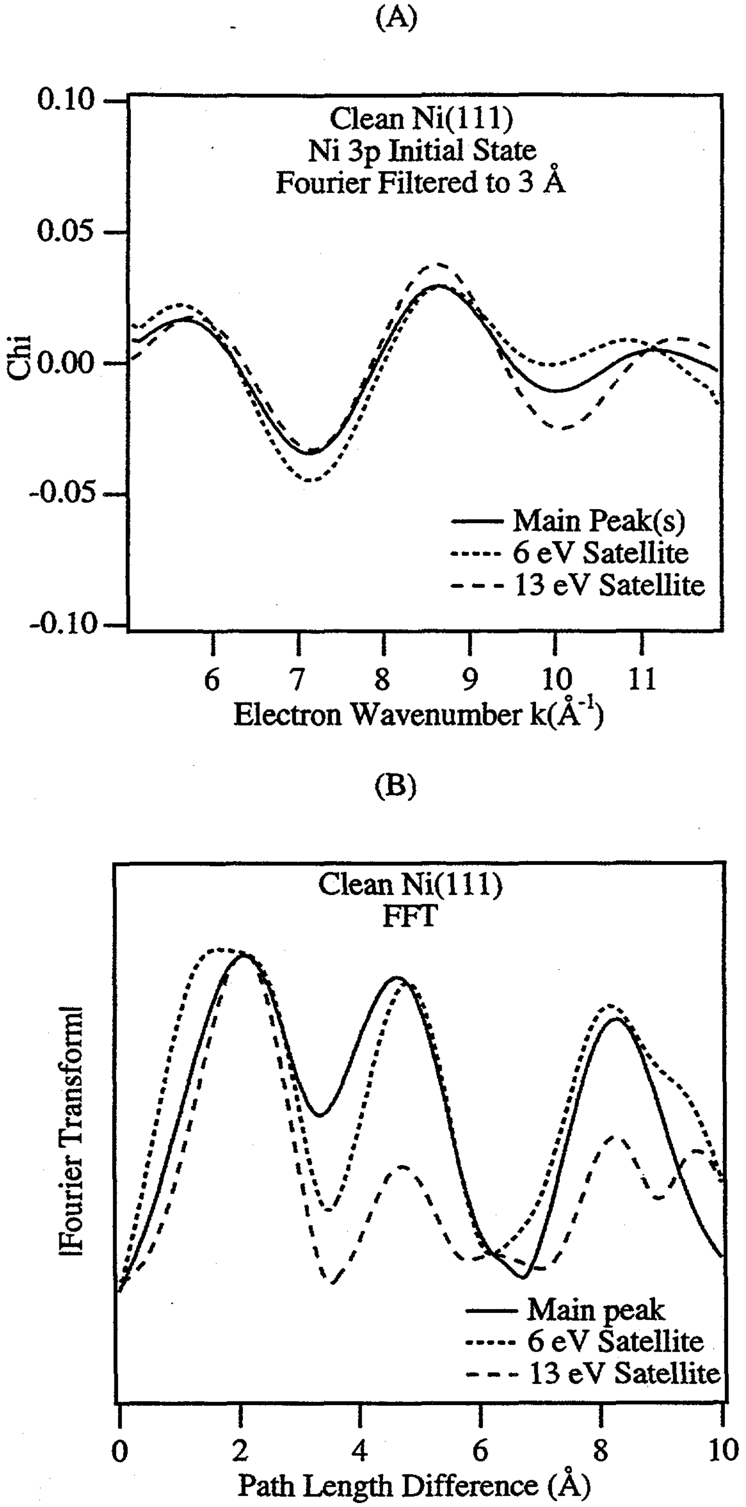

Figure 3.
ARPEFS curve (A) and Fourier Transform (B) of the Nickel XPS peak intensities. The ARPEFS curve has been Fourier filtered with a 3 Å cutoff to examine the phase of the dominant peak. The 13 eV satellite curves has been scaled by x5 .

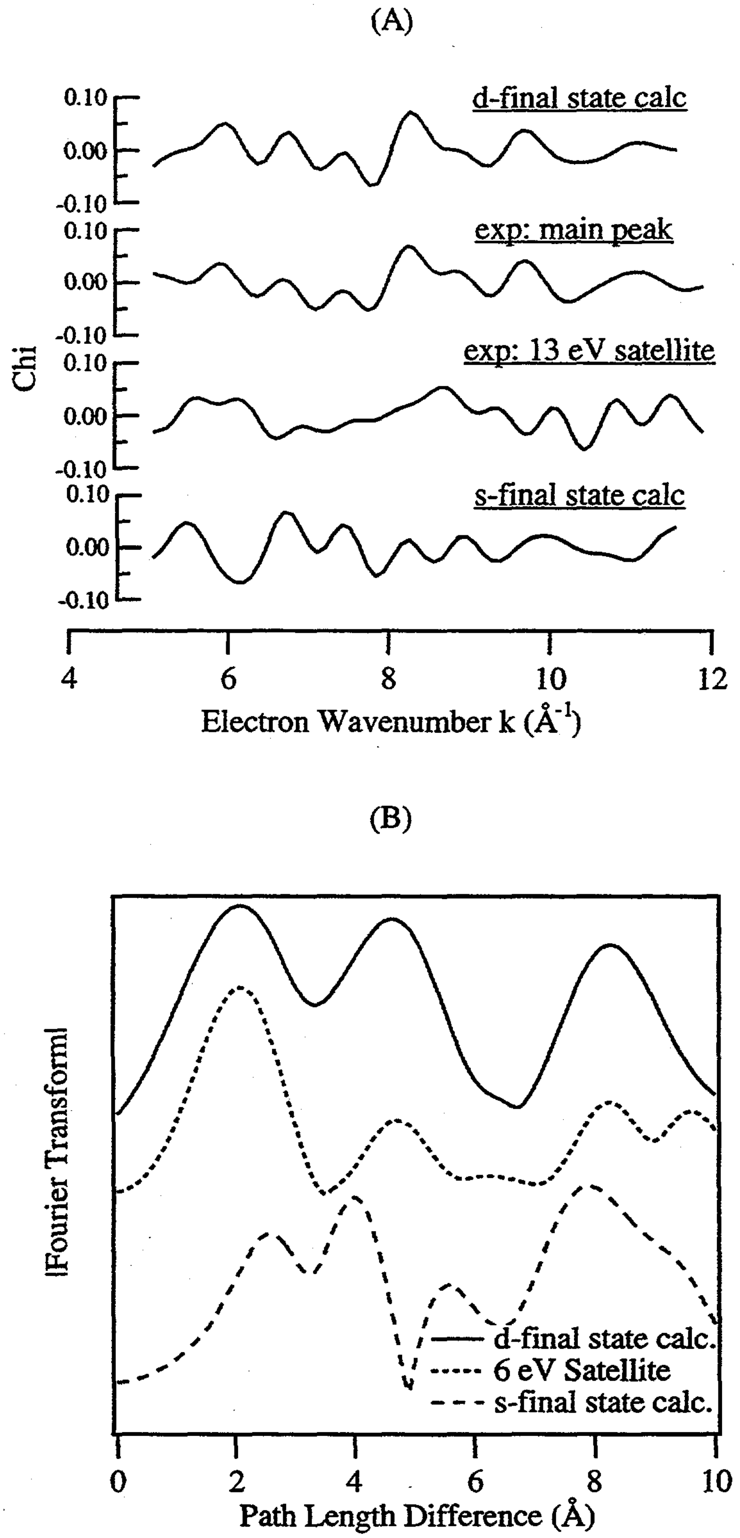

Figure 4.
Comparison of the 13 eV satellite ARPEFS curve (top) and Fourier transform (bottom) with d-like and s-like final-state multiple-scattering calculations.

Design and Characterization of a High Resolution, Fourier-Transform Soft X-ray Spectrometer for Synchrotron Radiation

Introduction

A Fourier Transform Soft X-ray spectrometer (FT-SX) has been designed and is under construction for the Advanced Light Source (ALS) at Lawrence Berkeley National Laboratory. The spectrometer is designed for ultra-high resolution (theoretical resolving power $E/\Delta E \sim 10^6$) in the photon energy region of 60-120 eV. This instrument is expected to provide experimental results which sensitively test models of correlated electron processes in atomic and molecular physics. The design criteria and consequent technical challenges posed by the short wavelengths of x-rays and desired resolving power are discussed. The fundamental and practical aspects of soft x-ray interferometry are also explored.

Background

Helium Double Excitations, Electron Correlation, and Chemistry

Correlated electron motion is at the center of any chemical process and thus constitutes a very important arena of basic scientific research. The many-body nature of the problem precludes analytical solutions, leaving only approximations to the quantum problem potentially tractable. The central problem in theoretical electron correlation studies is to find the appropriate approximations that describe all of the main characteristics of the experimentally observed features of such systems. It is natural to start with excitations of the helium atom since this is the simplest correlated electron system and, with the availability of synchrotron radiation sources, increasingly detailed experimental observations have become available. The FT-SX spectrometer has been designed to probe this prototypical system with unprecedented resolving power. Of particular interest are the regions of overlapping double excitation series where classically chaotic behavior is mixed with quantization effects[1-4].

Synchrotron Radiation, Soft X-ray Monochromators, and Resolution Limits

Synchrotron radiation has proved to be an extremely useful tools in basic atomic and molecular physics studies. The high photon flux and tunable photon energy facilitate detailed studies of excitation processes. Third generation light sources, such as the Advanced Light Source at Lawrence Berkeley National Laboratory, coupled with high resolution beam lines are providing extremely detailed observations of scientifically important systems such as the helium double excitation series, a correlated electron system, in the soft x-ray range. However, the theoretical limits of current x-ray monochromators have been reached [5] and there is more to be gained by increased resolving power in x-ray absorption experiments.

The highest resolving power soft x-ray beam lines available consist of a low emittance synchrotron source and a highly optimized, grating-based monochromator, usually a Spherical Grating Monochromator (SGM). The low emittance source allows for relatively high photon flux while using the small apertures necessary to operate the SGM at maximum resolving power. While the claim of experimentally achieved resolving power can vary depending on the interpretation of the data and caution of the investigators, it is apparent that the theoretically maximum resolving power of a spherical grating monochromator[5], (~64,000) has been closely approached by Kaindl, et al. in the region of the helium double excitations (~ 65 eV).

Soft X-ray Interferometry for High Resolution

To achieve a still higher resolving power, a different approach must be used other than the traditional, grating-based monochromator. It has been known in optics for a long time that interferometers can always, in principle, outperform gratings in terms of maximum resolving power or phase-space acceptance for equivalent resolving power. In practice, interferometry with x-rays is very difficult, due to the short wavelengths. Only recently have the mechanical, optical, and metrological technology advanced enough to practically build a soft x-ray interferometer for Fourier transform spectrometry.

Overview of the FT-SX Branch Line of Beam line 9.3.2

The FT-SX spectrometer is a modified Mach-Zehnder type interferometer designed to operate in the 60-120 eV photon energy range (wavelength 10-20 nm) with a theoretical resolution of ~65 μeV. It is a permanent end-station branch of beam line 9.3.2 at the ALS. The x-ray beam is first pre-filtered to a band-width of ~100 meV by the SGM monochromator. They are then deflected by a simple plane mirror downstream of the monochromator exit slit. They then pass through a conventional gas-ionization cell, the FT-SX spectrometer and impinge on a solid state detector. The entire interferometer is mounted in a high-vacuum chamber separated from the UHV beam line by a thin foil window. The vacuum vessel is mounted on an optical table with provisions to damp vibration both vertically and horizontally. The moving-mirror stage is driven by a specially designed, double-action, hydraulic piston which is external to the vacuum vessel. The mirror position in the interferometer is measured with a commercially available Hewlett-Packard heterodyne laser interferometer with a resolution of 3 Å and an actual rms noise of 4.5 Å at a sampling rate > 1MHz. Both the piston drive and the laser interferometer are mounted on the optical table. The heart of the spectrometer is a flexure-hinged linear motion stage upon which are mounted four mirrors permanently aligned by optical contacting to a custom, high precision prism.

The characteristics of the photon beam entering the FT-SX are determined by the beam line 9.3.2 SGM monochromator operated in a moderate resolution mode with a 100 l/mm grating to improve the signal/noise ratio of the absorption spectrum measured by the interferometer. The exit slit size of 100 μm gives a 0.15% band pass at 65 eV. The beam has a vertical divergence angle of 1.2 mrad. The first beam splitter is approximately 2.9 meters away from the exit slit. This results in a vertical beam size of 3.6 mm at the first beam splitter. The horizontal divergence is 2.5 mrad. The beam size is 750 μm at the horizontal focus, 5.7 meters from the first beam splitter. The horizontal beam size is thus 15 mm wide at the first beam splitter, assuming no intervening apertures.

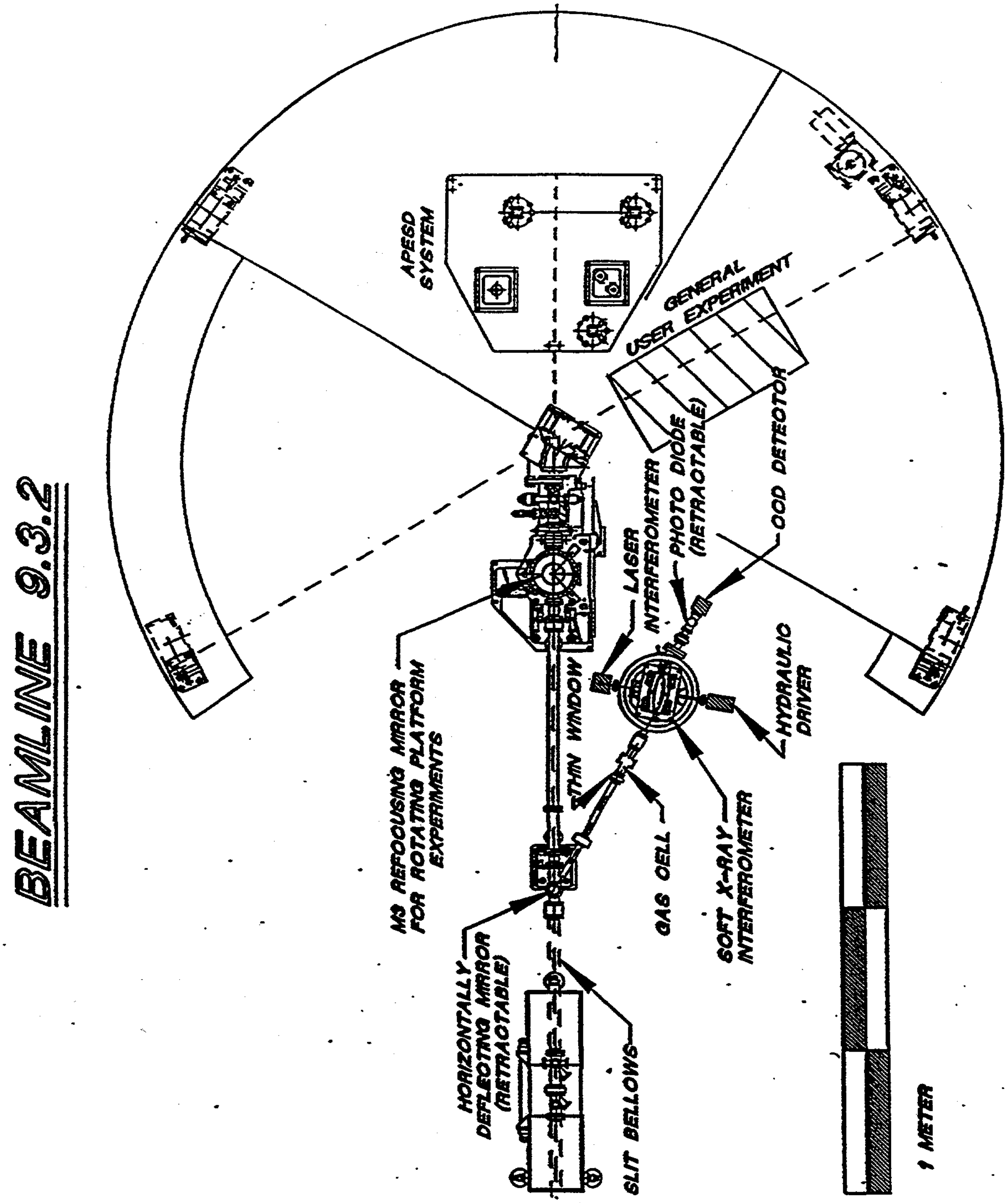

Schematic of Beam Line 9.3.2 End Stations

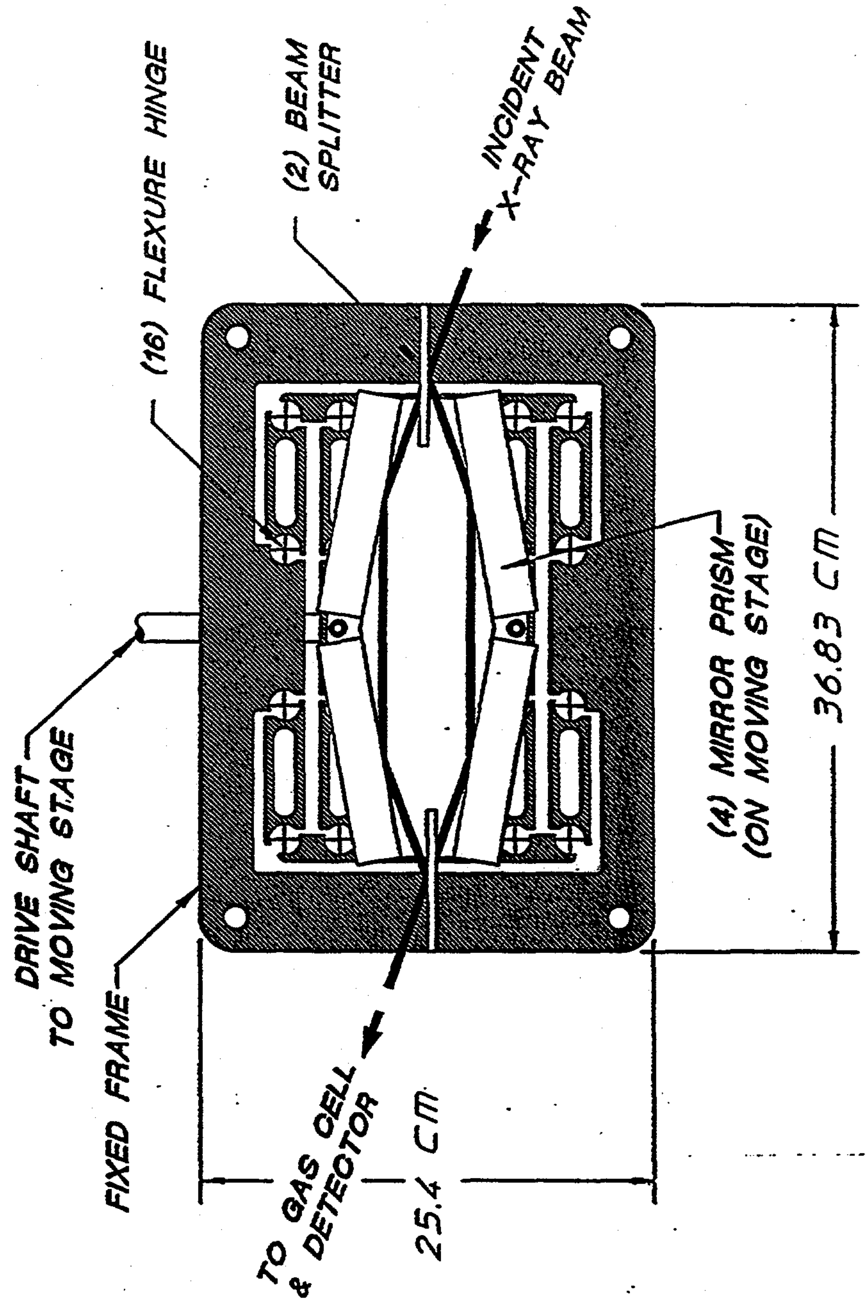

Schematic of the FT-SX interferometer

Essentials of Fourier Transform Spectrometry

The basic operation of a Fourier transform spectrometer is to split an incident beam into two coherent parts and recombine them after introducing a phase delay. The Fourier transform of the resulting interference pattern, as a function of phase delay or path-length difference, gives the energy spectrum of the incident beam. Note that an absorbing sample may be placed either before or after the interferometer. The Michelson interferometer, which is widely used in infra-red spectroscopy, is the most common example of such an instrument. The path-length-difference is introduced by moving one or more mirrors to vary the geometric distance between the beam splitter(s) and the detector. The key components of any interferometer are the beam splitters, which usually determine the optical aperture and operating range of an interferometer, and the mirror translation stage, which determine the maximum resolution of the instrument.

The spectral resolution of any optical spectrometer depends on the maximum path length difference introduced between the various parts of the beam. More precisely

$$\delta v = \frac{1}{2\Delta L}$$

where ΔL is the maximum path-length-difference introduced, in centimeters, and δv is the maximum resolution in wave numbers. If one can maintain the alignment of the mirrors to ensure proper overlap of the beams at the detector, the resolution of an interferometer can be made arbitrarily small by simply increasing ΔL. A grating, on the other hand, has a limit to the maximum path-length-difference which it can accommodate. The requirement that a grating must be completely coherently illuminated for maximum resolving power limits the throughput relative to an interferometer, which only requires that the beams be recombined coherently.

Design Constraints and Characterization of Soft X-ray Fourier Transform Spectrometers

The design constraints of FT-SX spectrometers are driven by two factors: the desired resolving power and the x-ray wavelengths of the desired operating range. The instrument under construction at the Advanced Light Source is designed to achieve a resolving power of $\sim 10^6$ at 65 eV.

Nominal Incidence Angle and Maximum Path Length Difference

The index of refraction for x-rays is ~ 10^{-6} away from unity[6]. This requires that most reflecting x-ray optical elements are mirrors used at grazing incidence. The geometry and size of the instrument is then constrained by the reflectivity of the mirrors and beam splitters, the desired resolving power (via the total motion of the mirrors), and beam spot size.

The principal design trade-off is between reflectivity, which decreases with increasing incidence angle, and instrument size, which must increase with decreasing incidence angle. There is more difficulty in increasing the instrument size than just aesthetics and convenience of operation. The mechanical tolerances, discussed below, set practical limits to the size of the instrument, due to the extremely tight specifications driven by the short wavelengths of the x-rays. Also, large x-ray mirrors and beam splitters are technically challenging to fabricate and are consequently very expensive.

Reflectivity and Incidence Angles for the FT-SX

The FT-SX is designed with an incidence angle of 20° on the beam splitters and 10° on each mirror. These angles,with a molybdenum optical coating, provide good reflectivity.

Each branch of the beam reflects once from the deflecting mirror (15°) and beam splitter (20°) and twice from the prism mirrors (10°). Multiplying the reflectivities gives the total transmission function of the interferometer. The total photon flux expected to traverse the system is then the product of the transmission function with the photon flux exiting the monochromator.

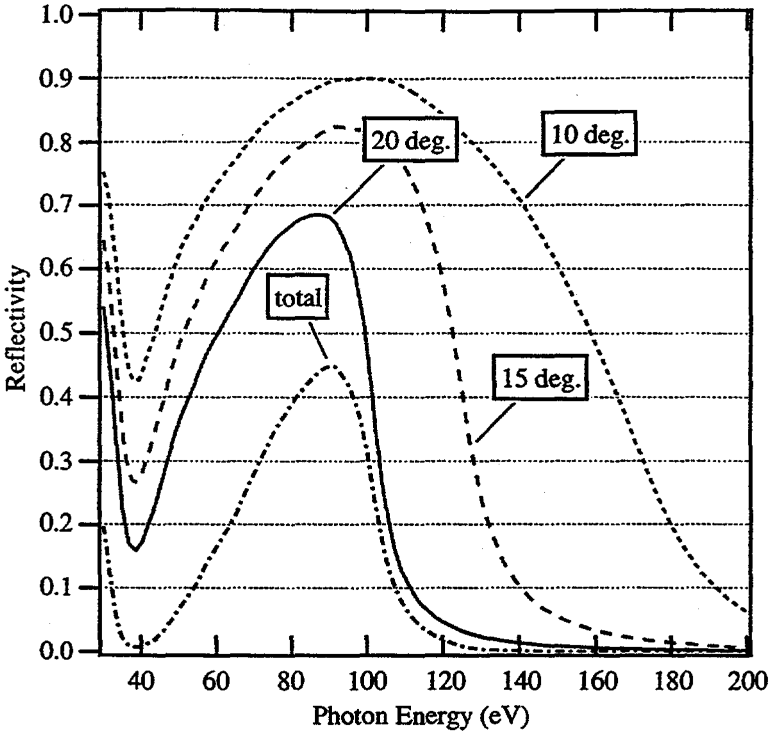

Reflectivity of Molybdenum at Various Incidence Angles

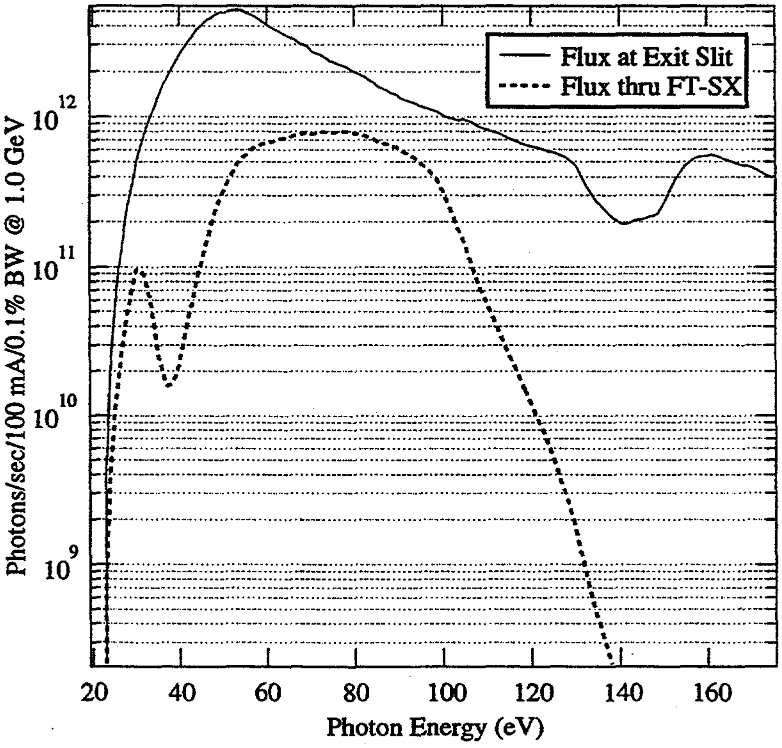

Measured Photon Flux through ALS Beam Line 9.3.2 and Expected Flux Through FT-SX

The photon flux was measured with a clean gold photodiode downstream from the exit slit of the monochromator, with a 0.1% band pass. The flux is quite high from 30 eV to 120 eV. Note that the graph above does not account for any apertures downstream of the exit slit. Some additional loss of beam may occur, but the instrument will be operated with a slightly larger band pass and higher ring current, so these factors will approximately cancel.

Path Length Difference and Total Mirror Travel

The geometry of the instrument, established by the selection of incidence angles on the beam splitters and mirrors, determines the ratio of path-length-difference(PLD) to mirror-motion. The total path-length difference is determined by the desired resolving power . The total mirror motion is then fixed from these two requirements. For the FT-SX the incidence angle on the beam splitters is 20°, so the ratio of PLD/ mirror-stage movement is $x = 2.6$.

Using the relationship for resolving power

$$R = \frac{E}{\delta E}$$

and the Fourier spectroscopy resolution equation for photons

$$\delta E = \frac{1.24 \mu m \cdot eV}{2x\Delta s}$$

where Δs is the total mirror travel in μm, we solve for Δs to get

$$\Delta s = \frac{R \cdot 1.24}{2Ex} .$$

The design goal of 10^6 resolving power at 65 eV for the FT-SX leads to a stage travel of 3.7 mm. Note that this is the displacement from the center since we intend to take two sided interferograms, so the total stage travel is 7 mm. We have achieved a stage travel of 14 mm with all of the required tolerances, as discussed below.

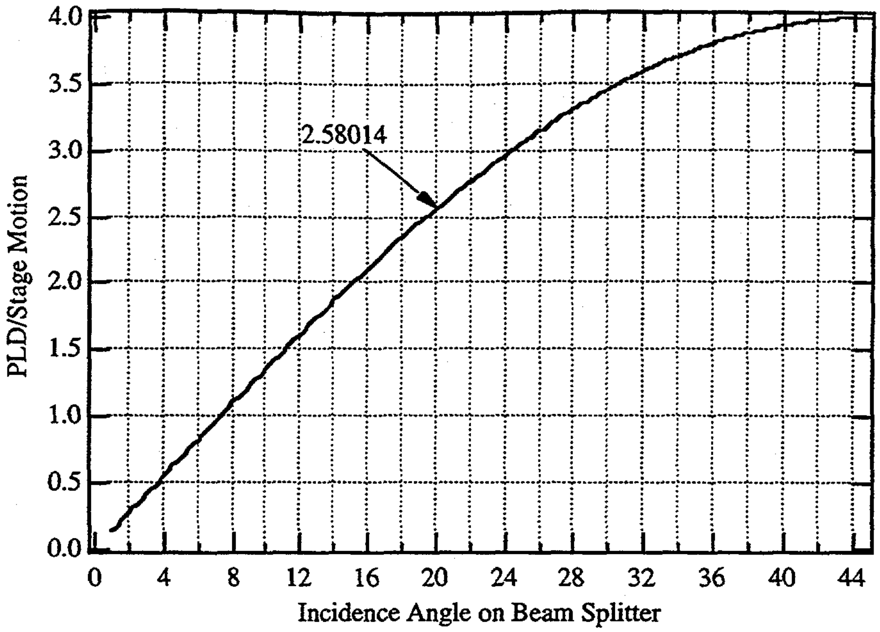

Ratio of path-length-difference to mirror stage motion vs. incidence angle on the beam splitters.
Note that below 10 degrees incidence the ratio is approximately 0.1375*degrees.

Mirror, Beam Splitter, and Beam Sizes

The projected beam size on the beam splitters and mirrors increases with decreasing incidence angle. The beam splitters are the field limiting optic, just as in infra-red and visible interferometry. The mirrors must be large enough to accept the entire beam anywhere in its full range of motion. The horizontal beam-splitter size is $w = 16$ mm and the incidence angle is $\theta = 0.349$ radians. The projected beam-splitter aperture is just

$$p = w \times \sin(\theta_i) \approx w \times \theta$$

giving an acceptance of 5.6 mm of the horizontal beam. All of the beam is accepted vertically with a beam-splitter aperture of 6 mm.

The projected mirror size along the direction of motion must be at least as large as the sum of the projected beam width and the total motion of the mirror. For a total stage motion of 14 mm the mirror must then be at least 86 mm long in the horizontal. The vertical size of the beam traversing the system is 3.6 mm and each optical element must be at least that tall. The actual size of the mirrors are 127 mm long and 32 mm high. The mirrors are much larger in the vertical because the polishing base must be large enough for the manufacturer to polish the mirror to x-ray quality.

Off Axis Rays and Resolving Power

The path length difference between rays off the principle axis of the interferometer will be different than those on axis. Consequently, the resolving power is diminished with increasing angular divergence of the x-rays accepted through the system. This can be demonstrated in a simple way. Looking back through the instrument from an image plane I, two images of the source can be seen.

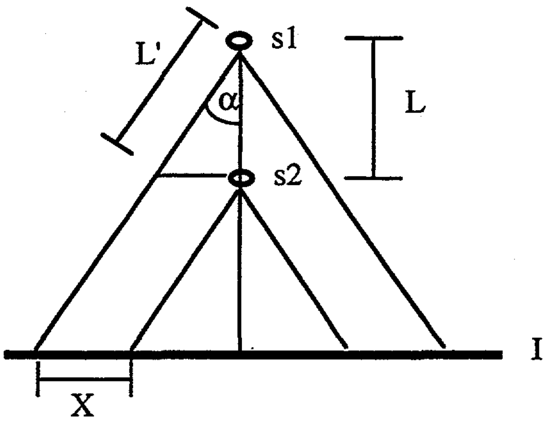

Path Length Difference Between Off-Axis Rays and the Central Ray

On axis, they appear to be separated by the path length difference introduced by displacement of the mirror stage

$$L = sx$$

where x is the mirror stage displacement and s is the geometric factor relating stage displacement and on-axis path length difference. Note that s=2 for the traditional Michelson interferometer with the mirrors at right angles and one mirror moving. Now, off axis the path length difference is given by

$$L = L' \cos(\alpha)$$

To relate this angular acceptance to the resolving power, we begin by noting that on axis the nth fringe of some wavelength of light is constructively interfering

$$n\lambda = L.$$

Off axis some nearby wavelength is doing the same

$$n\lambda' = L'$$

By substitution and making use of the small angle approximation

$$n\lambda = n\lambda' \cos(\alpha) \approx n\lambda' \left(1 - \frac{\alpha^2}{2}\right).$$

We then relate the resolving power to α

$$R = \frac{\lambda}{\delta\lambda} = \frac{2}{\alpha^2},$$

where

$$\delta\lambda = \lambda - \lambda'.$$

Hence the resolving power goes inversely with the square of the acceptance angle of the optical system. A more detailed treatment, derived by integrating the intensity response over acceptance angle, is given by Brault [7]. If the on-axis intensity to monochromatic light is

$$dI = d\Omega \cos\left(\frac{2\pi}{\lambda} L \cos(\alpha)\right)$$

then integration and use of the small angle approximation gives

$$I = \Omega_m \mathrm{sinc}\left(\frac{L\Omega_m}{2\pi\lambda}\right) \cos\left(\frac{2\pi L}{\lambda}\left(1 - \frac{\Omega_m}{4\pi}\right)\right)$$

where

$$\Omega_m = \pi\alpha^2.$$

This results in a convolution of the energy spectrum (fourier transform of the above function) with a rectangle. To match this convoluting function with the desired resolving power, we find

$$R = \frac{2\pi}{\Omega_m} = \frac{2}{\alpha^2}$$

This condition corresponds to accepting only one half of a fringe across the detector at the highest wave number at the maximum path-length difference. The other effects we may notice is that there is a scale change related to the solid angle acceptance.

For the FT-SX interferometer a resolving power of 10^6 gives an off-axis half-angle of 1.4 milliradians. The divergence half-angle of the x-ray beam coming from the monochromator is 0.6 mrad vertically and 1.2 horizontally, which is well within the necessary tolerance.

Optical Surface and Alignment Tolerances

The wave fronts of the two recombined beams must maintain tight phase relationships in order to produce fringes with good contrast. We consider here the errors and tolerances required of the surface figure and alignment of the optics.

Theoretical Background

Following Chamberlain[8] and Howells[9] the effect of wave front errors may be written as an integral over the area of the detector

$$D(\sigma)=\frac{1}{A}\iint_A \cos[2\pi\sigma\delta(u,v)]dudv$$

where $\delta(u,v)$ is the wave front error at point u,v on the detector. The total intensity on the detector is then written as

$$I(x)=\frac{I_0}{2}+\int_0^\infty D(\sigma)B(\sigma)\cos(2\pi\sigma x)d\sigma ,$$

and $B(\sigma)$ is the energy spectrum we wish to recover. Chamberlain calls $D(\sigma)$ the spectral distortion factor. We would like to set this distortion factor to >0.9 to maintain good fringe contrast and hence signal-to-noise ratio.

Optical Surface Figure

For a spherical wave front with radius R the wave front error in polar coordinates (r,ϕ) is

$$\delta(r)=\frac{r^2}{2R_s}.$$

Integrating over the area of the detector, Howells arrives at

$$D(\sigma)=\frac{1}{A}\int_0^{2\pi}d\varphi\int_0^R\cos\left(2\pi\sigma\frac{r^2}{2R_s}\right)rdr=\mathrm{sinc}\left(\frac{\sigma R^2}{R_s}\right).$$

Our criterion is then satisfied for $R_s>4\sigma R^2$. For $\sigma=10^6/cm$ (10 nm wavelength) and an effective detector radius $R\approx0.3$ cm gives an allowable wave front sphericity with radius greater than 400 m. The optical surfaces must be flat enough to maintain the above requirement. For a grazing incidence beam on a spherical mirror of radius ρ the focal length is given by

$$R_s = \frac{\rho \sin\theta}{2} .$$

The incidence angle of 10° on the mirrors require $\rho > 18$ km and for the beam splitters $\rho > 9$ km. For a mirror of half width of 50 mm the maximum slope error is then 10 µrad. For the beam splitter with half width 6 mm the slope error is maximally 2.5 µrad. A surface roughness of 5 Å rms is acceptable for these optics.

The beam splitters were fabricated by Rockwell International, RocketDyne. A slope error of 0.5 µrad and an rms roughness < 5 Å was achieved. All of the mirrors, fabricated by Photon Sciences International, have been fabricated with a surface roughness < 2 Å rms and a slope error < 0.5 µrad rms.

Optical Alignment

The relative tilts of the wave fronts must be maintained in the alignment of the optical surfaces. If the wave front tilt is e then the error is $\delta(\sigma) = \upsilon e$ and the distortion factor becomes

$$\begin{aligned} D(\sigma) &= \frac{1}{A}\int_{-R}^{R} d\upsilon \int_{-\sqrt{R^2-\upsilon^2}}^{\sqrt{R^2-\upsilon^2}} \cos(2\pi\sigma\upsilon e)\,d\mu \\ &= \frac{2R}{A}\int_{-R}^{R}\sqrt{1-\left(\frac{\upsilon}{R}\right)^2}\cos(2\pi\sigma\upsilon e)\,d\upsilon \\ &= 2\frac{J_1(2\pi\sigma eR)}{2\pi\sigma eR} . \end{aligned}$$

For D=0.9 the allowable wave front error is then,

$$e < \frac{0.911}{2\pi\sigma R} = 1.5\ \mu\text{rad} .$$

The downstream beam splitter is held in an adjustable mount to achieve this tolerance. This requires the mirrors and first beam splitter to be very close to the optimum. Because the beam-splitters are adjustable while the mirrors are pre-aligned, we specify the mirrors to be aligned within 0.5 µrad and the beam splitters to be within 1.0 µrad.

The prism base was fabricated by Photon Sciences International. Because optical contacting, the method for fixing the mirrors to the prism base, does not lead to any misalignment, a measurement of the edges of the prism determines the alignment of the mirrors. The prism was measured by Photon Sciences using Hadinger fringes to be aligned with error < 0.6 μrad to a common, perpendicular plane.

Translation Stage Tilt Errors

The relationship between the rotation of the moving mirrors and the error in the wave front is derived by Howells[9] for a single, plane mirror to be

$$\frac{\Delta r}{\Delta w} < 2\cos(\theta)\sin(\theta)$$

where Δr is the wave front tilt, Δw is the rotation of the mirror, and theta is the incidence angle.

For the pitch error of the moving stage the error occurs twice for each beam and in opposite directions, yielding

$$\Delta p < \frac{1.5\ \mu\text{rad}}{8\cos\theta\sin\theta} = 2.1\ \mu\text{rad}$$

The effect of the roll of the stage is negligible since the rotation is in the plane of the mirror surfaces. The yaw of the moving stage is also negligible since each branch of the beam reflects from two mirrors in the manner of a pentaprism.

The manufacture of the stage introduced errors into the alignment of the cartwheel flexures. This resulted in the stage having an unacceptable tilt error. This problem was rectified by adding slots to the frame near the flexture hinges that allow a correction of the stage tilt. Two ground, tapered rods were used to correct the tilt. The final stage tilt error was measured to be <0.5 μrad, at the resolution limit of the autocollimator.

Beam Splitters

Introduction

Two kinds of beam splitters are possible: wave-front dividing and amplitude dividing. There are strengths and weaknesses of each. Soft x-ray beam splitters are a subject of research in their own right. There are none commercially available. Important considerations for each are discussed below. The low divergence of the synchrotron radiation beam makes wave front dividing beam-splitters the best choice for a spectrometer using this source. Essentially all of the beam may be admitted through the system and the coherency conditions are satisfactorily met. Working with Rockwell International, Rocket Dyne Division we have developed a wave-front dividing beam splitter with excellent efficiency.

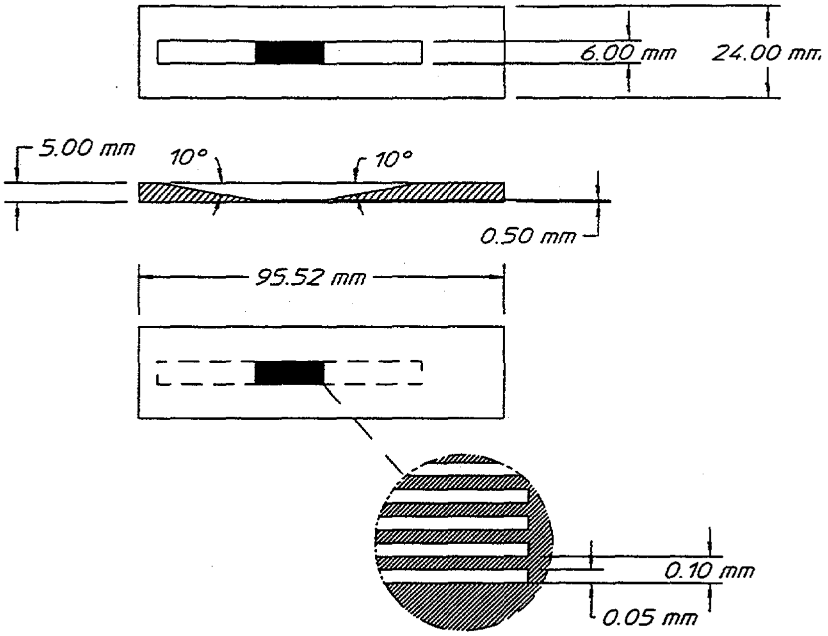

FT-SX Beam-Splitter Schematic

Wave Front Dividing Beam Splitters

Efficiency

The efficiency of the wave-front dividing beam splitter is determined by the incidence angle and the optical coating, which was discussed above.

Coherence Requirements on Angular Acceptance

The visibility of the interferogram fringes is affected by the average coherence properties of the light waves across the beam-splitter. A simple understanding of the problem can be gained by considering the coherence of two points on an image plane (the beam splitter), separated by distance x, for a source of width s consisting of independent, isotropic radiators.

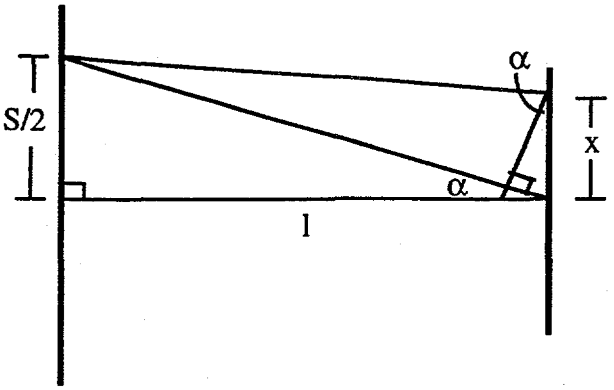

Coherence With an Extended Source (see text)

In order for the two points separated by x to be considered coherently illuminated, we require the path length difference between the two rays coming from a point on the source be equal to or less than one quarter of the x-ray wavelength. The worst case, corresponding to the minimum wavelength and a point on the extreme edge of the source, is given by

$$x\sin(\alpha) = \lambda/4.$$

A slot and the adjacent reflecting bar on the beam splitter should be coherently illuminated. Making use of the small angle approximation $\sin(\alpha)\approx\alpha$ and calling the grating period w=2x we get

$$\alpha \le \frac{\lambda_{\max}}{2w}$$

and thus we get the requirement on the angular acceptance of the optical system that the incidence angles be less than half of the 1st order diffraction angle. Note that this is the acceptance angle in the plane perpendicular to the slot directions. The angle in the plane parallel to the slots is not limited by this requirement. However, one must keep in mind that the coherence width of the beam affects the accuracy with which the beams must be recombined at the detector.

For the FT-SX beam-splitters, the period w is 100 μm and the maximum wavelength is 10 nm. This sets the angle subtended by the source to be 100 μrad. The monochromator exit slit will be nominally 100 μm and l=5.7 meters from the first beam splitter, giving an actual subtended angle of 100/5.7=17.5 μrad.

Another way of understanding the coherent illumination of the beam splitter is to consider diffraction from the monochromator exit slit. The first diffraction minimum comes at $\theta = \lambda/2s$, which we may consider to be the coherence half-angle. The coherence width at the beam splitter is then $2\theta l = \lambda l/s$ and the number of periods coherently illuminated is $N = \lambda l/sw$. For the FT-SX beam splitter and 100 μm slit $N = 5$.

Diffraction Effects

A wave front dividing beam splitter inevitably also acts as a grating. While it is desirable to reduce the slot spacing to increase the allowable source size, the diffraction angles increase. The beam splitters thus must be designed so that there is no significant intensity in any diffracted orders of higher angle than allowed from the resolving power limitations stated above. Since there is a (small) range of angles incident on the beam splitter, the incident beam divergence is convolved with the diffraction pattern. This increases the effective angle range traversing the spectrometer.

To analyze the effects of the beam splitter, we use the normalized grating equation for a slotted transmission grating[10]

$$I(\theta) = \left(\frac{\sin(\beta)}{\beta}\right)^2 \left(\frac{\sin(N\alpha)}{\sin(\alpha)}\right)^2$$

where $\alpha = \frac{\pi a \sin(\theta)}{\lambda}$, a is the grating period, $\beta = \frac{\pi b \sin(\theta)}{\lambda}$, b is the slot width, and N is the number of grating periods which are coherently illuminated. The intensity maxima come when $a\sin(\theta) = m\lambda$. A beam splitter will have b=a/2, i.e. the slots will be half the period of the "grating". In this situation, the even orders are suppressed. Both the reflected and the transmitted beams will exhibit this pattern. This function is then convolved with the divergence of the original light to get the divergence of the beam through the interferometer.

For the FT-SX we calculated above that 5 periods are illuminated. The graph below shows the diffraction pattern for the first beam splitter and the integrated intensity with increasing angle.

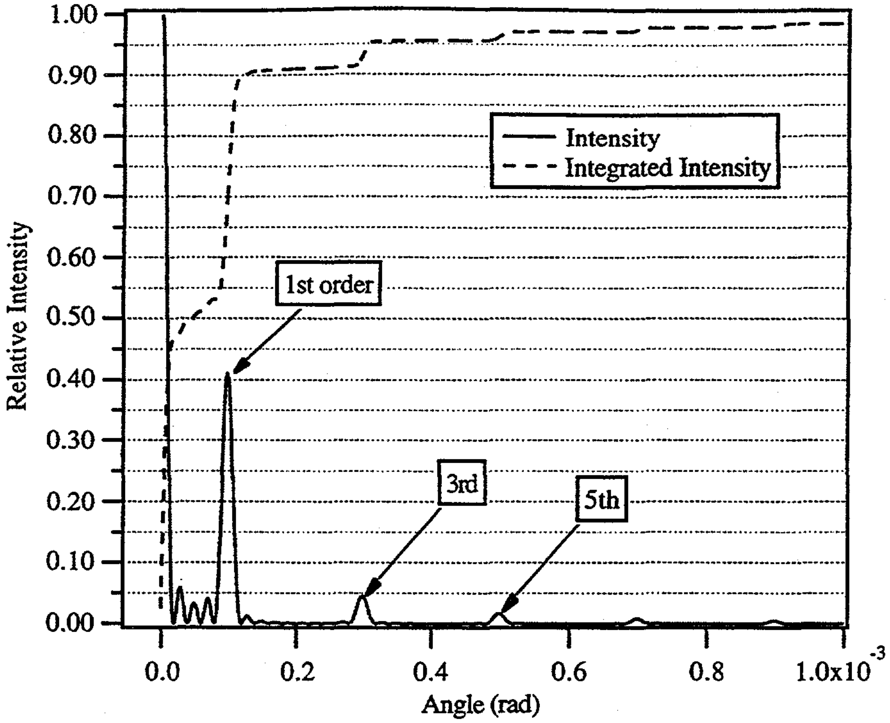

Diffraction From the FT-SX Beam Splitter

Note that 95% of the total intensity is within 0.3 milliradians. Since the vertical divergence of the beam is about 0.6 milliradians, almost all the beam traversing past the first beam splitter will be well within the 1.4 milliradian specification derived above.

Collimation

The slotted beam splitters act as collimators, limiting the acceptance angle because of their finite thickness. The 0.5 mm thick beam splitters have a projected thickness of ~1.5 mm for an incidence angle of 20 degrees. The 50 μm high slots in the beam splitter lead to a collimated acceptance angle of 50/1500 ~30 mrad. The vertical divergence of the synchrotron beam is 1.2 mrad.

Amplitude Dividing Beam Splitters

The use of suitable amplitude dividing beam splitters, analogous to half-silvered mirrors, would benefit future instruments which do not have the high-brightness, small source of synchrotron radiation. The limitations of coherent illumination of the beam splitter is removed, thus allowing much larger source sizes. For the Advanced Light Source synchrotron source this is not a problem since the source size is so small and the brightness high. Inverse photoemission and soft x-ray flourescence interferometer/spectrometers could operate very efficiently at reasonable source sizes (.5-1 mm) with amplitude dividing beam splitters. Luis DaSilva at Lawrence Livermore Laboratory has been developing a Si/Mo amplitude dividing beam splitter for plasma diagnostics[11]. However, the slope errors are on the order of 5000 Å, which is not suitable for spectroscopic optics [their application looks for spatial fringe shifts as a plasma diagnostic]. In addition, the absorption coefficients and required incidence angles for our energy range of interest make these beam splitters undesirable.

Translation Stage Drive

The problem of moving a mirror smoothly on the scale of nanometers and milliseconds at ~20 μm/sec velocity for 1 cm of travel is a fairly unique problem. The smooth motion is required to obtain the oscillating photon intensity without the distortion of frequency-dependant effects in the detector-amplifier-ADC signal chain. The motion must also be smooth compared to the bandwidth of the mirror position readout. It is also desirable to not generate any temperature gradients at or near the mirror stage or frame. The smoothness criteria precludes any use of conventional bearing systems and the desire to avoid temperature differentials makes any electromotive mechanism unappealing.

Our solution to these problems consists of a specially designed, double acting, hydraulic piston mounted outside the vacuum vessel. The working fluid is mineral oil. The key factors which achieve the smooth motion are: 1) the drive shaft slides on two O-rings with an oil bath on both sides of each O-ring, 2) a reasonably polished shaft (final sanding: 600 grit sand-paper on a lathe, then emery cloth for a few minutes), 3) the O-rings have as small a cross-section as possible. Fat O-rings stick slip a lot, probably because the oil is squeezed out of the center region of contact with the drive-shaft.

Errors, Noise, and Performance Expectations of the FT-SX Interferometer

Phase Errors

In considering the design and implementation of a high-resolution Fourier transform spectrometer for the soft X-ray region, it has become clear that the precision of the path length difference (phase) measurement is a critical aspect of the instrument because of constraints imposed by the short wavelengths of soft X-rays.

Analysis of Phase Errors

Introduction

We investigate the effects of periodic and random phase measurement errors on the frequency spectrum, derived from the Fourier transform of the interferogram, and the signal-to-noise ratio. Periodic phase errors lead to sidebands with positions determined by the period of the error and amplitudes that depend on the ratio of the maximum error to the wavelength. Random phase errors give rise to white noise in the frequency spectrum, with a signal/noise ratio proportional to the square root of the number of measurements and inversely proportional to the standard deviation of the measurement error .

The precision of the path-length difference measurement is a key aspect of the operation of the spectrometer. This problem, while previously recognized, has not been of great concern as most Fourier transform spectroscopy has been carried out in the infra-red region, where the wavelengths are relatively long[8]. We call an error in path-length difference a "phase error" in the measurement of the interferogram. Amplitude errors, such as detector noise and photon counting statistics, will be treated elsewhere. We consider only the phase error effects here. We first give a brief description of the FT-SX spectrometer and the equations used to represent the interferogram, then we discuss phase errors and their effects under the categories of constant, periodic, and random phase errors. The FT-SX spectrometer under construction at the Lawrence Berkeley National Laboratory will use, as a light source, the narrow bandwidth output of a spherical grating monochromator on a bend-magnet beam line at the Advanced Light Source. Before the detector will be a gas absorption cell containing, for example, helium. The interferogram will be sampled by moving the mirrors of a Mach-Zehnder interferometer continuously at a slow speed, inducing a continuously varying path-length difference (PLD) between the two arms of the beam, and recording the signal at constant position intervals. To obtain the desired resolution of 10^6 the interferogram must be very long, about 1 cm for the soft X-ray wavelength range. Additionally, the resolution of the position measurement should be a small fraction of the soft X-ray wavelength, e. g., 5-10 Å. This combination of very high resolution position-measurement and long travel distance has led us to select heterodyne laser interferometry as the position measurement method. There are commercially available systems based on this method, using a HeNe laser with a claimed resolution of <6 Å. However, certain errors, both random and periodic, are known to be associated with these devices [12]. It is our desire to understand and estimate the effects of these phase errors on the final absorption spectrum and to correct for them if necessary.

The function used for the investigation of phase errors is the interferogram function for a monochromatic source,

$$S_g = \cos(\omega_g x + 2\pi\varepsilon_x) = \cos\left(\frac{2\pi}{\lambda_g}x + 2\pi\varepsilon_x\right)$$

where ω_g, λ_g are the frequency and wavelength of the light, x is the induced path-length difference, and ε_x is the phase error in fractions of a wavelength, and is usually dependent in some way on x. The amplitude is set to unity for convenience. The Fourier transform of this function is a delta function at frequency ω_g. The discrete form is,

$$S_g = \cos\left(\frac{2\pi n}{p} + 2\pi\varepsilon_n\right)$$

where n is the sample position index, p is the number of sample points per period of the signal, and ε_n is the phase error. Appendix A has a more complete discussion of the connection between the above equations and the meaning of their parameters. We can characterize the types of phase errors based on whether ε_n is constant, periodic, or random.

Case 1: Error is constant

This case corresponds to missing the zero path-length difference position, creating a sampled output signal that no longer appears even. Collection of the two-sided interferogram (sampling both sides of the zero path-length-difference) allows for correction of this problem, but it must be dealt with properly to obtain a correct energy spectrum. We would point out that, in general, this results in a frequency-dependent loss of information since the odd parts of the signal near the Nyquist frequency are attenuated or lost completely. This problem, which is largely a data analysis problem, has been treated elsewhere as it is common to all Fourier transform spectroscopies [13]. We will only briefly describe it here, following closely Foreman et. al. The basic result is that while a simple absolute value of the complex Fourier transform will recover the spectrum, that operation is nonlinear and leads to a decrease in the signal-to-noise ratio for small signals. A correction to the two-sided interferogram restoring the even symmetry is possible.

Starting with the interferogram function with zero error

$$S(x) = \int B(\gamma)\cos(2\pi\gamma x)\,d\gamma$$

the interferogram is even and symmetric and the spectral distribution can be determined from the Fourier transform

Case 2: Error is periodic

It is known that heterodyne interferometers suffer from periodic errors in their position measurements due to imperfect separation of the two different frequency components [12]. The period is that of the nominal wavelength of the laser light used. Thus, for a HeNe laser there is an error that has a period of 633/4 nm in translation for a four-pass plane mirror system.

We may represent this error, in units of path-length distance, as

$$\mathrm{E} = \beta \sin(\omega_m x)$$

then our signal becomes

$$S_g = \cos(\omega_g x + \mathrm{E}) = \cos(\omega_g x + \beta \sin(\omega_m x))$$

where ω_g is the frequency of our (monochromatic) signal and ω_m is the effective frequency of the laser position indexer. The signal is thus an angle-modulated function. The maximum position measurement error is β. Because the mirrors are arranged for grazing reflections of the soft X-rays, there is a geometric factor relating the movement of the mirrors and the path-length difference introduced. This factor, along with the optical arrangement of the laser position transducer, leads to an "effective" period when compared to the soft X-rays. We show in appendix B that this function is equivalent to

$$\begin{aligned}
S_g &= \sum_t J_t(\beta)(-1)^t\left[\cos\left(\left(\omega_g - t\omega_m\right)x\right) - \cos\left(\left(\omega_g + t\omega_m\right)x\right)\right] \\
&= J_0(\beta)\cos\left(\omega_g x\right) \\
&\quad -J_1(\beta)\left[\cos\left(\left(\omega_g - \omega_m\right)x\right) - \cos\left(\left(\omega_g + \omega_m\right)x\right)\right] \\
&\quad +J_2(\beta)\left[\cos\left(\left(\omega_g - 2\omega_m\right)x\right) - \cos\left(\left(\omega_g + 2\omega_m\right)x\right)\right] \\
&\quad -J_3(\beta)\left[\cos\left(\left(\omega_g - 3\omega_m\right)x\right) - \cos\left(\left(\omega_g + 3\omega_m\right)x\right)\right] \\
&\quad + \;\ldots
\end{aligned}$$

where the J's are Bessel functions of the first kind ^{14}. Thus the result is a set of symmetrically spaced sidebands (ghosts) about the real signal at multiples of the modulation frequency. The amplitude of the modulation function (the maximum error in path-length difference) determines the amplitudes of the sidebands. The larger the modulations, the more sidebands that become apparent. With no modulation , $\beta = 0$, the formula reduces to a single frequency at the original signal peak, as expected. For small modulations only the first sideband has a non-negligible intensity. The total power in the spectrum

$$J_0^2(\beta) + 2\sum_t J_t^2(\beta) = \frac{1}{2}$$

is constant. So with a periodic angular modulation (position measurement error), power is removed from the main peak and appears in the sidebands. All of these sidebands scale with the intensity of the signal. One should note that, although the main signal loses power, any multiplicative noise will, in general, not be reduced. Thus one loses signal/noise with this kind of phase error.

To make use of the above results and apply them to the case of position measurement error in Fourier transform spectrometry, we write the position as

$$x \to x + \beta \sin\left(\frac{2\pi x}{\lambda_m}\right)$$

and have for the signal

$$S_g = \cos\left[\left(\frac{2\pi}{\lambda_g}\right)\left(x + \beta \sin\left(\frac{2\pi x}{\lambda_m}\right)\right)\right] = \cos\left[\frac{2\pi x}{\lambda_g} + \frac{2\pi\beta}{\lambda_g}\sin\left(\frac{2\pi x}{\lambda_m}\right)\right]$$

$$= J_0(2\pi\beta')\cos\left(\frac{2\pi x}{\lambda_g}\right)$$

$$-J_1(2\pi\beta')\left[\cos\left(\left(\frac{1}{\lambda_g} - \frac{1}{\lambda_m}\right)2\pi x\right) - \cos\left(\left(\frac{1}{\lambda_g} + \frac{1}{\lambda_m}\right)2\pi x\right)\right]$$

$$+J_2(2\pi\beta')\left[\cos\left(\left(\frac{1}{\lambda_g} - \frac{2}{\lambda_m}\right)2\pi x\right) - \cos\left(\left(\frac{1}{\lambda_g} + \frac{2}{\lambda_m}\right)2\pi x\right)\right]$$

$$- \ \mathrm{L}$$

$$\beta' = \frac{\beta}{\lambda_g}$$

It is important to notice that the amplitudes of the peak and sidebands are in general dependent on the ratio of the modulation amplitude (maximum position error) to the wavelength of the spectral component of interest. The figure below plots the amplitudes of the main peak (normalized to 1 at zero modulation) and first sideband versus of the fractional deviation β' as written above.

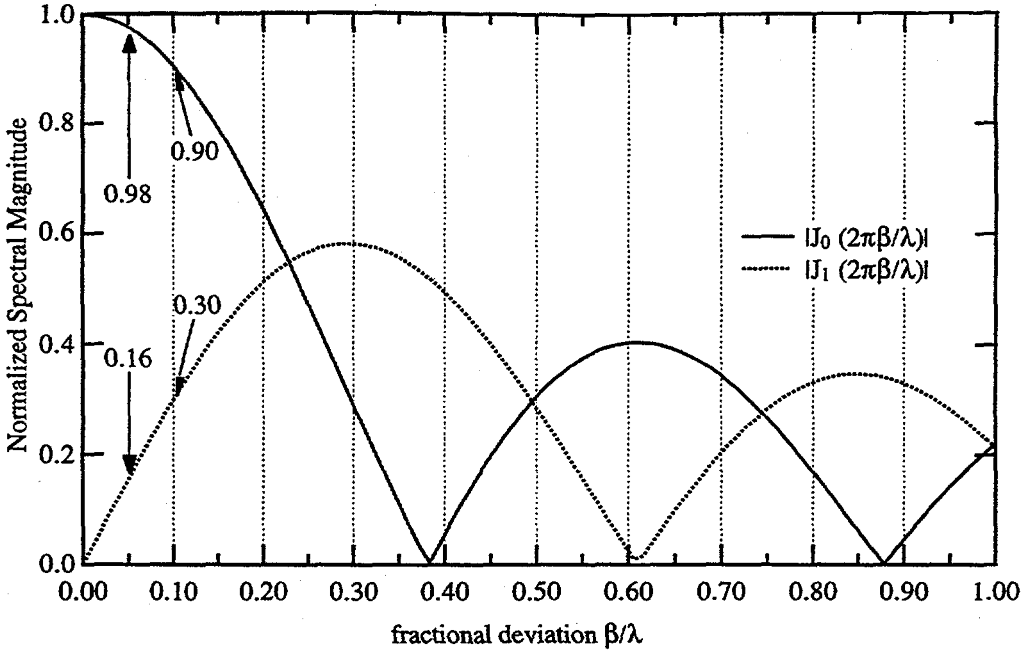

Main peak and 1st side-band magnitudes vs. amplitude of periodic position error.
The effect of periodic position errors is to create sidebands of each peak whose magnitudes vary with the maximum position error. As illustrated, an error of 10% of the wavelength of the main line leads to a 10% loss in amplitude to the side bands.

From the figure, an error of ±5% of the wavelength reduces the main peak amplitude has dropped by 2% (5% of the power is lost to the sidebands). At ±10% the amplitude has dropped by 10% and the first sidebands have risen to 30% of the amplitude of the main peak. Now we need to consider two questions regarding the performance of the FT-SX interferometer: a) where are the sidebands most likely to be, and b) what are tolerable periodic errors of the position measurement system?

To answer the first question we must determine the effective period, λ_m, of the laser position transducer. From the geometry of the instrument, the wavelength of the HeNe, and the four-pass optics layout, we find that the position error is equivalent to a 58 nm modulation period. This means that the "ghosts" will appear in the Fourier transform spectrum at ±21 eV from the real signal. This is quite far out of the range of the bandwidth of the incoming light (~1% at 65 eV). Therefore, the only effect on the final spectrum will be to reduce the signal-to-noise ratio, provided that precautions are taken to ensure there is no aliasing of the ghosts back into the spectrum. It may prove to be desirable to keep all of the sideband spectra to add into the total.

To answer the second question we need to consider the amplitude of the periodic measurement errors. Our criteria for evaluating acceptable intensity loss of the signal is to try to keep the loss of the same order as the photon shot noise level in the spectrum. For a signal/noise amplitude ratio of 300, as estimated for the FT-SX [15] for a single scan, this would entail an amplitude loss to 0.9967 or only 0.33%. Making use of the limiting relation when $\beta' << 1$ for the zeroeth order Bessel function

$$J_0 \cong 1-\left(\frac{\beta'}{2}\right)^2$$

$$\beta' \cong 2\sqrt{1-J_0}$$

Plugging in 1/300 for $1-J_0$ gives a PLD error of β'=0.115 and, again using the geometric factors of the instrument, we get a position measurement fractional error of 4.4%. For the nominal wavelength of 200 Å this becomes ±9 Å of error. This is a realistic goal and should be achievable with the laser interferometer. To operate at higher energies requires even tighter tolerances. At 100 Å (120 eV) the allowed error of 4.5 Å becomes more challenging. With a fractional error of 10% of the x-ray wavelength we still lose only 10% of the signal amplitude.

Case 3: Error is random

The effects of random errors in the sample position become important when the resolution of the position measurement system is comparable to the wavelengths of light passing through the instrument. In particular, the heterodyne laser interferometer has a noise component in the output due to variations in air density in the laser path, noise in the measurement electronics, etc. Heuristically speaking, one would expect such noise to generate many ghosts in the final spectrum. This can be understood from the results of the investigation of periodic errors discussed above and from the statistical properties of a noise wave form (see appendix C). We would expect the distribution of noise in the final (energy) spectrum to be white (each a ghost from one spectral component of the modulating noise) with magnitudes following a Rayleigh distribution.

In order to asses the effect of such phase noise on the final Fourier-transform spectrum, numerical simulations have been carried out. We begin again with the relation

$$S_g = \cos\left(\frac{2\pi n}{p} + 2\pi\varepsilon_n\right)$$

and let ε_n vary randomly from one sample point to the next. The probability distribution used to generate the error term is gaussian with zero mean obtained from an integer distribution with $2^{32} - 2$ values using the Central Limit Theorem with 12 samples [16]. Note that the units of the error term ε_n is in fractions of the monochromatic signal's wavelength. The interferograms were generated by "sampling" the function, assuming equally spaced intervals, but allowing the error term to modify the value obtained in that sample. The amplitude signal to noise ratio (S/N) were estimated for each interferogram. The signal amplitude was estimated by taking the total intensity under the "peak" in the fast Fourier transform (FFT) and subtracting the mean intensity of the noise away from the peak. The standard deviation of the spectral components away from the peak were calculated using a large number of their magnitudes. The ratio of the two is the S/N. For example, The figure below shows 5 periods of a g=256 period interferogram with p=8 points/period and a noise standard deviation of 0.100. Also shown is the zero noise function for comparison. The Fourier transforms of those two interferograms are shown as well. The general feature to be noticed is that the spectrum of the interferogram with phase noise shows a reduction in peak intensity and a distribution of noise components across the entire frequency spectrum (the full range of the FFT is not shown in the figure).

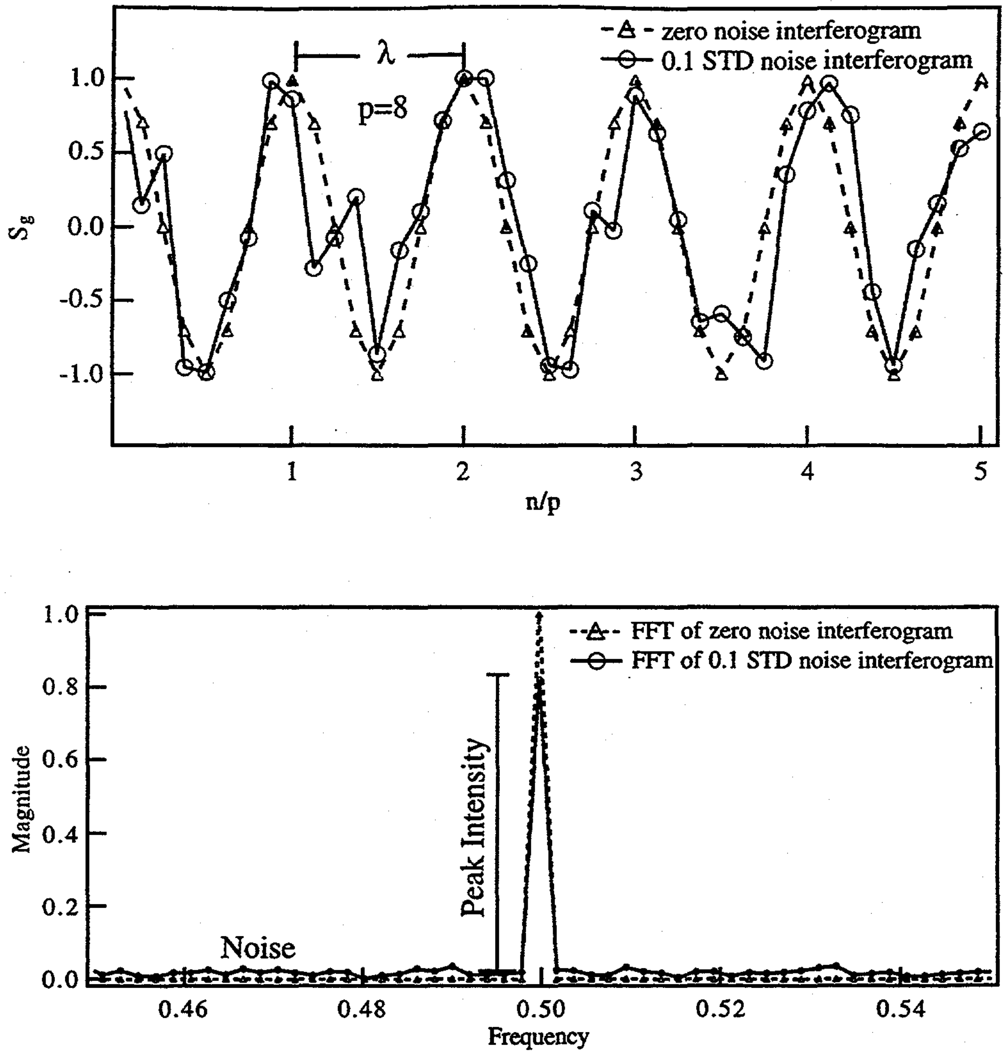

Interferograms, with and without position noise in sampling, and their FFT's.
The sample rate is 8 points/period and 256 periods were included (but not shown).

A histogram of the noise amplitudes from the above Fourier transforms, shown below, confirms our expectation regarding the statistical distribution of the noise amplitudes.

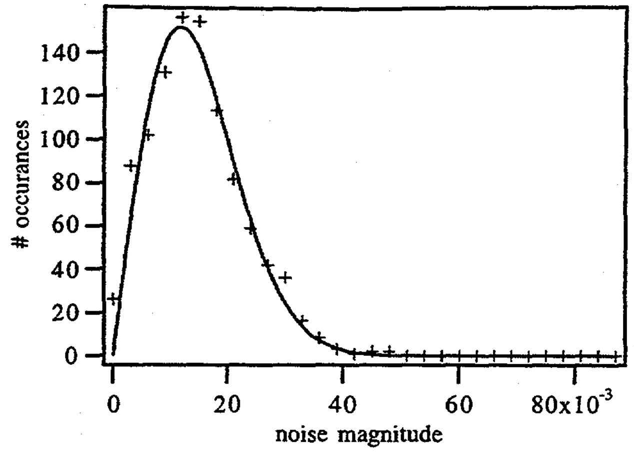

Histogram of noise amplitudes in the FFT.
The solid line is a Rayleigh distribution, which fits as expected.

The three parameters, p (number of samples/period), g (total periods included in sample set), and σ (standard deviation of gaussian noise) of ε_n, were varied independently while holding the other two constant in order to ascertain their effect on the Fourier transform. The number of sample points per period, p, was varied from 2 to 64. The number of periods of the signal included in an interferogram, g, were varied from 64 to 256 and the rms value of the phase noise was varied from 0.001 to 0.5. The latter number can be understood as the standard deviation of the position error being ±1/2 period. As discussed in the Appendix A, the equations and parameters are defined such that the frequency scale is normalized to the main signal, which always appears at 1/2 Hz.

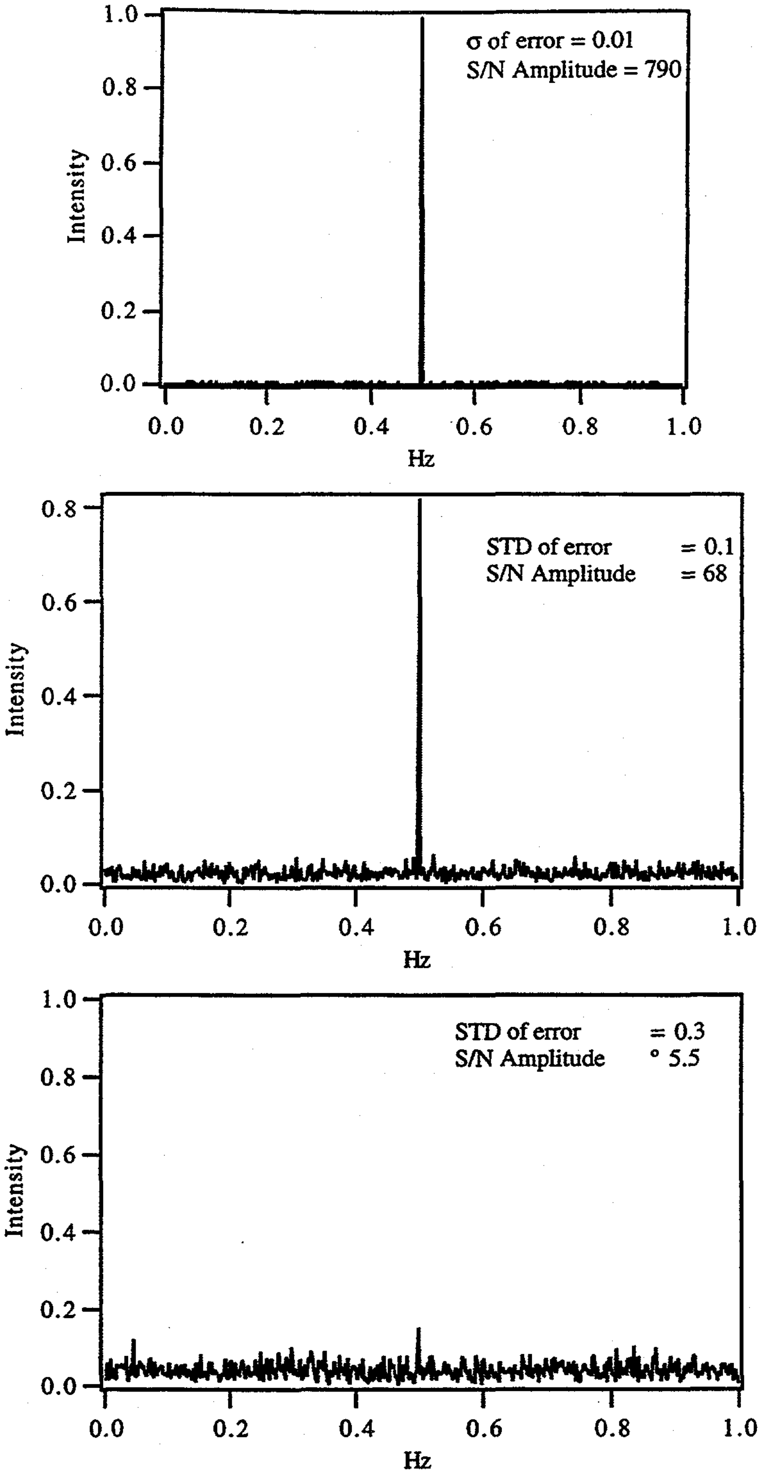

Simulated spectra with random position errors (σ) of 0.01, 0.1, and 0.3 of a period.

Included are 256 periods with a sampling rate of 4 points/cycle. The signal/noise amplitude ratio is shown for each (see text for calculation method).

The figure above shows the magnitudes of the FFT's of three interferograms in which the noise σ was 0.01, 0.1, and 0.3. The number of samples per period, p, is 4 and the total number of periods included, g, is 256. Shown in each figure is the estimated signal to noise amplitude ratio for these spectra. The results of these simulations can be summarized as follows:

$$\frac{S}{N} \propto \frac{1}{\sigma}, \quad \text{for } \sigma \leq 0.1$$

$$\frac{\mathrm{S}}{\mathrm{N}} \propto \sqrt{p}$$

$$\frac{S}{N} \propto \sqrt{g}$$

Putting all of these together we get

$$\frac{S}{N} = c\frac{\sqrt{pg}}{\sigma} = \frac{\sqrt{N}}{4\sigma}$$

and we find that the signal to noise ratio varies inversely with the increase in position noise and directly with the square root of the total number of observations, which, in retrospect, is not surprising. "c" is just a constant of proportionality which we find to be about 1/4. The trends stated above deteriorate for larger position measurement errors as the peak gets completely washed out in the noise. Also, for the Nyquist sample rate, p=2, the signal to noise is a little higher than indicated by the trend above since the derivative of the signal is zero at the crests and troughs. Of course, since real spectra are not delta functions, the values for larger sampling rates probably extrapolate back to 2 since one is probably not always sampling at the extrema. It is interesting to note that the peak positions and line shapes are not affected beyond that of the addition of random noise, as shown below.

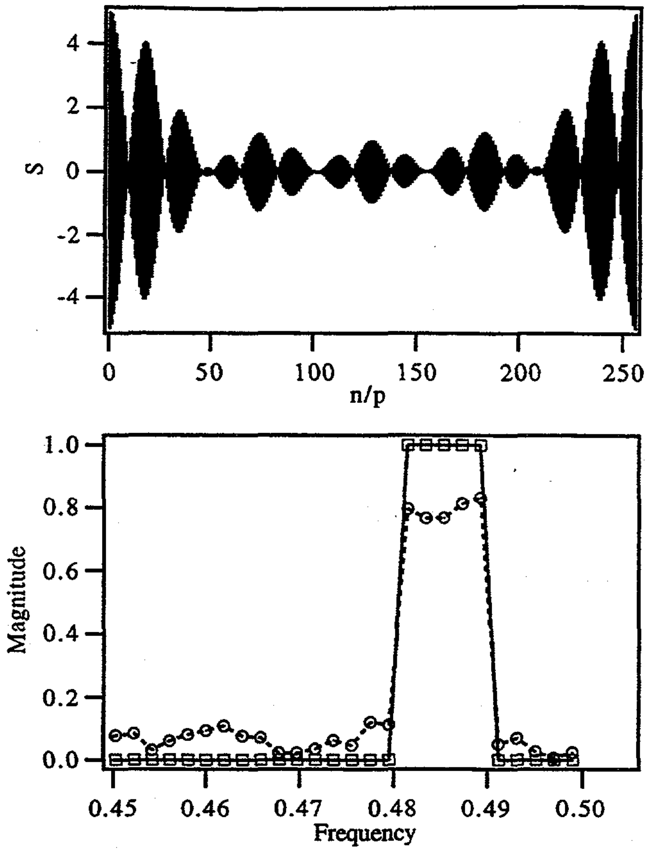

Interferogram of 5 component "peak" with noise and its FFT.
Only the envelope of the interferogram is visible. The line shape in the FFT is not affected other than by the addition of random noise.

What these results mean is that one overcomes the effects of noise in the sample position by increasing the sample rate until the bandwidth of the position measurement noise is exceeded. This sets the maximum necessary sampling rate of the system until the other sources of noise, e.g. detector or photon shot noise, become dominant. The benefit in signal to noise is still realized even if a filter is applied to the over sampled signal and then decimated back to the necessary sample rate. Practically speaking, for ultra-high resolution spectra where ~10^6 periods are included, the minimum number of data points is $2\text{x}10^6$. An σ of 0.1 (~10 Å for the FT-SX) still gives a S/N contribution of ~3000 which is insignificant compared to the expected contributions from the photon shot noise. For broad bandwidth studies, though, the benefit may be more important since most of the information is contained in a relatively narrow region around the zero PLD. Sampling at PLD's beyond which the oscillations have died out do not count.

Position Measurement System of the FT-SX

Periodic Errors

The periodic error was measured using the phase-difference method of Hou, et. al. [12,17]. The measurement was carried out in air with the flight path of the split laser beams enclosed in a plastic box. The laser beam passed through a hole in the box. The non-linearity was found to have less than 0.5 nm amplitude deviation, which is well within our specifications above. However, in the final system, the laser beam will pass through a vacuum viewport. This may create some additional non-linear character.

Random Errors

The measured noise level of the HP interferometer in air, enclosed with a box, is 4.5 Å rms, which satisfies very well the criteria set above. The resolution is only 3 Å, so we cannot expect to do better than this with individual position samples. The high sampling rate of 100 kHz afforded by the HP VME-base electronics does allow a great deal of compensation for this noise by oversampling the position.

Amplitude Errors

Amplitude errors in FTS, and indeed in most spectrometric techniques, arise from the statistical noise associated with electronic signals as well as the intrinsic "counting statistics". We consider below the noise due to photon counting statistics, random background noise, quantization noise of the Analog-Digital converter.

Photon Shot Noise

A well designed and fabricated spectrometry system will reach the limit of counting statistics of the photons detected. The signal/noise ratio for FT spectrometry is given by[7]

$$\frac{S}{N} = \frac{M\sqrt{\Phi}}{N}$$

where M is the modulation amplitude of the signal, Φ is the total number of photons detected, and N is the number of sample points. Simulations suggest $M \approx .005$ for the helium double excitation series. For 1000 seconds of integration time of 10^{12} photons/sec and 1000 sample points (from 10^6*BW) we get a signal/noise ratio

$$\frac{S}{N} \cong 160$$

for a single scan.

1/f Noise

The low frequency noise associated with any measured signal must be dealt with. This noise includes the ubiquitous 60 Hz AC power and beam intensity fluctuations caused by mechanical resonances in the storage ring and beam line. In conventional gas-ionization cells the noise is bandwidth limited by simple averaging. Scanning Fourier transform spectrometers like the FT-SX deal with this problem in a much better way: the mirrors are scanned at a constant rate which causes the measured signal, the interference fringes, to become time varying in a controlled way. One simply chooses a mirror velocity that moves the signal frequency up out of the low frequency noise and then filters the signal. For the FT-SX helium double excitation series the wavelength of the x-rays is approximately 20 nm. Scanning the mirrors at ~15 μm/sec results in a 1 kHz signal frequency, which is well away from the low frequency interferences. This rate is also very compatible with modern analog sampling electonics and power supplies.

ADC Quantization Noise

The discrete nature of the analog-to-digital converter amplitude conversion adds noise to a signal. That noise depends on the resolution (number of bits) of the converter. Selection of a proper converter depends on the expected signal/noise ratio.

To calculate the quantization noise power we find the variance of the error e

$$\sigma^2 = \int_{-q/2}^{q/2} e^2 p(e)de = \frac{1}{q}\int_{-q/2}^{q/2} e^2 de = \frac{q^2}{12}$$

where $q = 2V/2^b$ is the unit of quantization, i.e. number of volts per dac step, V is the maximum amplitude of the input voltage, so that $2V$ is the total range, and b is the number of bits of resolution of the converter[18]. Now consider a signal whose amplitude is a V, where a is the fraction of the total amplitude in the input signal. The power of the signal is then a $V/2$ and the signal/noise ratio is then, at worst,

$$\frac{S}{N_{adc}} = 3a^2 2^{2b-1}$$

The expected signal/noise due to the photon counting statistics is about 300 for 1 scan of the interferometer. The signal fraction of total will be at worst ~0.1%. Hence, from the above equation we find that an ADC with 16 bits will give a signal/noise power of 6000, which is sufficient. Note that this is worst case since the power is distributed randomly throughout the entire frequency range of the spectrum while the spectrum only occupies a narrow band in this region. Thus oversampling effectively adds more bits of resolution to the ADC. Thus the 16 bit, high-speed ADC will readily provide the necessary resolution.

Data Acquisition and Control System

The data acquisition and control system must meet several time-critical tasks while acquiring an interferogram and must allow easy use, configuration, and control of the acquisition process.

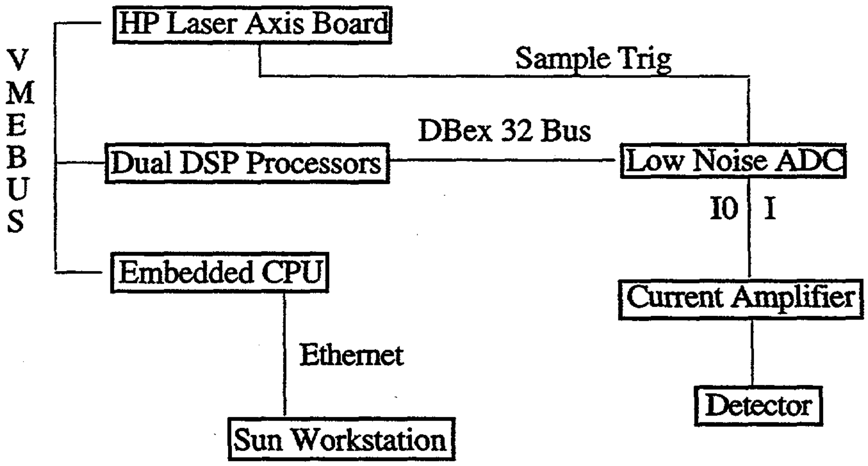

Schematic of Data Acquisition and Control Electronics

Detector and Current Amplifier

The detector is a silicon photodiode with an extra thin passifying oxide layer on the surface to allow soft x-ray detection. These detectors have been shown to have a high quantum efficiency in the soft x-ray range[19]. The detector and current amplifier impedence must be properly matched to ensure low noise operation.

Signal Acquisition

The signal from the current amplifier is converted with a low noise, high speed analog to digital converter. The sample trigger clock runs at 100 kHz and is also brought out to the external trigger input of the HP laser position measurement board. This ensures synchronous sampling of the position and current. Digital signal filters are then applied by the Digital Signal Processor chips to filter out the noise. The signal is then decimated to a fraction proportional to the known band-width of the incident x-rays. This aliasing is done after the filtering to avoid stacking all of the noise into the final spectrum. The decimated signal is then stuffed into a buffer in the embedded CPU. The embedded CPU takes care of passing the data along to the control/display workstation as well as starting, stopping, and saving the acquisition process.

Expectations Regarding the Measurement of Helium Double Excitations with the High Resolution Fourier Transform Soft X-ray Spectrometer

Introduction

The helium double excitation series are the primary spectroscopic series to be investigated. There are, theoretically, infinitely many peaks which get sharper as the ionization threshold is approached[5].

Signal Simulation

In order to determine what kind of signal to expect from this absorption system, I have performed some simulations of the absorption spectrum by inverse FFT of the theoretical curves and an assumed incident photon spectrum. The top panel of the figure below shows a gaussian energy profile of 1 eV width with the absorption due to the 2n+ series of the helium double excitation spectrum previously measured[20]. The lower panel shows an expanded view of the first 40 μm of path length difference determined by the inverse FFT of the top spectrum. Note that the oscillations are approximately .02% of the average intensity. The actual experiment will be done with a 0.1 eV width incident photon energy. This will increase the relative oscillations to ~0.2%.

Gaussian Distribution

@65 eV, Sigma=0.5 eV,2 meV Point Density
With He Resonance Absorptions
2n+ series, peaks 2+ to 7+

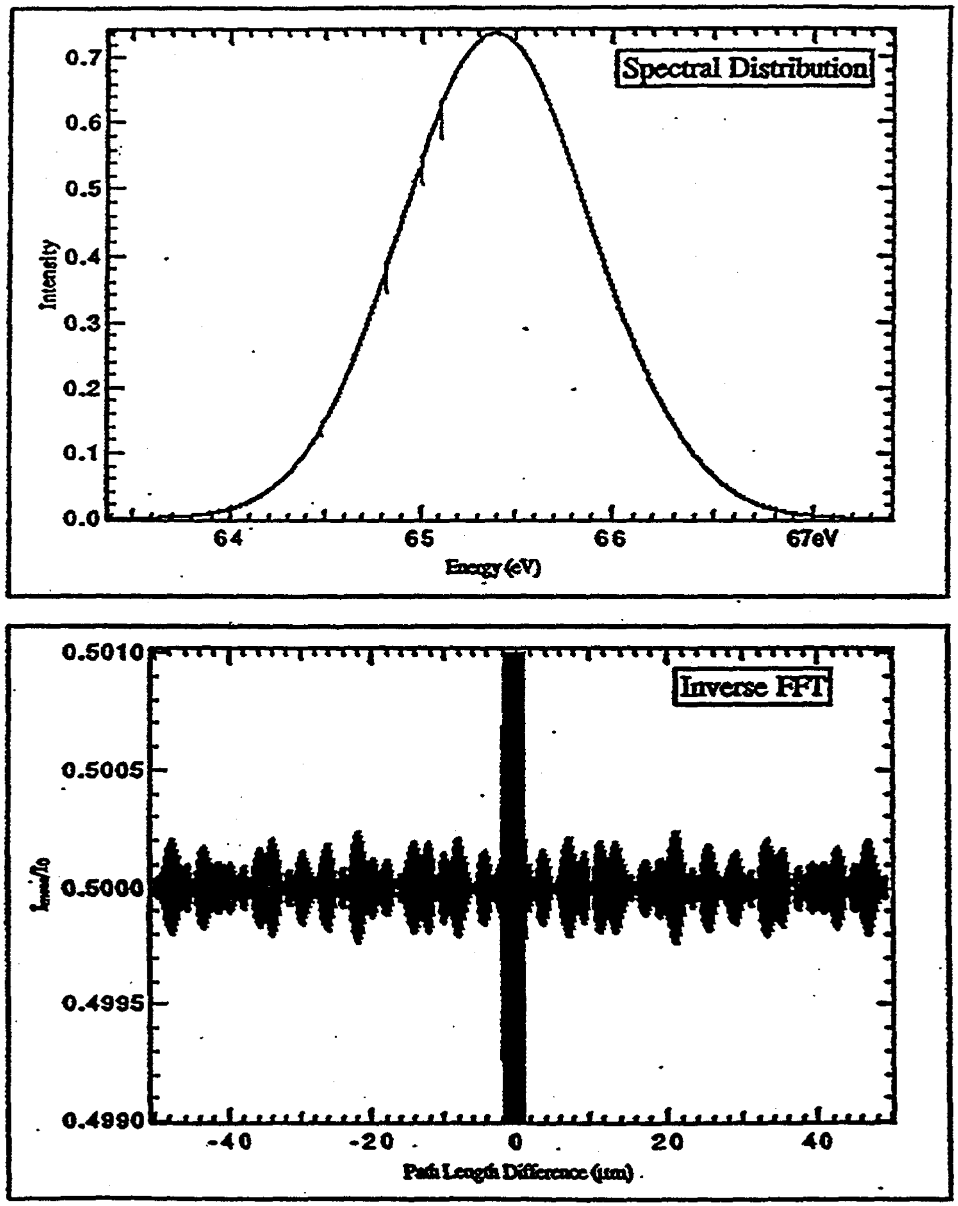

Simulated Absorption Spectrum and Signal

Experimental

The gas sample is contained in a conventional gas ionization cell upstream of the interferometer. The collected ion signal can be used as a normalization since the monochromator is not scanned. Additionally, a metal grid can be used for flux normalization.

One could worry about doppler broadening of the sharpest lines. An analysis of the doppler broadening for helium at room temperature, based on the kinetic theory of gases and non-relativistic doppler shifts[21] gives a broadening of $2\text{x}10^{-7}$ resolving power at 65 eV and 300 K. This is still an order of magnitude less than the theoretical best resolving power of the spectrometer.

Appendix A: The Interferogram Function

We now discuss the functions and notations used for the discussion and simulations and the various interpretations that can be applied to understand what they mean. The output signal of an interferometer is given by

$$I(x) = \frac{I_0}{2}\left(1 + \int B(\gamma)\cos(2\pi\gamma x)\,d\gamma\right) \quad (A1)$$

The oscillatory part of the signal contains the spectral information. We write this interferogram function as

$$S(x) = \int B(\gamma)\cos(2\pi\gamma x)\,d\gamma \quad (A2)$$

where $\gamma = 1/\lambda$ is the wave number, x is the path length (phase) difference between the two beams in the interferometer, and $B(\gamma)$ is the spectral distribution of the signal. If the function is of finite length ΔL it can be uniquely resolved into a sum of discrete cosines and sines with frequencies which are integral multiples of the resolution $\delta\gamma = 1/2\Delta L$. We will only consider the even (real) functions in S here and thus write

$$S(x) = \sum_{k=1}^{\frac{\Delta L}{2}} b_k \cos\left(\frac{2\pi k}{\Delta L}x\right) \quad (A3)$$

where k is the frequency index (*not* the wave vector). For simplicity and clarity we will assume that the spectral amplitudes, b_k, are unity. If we sample this function at intervals δl then we can write

$$S(n)=\sum_{k=1}^{\frac{\Delta L}{2}}\cos\left(\frac{2\pi k}{\Delta L}n\delta l\right) \qquad (A4)$$

The run of a single frequency component of this function is written as

$$S_k=\cos\left(\frac{2\pi k}{\Delta L}n\delta l\right) \qquad (A5)$$

where the dependence on n is implicit. Since $\Delta L / \delta l$ is the total number of points, which we call N, we arrive at yet another form of the function which is commonly used when discussing FTS,

$$S_k=\cos\left(\frac{2\pi kn}{N}\right); \quad n=1,2,\ldots,N \qquad (A6)$$

To summarize what we have so far:

N	is the total number of sample points
n	is the sample position index
k	is the frequency index

We find it convenient to introduce two new parameters which provide a more natural scale for illustrating the various effects of errors, p and g, particularly when we are only considering a single frequency, i.e. an ideally monochromatic source. First we introduce these parameters, then describe how they are related to the other parameters and discuss their interpretation. We define the total number of points to be

$$N=pg \qquad (A7)$$

thus

$$k=1,2,\ldots,\frac{pg}{2} \qquad (A8)$$

Then we can write the signal as

$$S_k=\cos\left(\frac{2\pi kn}{pg}\right) \qquad (A9)$$

We take our signal of interest to be a single spectral component of frequency $k = g$. Then we can write, for our principle signal,

$$S_g = \cos\left(\frac{2\pi gn}{pg}\right) = \cos\left(\frac{2\pi n}{p}\right) \qquad (A10)$$

Because we have tied the total number of points to g and p, we can now consider g to be the number of periods of our signal which are included in our data set (the sample range) and p is the number of points/period (the sample rate). Looking at the previous equation one can see that every time n is a multiple of p the function has gone through one cycle. In addition, we define the frequency scale of the transform such that

$$\delta f = \frac{1}{2g} \qquad (A11)$$

so that at our signal frequency

$$k\delta f = \frac{g}{2g} = \frac{1}{2} \qquad (A12)$$

hence our signal always has a frequency of 1/2 Hz in this scale, independent of the sample rate p or the total number of periods g included. We also find that the total frequency range of the transform is

$$\Delta f = k_{\max}\,\delta f = \frac{pg}{2} \times \frac{1}{2g} = \frac{p}{4} \qquad (A13)$$

So at the Nyquist sampling rate, $p = 2$, we find $\Delta f = 1/2$, i.e. our signal peak comes at the last channel of the transform. Naturally, increasing the sampling rate increases the frequency range of the transform, but the signal peak remains at $1/2$. Also, increasing the number of periods included in the data range improves the resolution of the transform. To summarize our parameters

p	number of points/period of our signal,
g	number of periods included in the data range(or frequency),
$N = pg$	total number of points sampled,
$n = 1\ldots N$	sample position index,
$k = 1\ldots \frac{pg}{2}$	frequency index, and
$S_g = \cos\left(\frac{2\pi n}{p}\right)$	sampled output of the detector. The signal amplitude is assumed to be one.

When dealing with only the signal frequency, there is another approach to arrive at the above expression. Backing up a few steps, but considering a monochromatic signal of wavelength $\lambda = 1/\gamma$, we can write

$$S_g = \cos\left[\left(\frac{2\pi}{\lambda}\right)n\delta l\right] \qquad (A14)$$

where δl is, again, the sampling interval. If we write δl in terms of the wavelength and the number of samples per wavelength $\delta l = \lambda / p$ then

$$S_g = \cos\left[\left(\frac{2\pi}{\lambda}\right)n\left(\frac{\lambda}{p}\right)\right] = \cos\left(\frac{2\pi n}{p}\right) \qquad (A15)$$

We now have an ideal signal function to which we can introduce errors for the purpose of determining their effect on the final spectrum.

Appendix B: Derivation of the Angle-Modulated Cosine Function

We derive the spectral form of an angle-modulated cosine. This corresponds to a periodic position measurement error in a sampled interferogram. If the modulation function (position measurement function) is

$$\mathrm{E} = \beta \sin(\omega_m x) \qquad (B1)$$

then the signal becomes

$$S_g = \cos(\omega_g x + \mathrm{E}) = \cos(\omega_g x + \beta \sin(\omega_m x)) \quad (B2)$$

where ω_g is the frequency of the (monochromatic) signal and ω_m is the effective frequency of the position indexer. The maximum position measurement error is β. We will now derive an equivalent expression for this function that shows the harmonic content of the Fourier transform following Taub and Schilling [22]. Using

$$\cos(a+b) = \cos(a)\cos(b) + \sin(a)\sin(b) \qquad (B3)$$

we get

$$S_g = \cos(\omega_g)\cos(\beta\sin(\omega_m)) - \sin(\omega_g)\sin(\beta\sin(\omega_m)) \qquad (B4)$$

Now the cosine-of-sine and sine-of-sine terms can be expanded as

$$\cos(\beta\sin(\omega_m x)) = J_0(\beta) + 2\sum_{t=1}^{\infty} J_{2t}(\beta)\cos(2t\omega_m x)$$
$$\sin(\beta\sin(\omega_m x)) = 2\sum_{t=0}^{\infty} J_{2t+1}(\beta)\cos(2t\omega_m x) \qquad (B5)$$

where the J's are Bessel functions of the first kind [14]. Substituting the previous two relationships back into the expansion and using standard trigonometry identities for the products of cosines and sines we get

$$\begin{aligned} S_g &= \sum_t J_t(\beta)(-1)^t\left[\cos((\omega_g - t\omega_m)x) - \cos((\omega_g + t\omega_m)x)\right] \\ &= J_0(\beta)\cos(\omega_g x) \\ &\quad -J_1(\beta)\left[\cos((\omega_g - \omega_m)x) - \cos((\omega_g + \omega_m)x)\right] \\ &\quad +J_2(\beta)\left[\cos((\omega_g - 2\omega_m)x) - \cos((\omega_g + 2\omega_m)x)\right] \qquad (B6) \\ &\quad -J_3(\beta)\left[\cos((\omega_g - 3\omega_m)x) - \cos((\omega_g + 3\omega_m)x)\right] \\ &\quad + \ \ldots \end{aligned}$$

Thus the result is a set of symmetrically spaced sidebands (ghosts) about the real signal at multiples of the modulation frequency. The amplitude of the modulating wave determines the amplitudes of the sidebands.

Appendix C: Spectral Content of a Random Noise Wave form

We now discuss the harmonic content of a noise wave form. A finite length, sampled noise wave form can always be written as a sum of sines and cosines

$$\begin{aligned} \varepsilon_n &= \sum_k a_k \cos(2\pi k\,\delta f\,n) + b_k \sin(2\pi k\,\delta f\,n) \\ &= \sum_k a_k \cos\left(\frac{2\pi kn}{2p}\right) + b_k \sin\left(\frac{2\pi kn}{2p}\right) \qquad (C1) \\ &= \sum_k c_k \cos\left(\frac{2\pi kn}{2p} + \theta_k\right) \end{aligned}$$

and because the noise is a random, stationary process, the spectral amplitudes of the noise, the a_k, b_k, c_k and θ_k's, are also random variables which have statistically definable properties [22]. It can be shown that the complimentary spectral amplitudes a_k, b_k or c_k, θ_k are uncorrelated with each other and uncorrelated with other spectral amplitudes. The amplitudes a_k, b_k have gaussian distributions with zero mean. In a Fourier transform one usually is interested in the magnitudes and phases, c_k, θ_k. These are related to the amplitudes a_k, b_k in the same manner that random variables in polar coordinates are related to random variables in Cartesian coordinates [22]. Thus the probability distribution of the magnitude is a Rayleigh probability function

$$p(c_k) = \frac{c_k}{\Gamma} \exp\left({}^{-c_k^2}\!/_{2\Gamma^2} \right) \qquad (C2)$$

(with the same variance as the Cartesian variables) and the phase angle has a uniform probability distribution of $1/2\pi$. Making use of the low modulation limit for the sideband amplitude of a phase modulated signal

$$J_1 \cong \frac{\beta}{2} \qquad (C3)$$

we would expect the distribution of noise in the final, sampled spectrum to be white (each a ghost from one spectral component of the noise) with magnitudes following a Rayleigh distribution.

Bibliography

[1] K. Richter, J. S. Briggs, D. Wintgen, and E. A. Solov'ev, Journal of Physics B **25**, 3929 (1992).

[2] C. D. Lin, Phsical Review A **29**, 1019 (1984).

[3] D. R. Herrick, Advances in Chemical Physics **52**, 1 (1983).

[4] J. M. Rost and J. S. Briggs, Journal of Physics B **24**, 4293 (1991).

[5] G. Kaindl, "Ultra-High Resolution Spectroscopy of the He Double Excited States," presented at the Oji International Seminar on Atomic and Molecular Photoionization, Tsukuba, Japan, 1995 (unpublished).

[6] Douglas Vaughan, "X-ray Data Booklet," (Lawrence Berkeley Laboratory, University of California, Berkeley, CA 94720, 1986).

[7] J. W. Brault, "Fourier Transform Spectrometry," in *High Resolution in Astronomy*, edited by A. Benz, M. Huber, and M. Mayer (Geneva Observatory, Sauverny, Switerland, 1985), pp. 1.

[8] J. Chamberlain, *The Principles of Interferometric Spectroscopy* (John Wiley and Sons, Chichester, 1979).

[9] Malcom Howells, Light Source Note Report No. LSBL-186, 1993.

[10] Hecht, *Optics* (Addison-Wesley Publishing Company, Menlo Park, 1987).

[11] Luis DaSilva .

[12] W. Hou and G. Wilkening, "Heterodyne interferometry errors," Precision Engineering , 91-98 (1992).

[13] M. L. Forman, W. H. Steel, and G. A. Vanasse, "Correction of Asymmetric Interferograms Obtained in Fourier Transform Spectroscopy," Journal of Optical Society of America **56** (1), 59-63 (1966).

[14] I. S. Gradshteyn and I. M. Ryzhik, *Table of Integrals, Series, and Products* (Academic Press, San Francisco, 1980).

[15]M. R. Howells, K. Frank, Z. Hussain, E. J. Moler, T. Reich, D. Moller, and D. A. Shirley, "Toward a soft X-ray Fourier-transform spectrometer," Nuclear Instruments and Methods in Physics Research A **347**, 182-191 (1994).

[16]W. H. Press, B. F. Flannary, S. A. Teukolsky, and W. T. Vetterling, *Numerical Recipes in C* (Cambridge University Press, New York, 1990).

[17]Wenmei Hou and Gunther Wilkening, "Investigation and Compensation of the Nonlinearity of Heterodyne Interferometer," Precision Engineering **14**, 91-98 (1992).

[18]Jervis, *Digital Signal Processing* (McGraw-Hill, New York, 1995).

[19]Raj Korde and L. Randall Canfield, "Silicon photodiodes with stable, near-theoretical quantum efficiency in the soft x-ray region," SPIE X-Ray Instrumentation **1140** (1989).

[20]M. Domke, C. Xue, A. Puschman, T. Mandel, E. Hudson, D. A. Shirley, G. Kaindl, C. H. Greene, and G. R. Sadeghpour, "Extensive Double-Excitation States in Atomic Helium," Physical Reveiw Letters **66**, 3441-3443 (1991).

[21]P. W. Atkins, *Physical Chemistry* (W. H. Freeman and Company, New York, 1990).

[22]H. Taub and D. L. Schilling, *Principles of Communication Systems*, 2nd ed. (McGraw-Hill, San Francisco, 1986).

Conclusion

Synchrotron radiation has opened up new avenues of investigation into dilute and many-body systems. In this thesis I have explored aspects of each of these avenues. The high brightness of third-generation light sources allow for the high resolution spectroscopy that enables detailed studies to be performed. The growth in the availability of synchrotron light sources world-wide has led to the increased importance of x-ray photoemission and x-ray absorption techniques.

Three surface structures of molecular adsorbates on transition metal surfaces have been determined. The results demonstrate that theoretical modeling of such systems must include the interactions between adsorbates and between adsorbates with sub-surface atoms, which have not been fully modeled at present. The Angle-Resolved Photoemission Fine Structure (ARPEFS) technique has become routine with the recent development, within Dave Shirley's research group, of highly optimised computer codes for calculating ARPEFS curves for arbitrary initial-state electrons and multiple photoemitters. The importance of the ARPEFS technique appears to be growing as synchrotron facilities become more accessible and as the theoretical modelling becomes more widely understood. The low kinetic energy limit has yet to be explored.

Two approaches to the study of correlated electron systems have been developed: 1) the use of photoelectron diffraction to determine the intrinsic/extrinsic properties and the angular momentum of the peaks due to multi-electron excitation in photoemission, and 2) the design and characterization of a new kind of high resolution x-ray spectrometer for the investigation of helium double excitation with synchrotron radiation. Multi-electron excitations in the photoemission process are found to be primarily monopole excitations, i.e. there is no angular momentum change in the shake-up and shake-off electrons. This greatly reduces the number of excitation channels which are possible.

The Fourier Transform Soft X-ray (FT-SX) spectrometer will provide an extremely sensitive test of electron correlation theories. The design specifications are driven by the short x-ray wavelength and the desired resolving power. The specifications have been met using tools operating at the limits of modern metrology, mechanical design, optical fabrication, and digital signal processing. It is apparent to me that, because an interferometer can always in principle outperform a grating-based spectrometer, the future of soft x-ray spectroscopy lies with high resolution and high throughput Fourier transform interferometry.